Chair of Physics

Master's Thesis

Effects of Partial Oxidation on the Microstructure of Wood Derived Carbons

Hector Herreria Gil

March 2025

MONTANUNIVERSITÄT LEOBEN
www.unileoben.ac.at

AFFIDAVIT

I declare on oath that I wrote this thesis independently, did not use any sources and aids other than those specified, have fully and truthfully reported the use of generative methods and models of artificial intelligence, and did not otherwise use any other unauthorized aids.

I declare that I have read, understood and complied with the "Good Scientific Practice" of the Montanuniversität Leoben.

Furthermore, I declare that the electronic and printed versions of the submitted thesis are identical in form and content.

Date: 0 3 - 0 3 - 2 5

Signature Author Héctor Herrería

Acknowledgments

I would like to express my deepest gratitude to Prof. Oskar Paris, my supervisor, for his invaluable guidance, encouragement, and continuous support throughout this thesis. His insightful advice and scientific expertise have been fundamental in shaping my research. I am deeply appreciative of the time and effort he invested in providing constructive feedback and helping me navigate challenges throughout the course of this work.

A special thanks to Dr. Max Rauscher, my second supervisor, for his unwavering support and expertise in experimental techniques. His patience and willingness to share his knowledge on X-ray scattering and gas sorption instrumentation significantly contributed to the success of this research.

I am also sincerely grateful to all my colleagues and coworkers at the Chair of Physics for creating a collaborative and stimulating research environment. Furthermore, I would like to acknowledge Prof. Christian Mitterer, who was my first supervisor during my Bachelor's Thesis, for introducing me to the world of materials science and for his early mentorship that shaped my academic path. Additionally, I extend my appreciation to Dr. Nikolaos Kostoglou for his support and valuable discussions during my academic journey.

Last but not least, I am profoundly grateful to my family and friends, whose unwavering encouragement and support, despite the distance, have been instrumental in keeping me motivated throughout this endeavor.

Abstract

The transformation of wood into advanced carbon materials relies on the partial preservation of its hierarchical structure after thermal treatments. Unlike isotropic materials, wood exhibits inherent anisotropy due to the alignment of cellulose fibrils along the tree's growth direction within its lignocellulosic matrix. In this study, a pre-oxidation step was introduced before pyrolysis to investigate the effects of structural decomposition at five different temperatures: 250°C, 275°C, 287°C, 300°C and 325°C. These temperatures remain below the threshold for complete cellulose and lignin decomposition, selectively modifying the matrix by targeting hemicellulose, while aiming to preserve the alignment of cellulose fibers through subsequent pyrolysis at 800°C under two different heating rates (7°C/min, 1°C/min) and atmospheres (Nitrogen, Vacuum), and finally activation at 800°C with CO_2, ultimately leading to the formation nanoporous carbons with some anisotropy.

To assess structural modifications, Wide-Angle X-ray Diffraction (WAXD) was used to study the crystallography of cellulose by their intensity curves, focused on the <110>, <$1\bar{1}0$> and <020> planes through all thermal steps. For the pyrolized samples, crystallite sizes from turbostratic nanocarbons arrangement were calculated for the in-plane (La) and out-of-plane (Lc) directions, according to <100> and <002> planes respectively. From the azimuthal intensity distribution of pyrolized samples a parameter η was calculated as a degree of preferred orientation. Beyond WAXD, Small-Angle X-ray Scattering (SAXS) elucidated the density phase contrast difference between cellulose and lignocellulosic matrix for pre-oxidized samples, and details of pore structure for the pyrolized samples. Gas sorption measurements (N_2 at 77k and CO_2 at 273k) were conducted to investigate the specific pore volume (SPV), specific surface area (SSA) and pore size distribution (PSD) of the pyrolized and activated samples.

As a main important outcome, samples that underwent partial oxidation at 287°C showed decomposition of hemicellulose while mostly preserving the crystalline cellulose fiber structure, indicating a controllable method to partially decompose the lignocellulosic matrix. Moreover, 287°C pre-oxidated wood followed by pyrolysis at 800°C with 1°C/min heating rate under vacuum demonstrated enhanced development of pore structure as well as the highest degree of preferred orientation with around 12% of the carbon being preferentially oriented along the tree's growth direction. Final activation at 800°C with CO_2 indicated pore structure development and high material yield for same pre-oxidated temperature at 287°C followed by pyrolysis at 800°C with 1°C/min heating rate. This highlights the potential to preserve anisotropic features to some extent after thermal treatments, suggesting pathways for tailoring wood nanocarbons for advanced functional applications.

Kurzfassung

Die Umwandlung von Holz in fortschrittliche Kohlenstoffmaterialien basiert auf der teilweisen Erhaltung seiner hierarchischen Struktur nach thermischen Behandlungen. Im Gegensatz zu isotropen Materialien weist Holz eine natürliche Anisotropie auf, die auf die Ausrichtung der Zellulosefibrillen entlang der Wachstumsrichtung des Baums innerhalb seiner lignozellulosischen Matrix zurückzuführen ist. In dieser Studie wurde ein Voroxidationsschritt vor der Pyrolyse eingeführt, um die Auswirkungen des strukturellen Abbaus bei fünf verschiedenen Temperaturen zu untersuchen: 250°C, 275°C, 287°C, 300°C und 325°C. Diese Temperaturen liegen unterhalb der Schwelle für die vollständige Zersetzung von Zellulose und Lignin und ermöglichen eine selektive Modifikation der Matrix durch den gezielten Abbau von Hemizellulose. Ziel war es, die Ausrichtung der Zellulosefasern zu bewahren, indem die anschließende Pyrolyse bei 800°C unter zwei verschiedenen Heizraten (7°C/min, 1°C/min) und Atmosphären (Stickstoff, Vakuum) durchgeführt wurde. Abschließend erfolgte eine Aktivierung bei 800°C mit CO_2, wodurch nanoporöse Kohlenstoffe mit gewisser Anisotropie entstanden.

Zur Bewertung der strukturellen Modifikationen wurde Weitwinkel-Röntgenbeugung (WAXD) eingesetzt, um die Kristallstruktur der Zellulose anhand ihrer Intensitätskurven zu untersuchen. Dabei lag der Fokus auf den Ebenen <110>, <1$\bar{1}$0> und <020> über alle thermischen Schritte hinweg. Für die pyrolysierten Proben wurden die Kristallitgrößen von turbostratischen Nanokohlenstoffen für die In-Ebene (L_a) und die Aus-der-Ebene (Lc) gemäß den <100>- bzw. <002>-Ebenen berechnet. Aus der azimutalen Intensitätsverteilung der pyrolysierten Proben wurde ein Parameter η als Maß für die bevorzugte Orientierung ermittelt. Über WAXD hinaus wurde mittels Kleinwinkel-Röntgenstreuung (SAXS) der Dichtephasen-Kontrastunterschied zwischen Zellulose und der lignozellulosischen Matrix für voroxidierte Proben sowie Details der Porenstruktur für die pyrolysierten Proben analysiert. Zusätzlich wurden Gassorptionsmessungen (N_2 bei 77K und CO_2 bei 273K) durchgeführt, um das spezifische Porenvolumen (SPV), die spezifische Oberfläche (SSA) und die Porengrößenverteilung (PSD) der pyrolysierten und aktivierten Proben zu bestimmen.

Ein zentrales Ergebnis der Untersuchung ist, dass Proben, die einer teilweisen Oxidation bei 287°C unterzogen wurden, eine Zersetzung der Hemizellulose aufwiesen, während die kristalline Zellulosefaserstruktur weitgehend erhalten blieb. Dies deutet auf eine kontrollierbare Methode zur teilweisen Zersetzung der lignozellulosischen Matrix hin. Zudem zeigte Holz, das bei 287°C voroxidiert und anschließend bei 800°C mit einer Heizrate von 1°C/min unter Vakuum pyrolysiert wurde, eine verbesserte Entwicklung der Porenstruktur sowie den höchsten Grad an bevorzugter Orientierung, wobei etwa 12% des Kohlenstoffs entlang der Wachstumsrichtung des Baums ausgerichtet blieben. Die abschließende Aktivierung bei 800°C mit CO_2 führte zu einer ausgeprägten Porenstrukturentwicklung und

einer hohen Materialausbeute für dieselbe Voroxidationstemperatur von 287°C, gefolgt von einer Pyrolyse bei 800°C mit einer Heizrate von 1°C/min. Dies unterstreicht das Potenzial, anisotrope Merkmale nach thermischen Behandlungen zumindest teilweise zu bewahren, und weist auf mögliche Wege hin, Holz-Nanokohlenstoffe für fortschrittliche funktionale Anwendungen gezielt zu gestalten.

Index of Abbreviations

APS	Average Pore Size
DFT	Density Functional Theory
ECF's	Elementary Cellulose Fibrils
FWHM	Full Width Half Maximum
IUPAC	International Union of Pure and Applied Chemistry
MFA	Microfibril Angle
PSD	Pore Size Distribution
SPV	Specific Pore Volume
SSA	Specific Surface Area
SAXS	Small-Angle X-ray scattering
WAXD	Wide-Angle X-ray Diffraction

Content

1 Introduction

Biomaterials have become very important during last decades in the field of materials science, serving as source of inspiration as tools for the design of innovative materials and systems from natural structures [1],[2]. There can be found some biological materials with inherent hierarchical structure such like bone [3], showing their self-assembly and evolutionary efficiency, others like wood have been copied through bio-templating methods with silica [4], or ceramics by high precision nanoparticle casting methods [5]. This is because of its inherent hierarchical arrangement of cellulose fibers on the order of 2-4 nm of diameter, oriented along the tree's growth direction within a matrix of lignin and hemicellulose, which makes an ideal option to get textured properties, with the aim to preserve them after carbonization treatments resulting in carbonized wood monoliths [6], in order to achieve advanced applications which are crucial for fast diffusion kinetics or good thermal and electrical conductivity for environmental applications [7]. While it is known that wood cell walls are anisotropic due to the cellulose molecular arrangement [8], it is yet uncertain whether the carbon formed has any preferred crystallite orientation which would contribute to get anisotropy at the sub-cellular level [9]. The mechanical properties of carbonized wood are closely related to the microstructure established during pyrolysis. Studies on carbonized cellulose fibers reveal that the molecular orientation of cellulose governs the structural arrangement of the resultant carbon, influencing the shrinkage, density, and acoustic properties [10]. Axial shrinkage during pyrolysis is minimal, while radial and tangential dimensions decrease significantly, resulting in anisotropic properties, mainly because of cellulose fibrils which dominate the mechanism of dimensional change during carbonization [11].

Carbonization of wood is a general step to get wood-derived carbons where fibers play a big role due to the main aligned constituent within the structure, being possible to achieve fibrous activated carbons [12]. But wood has cellulose fibers embedded within lignin and hemicellulose, which makes more complex the process to achieve open oriented channels inside the structure without removing any of these elements. Therefore, the strategy followed in this study hypothesizes that setting a pre-oxidation step before pyrolysis, which could decompose the elements in between the cellulose fibers while aiming for the orientation preservation of the cellulose fibers, may result in a partially oriented structure. Studies using Thermogravimetric Analysis have elucidated the different temperature decomposition ranges of wood constituents (cellulose, hemicellulose and lignin) [13], from where it is known that hemicellulose decomposes at a range between 220-330°C. Due to their differences in weight loss and activation energy, the possibility to study the range between 250°C and 325°C applying a pre-oxidation step, may affect hemicellulose in a higher extent compared to lignin and cellulose.

Pyrolysis of wood via gasification mechanisms shows the complexity to determine the wood constituent polymers behavior [14], primarily formed by molecular chains of focusing on secondary char formation and volatile composition. There are many studies that concentrate on structural properties of charcoal, as well as hemicellulose studies revealing the behavior by fast pyrolysis treatments [15]. Others which are related to carbon fibers from pure cellulose [16] allow to demonstrate the orientation preservation on cellulose based fibers [17] and others that concentrate on creating nanoporous carbons from lignocellulosics [18]. Nevertheless, wood exhibits complexities to obtain high performance carbon fibers due to the natural cellulose I elementary constituent, but it is possible to study their development of preferred orientation since is not yet fully clear [19]. After pyrolysis, high anisotropy is also a major structural feature common to all cellulose-based fiber carbons, resulting from planar assemblies of graphene sheets oriented more or less parallel to the fiber axis. At the atomic level, graphene sheets with high amount of defects allow to form a turbostratic arrangement, which is strongly distorted in-plane and carbon atom positions can also deviate considerably from the perfect planar structure. Then, fibers are based on the stacking of such imperfect graphene sheets. In contrast to graphite, the high density of in-plane defects and a finite lateral extension of the sheets lead usually to a stacking without any orientational and positional order between the sheets, resulting in the before mentioned turbostratic structure. Two characteristic length scales determine the structure at the nanometer level, both the lateral extension of the sheets L_a and their stacking height L_c are in the range between one and a few tens of nanometers and define a kind of nano crystallites, able to evaluate through X-ray techniques like WAXD [20].

In this study, samples underwent pre-oxidation treatment below 350°C followed by pyrolysis at 800°C, aiming for the orientation preservation of the cellulose-based carbon fibers, therefore getting a full process perspective with activation step in order to evaluate some samples as activated wood-derived carbons. Porosity is the main characteristic of activated carbons, critical for applications in adsorption, catalysis, filtration and energy storage. The activation process introduces nanoscale pores, significantly increasing surface area and adsorption capacity. The common methods for activating previously pyrolyzed samples can be divided into two groups: the chemical and the physical activation or also called thermal activation. On the one hand, chemical variant is mostly based on the reaction with bases such as KOH, introducing an exfoliation effect, leading to a broader distribution of pore sizes [21]. On the other hand, in the physical variant the sample is usually heated under water vapor or

CO_2 atmosphere. Oxygen-containing atmospheres are rarely used because the strongly exothermic reaction burns the carbonated material on the surface. As a result, there is no penetration of the sample and thus no elevation of the surface, but pure mass loss due to the continuous burning of the superficial carbon. The common thermal activation processes are

endothermal reactions [22], which make the reaction rate much easier to control. However, thermal activation with water vapor by no means provides the same results as that with CO_2. The methods differ in their reaction kinetics and thus decisively in their results, in this thesis only CO_2 activation was used, hence the process will be explained in more detail. Activation is stoichiometrically according to the Boudouard equation:

$$C + CO_2 \leftrightarrow 2\,CO$$

This reaction preferably takes place on carbons defects, for example five- or seven-membered, carbon rings. Both in the activation by water vapor and by CO_2 it can form chemisorbed oxides on the surface, which throttle the reaction rate by blocking reactive carbon atoms. Whether the surface complexes are reaction intermediate stages is not yet fully understood [22]. In addition, common reaction equations have only limited validity in the narrow pore spaces in which interactions with the pore surface significantly influence the reaction kinetics.

The importance of cellulose's molecular arrangement is key on structural evolution under controlled thermal conditions. Moreover, the interplay between microfibril orientation and carbon domain alignment reinforces the significance of structural integrity during carbonization. Finally, activation process using CO_2 around 800°C complements the broader discussion on porosity development, analyzing these changes with Gas Sorption analysis. The insight on these studies bridges these detailed processes, providing a holistic framework for optimizing wood-derived carbons in future investigations.

1.1 Wood Structure

Wood is among the most abundant and versatile natural resources on Earth. About more than one third of the world's land surface is covered by forests, becoming one of the most important products. Besides actual issues with deforestation and climate change, wood has always played a role as a natural energy resource, that is why understanding its hierarchical structure is key for the study of main applications.

Wood structure can be described from different scales. In Figure 1a the macroscopic differentiation into multiple parts is shown. Moving from the inside outwards as radial direction, the center is known as the pith of few mm in diameter. It is followed by the core wood, where annual rings are grown every year in two different seasons. Earlywood grows in the spring, characterized by low density and light color, its main task is water transport. In contrast, Latewood grows in the summer, darker color and denser, mainly provides strength. Continuing to the external bark where phloem cells grow, there is a thin layer separating bark from the inside sapwood and core wood where xylem cells are predominant. Core wood is

almost inactive in old trees, having no functionality. The closer to the bark or farther from the pith, the more functionalized and active for the tree the layer is [23]. In Figure 1b microscopic and nanoscopic cell wall structure is shown, which will be in detail explained later, and 1c shows the nanoscopic and atomic structure of cellulose, where molecules are placed in chains within a monoclinic unit cell along the growing tree, parallel to the vertical unit cell axis.

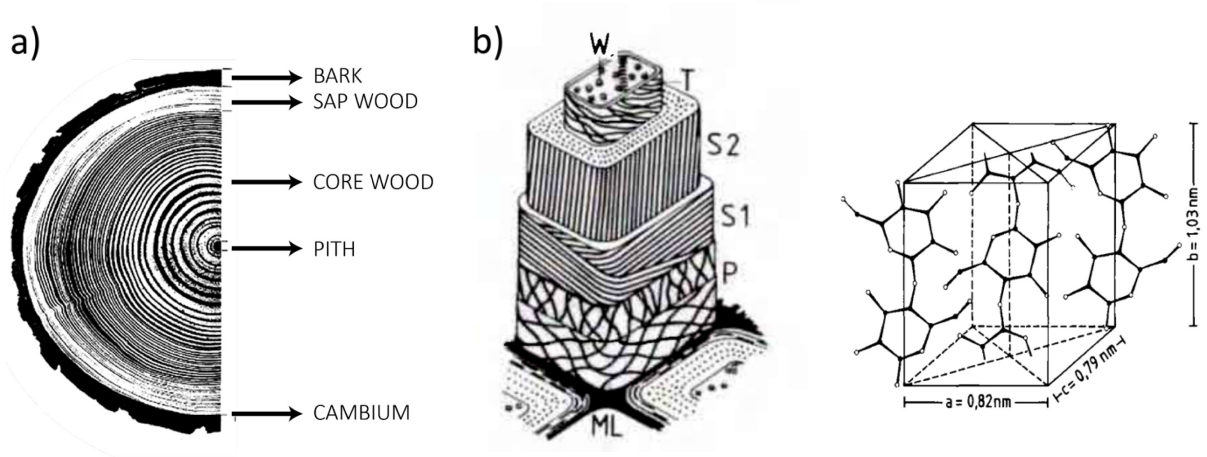

Figure 1: a) macroscopic tree's cross section parts, b) microscopic cell walls arrangement, c) nanoscopic cellulose monoclinic unit cell [24].

When cell wall structure is considered, there exist two main wood categories, only if they experience seasonal changes: Hardwoods and Softwoods. Hardwoods (deciduous trees) have more complex anatomy due to their several cell types, on the other hand, Softwoods (conifers) are older morphologies, and their cell anatomy consists of two types: Parenchyma cells are short with stubby ends, often arranged like bricks, Tracheids (Figures 2-3) are long tube-shaped cells with 20-40 µm in diameter and some mm in length. They transport water and support the mechanical stresses, representing 95 % of the total volume [24]. Main arrangement of Tracheids is divided into earlywood, having thinner and wider lumen, and latewood with thicker walls and smaller lumen, leading to a water and nutrients transport role in earlywood Tracheids, and a mechanical supportive role for the latewood ones. Pits are the small circles located along the Tracheids, are microscopic openings in the cell walls that facilitate the transport of nutrients between cells. In this study, Spruce wood samples are conifers, which contains this type of cell anatomy.

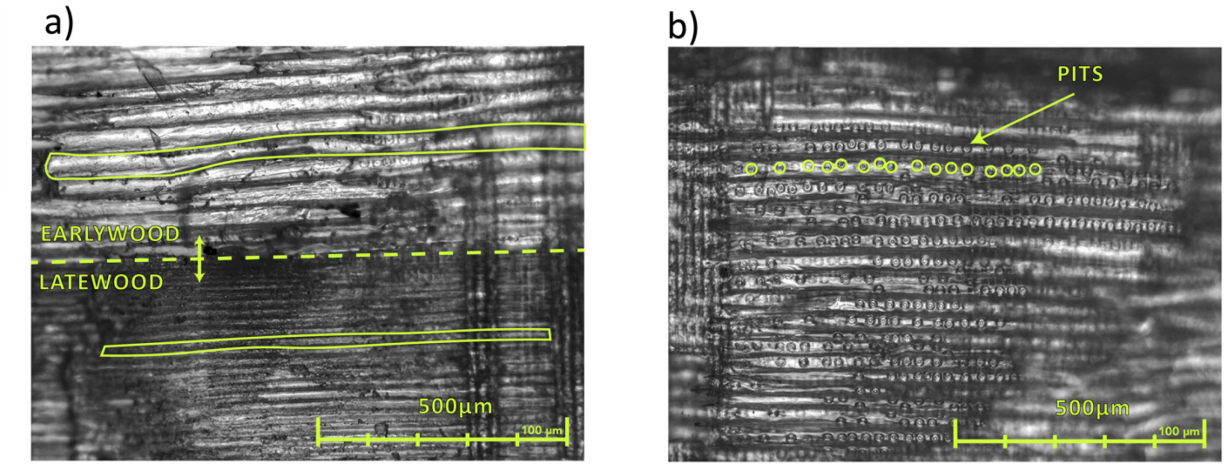

Figure 2: Light Microscope images of Tracheids along the axial direction: a) earlywood (upper bright side) vs latewood (lower dark side) Tracheids, b) Tracheids and pits.

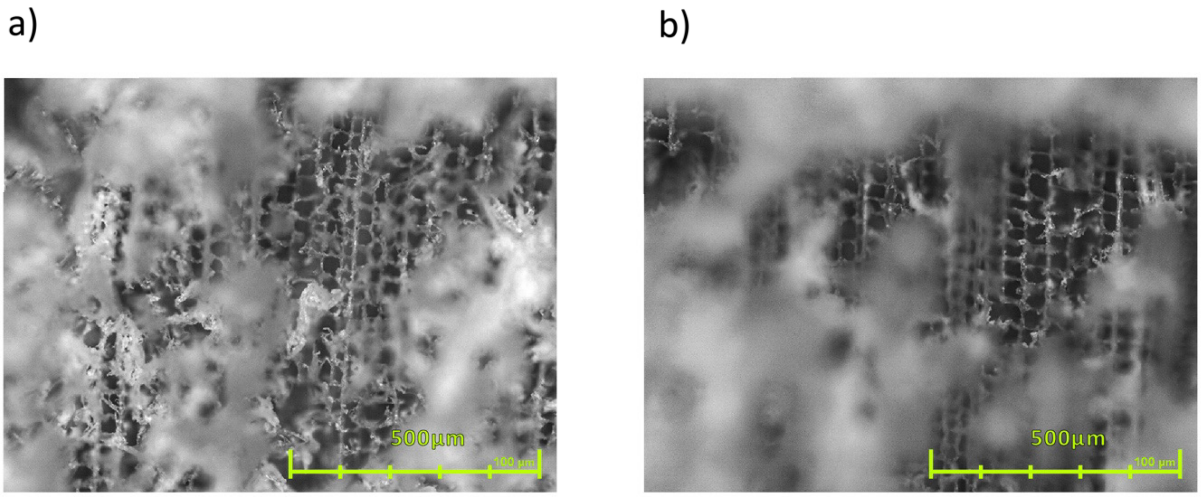

Figure 3: a), b) cross section of Tracheids on earlywood via Light Microscope.

Furthermore, beneath cell wall structure, the nanostructure also referred to as the ultrastructure of the wood cell wall is observed, which consists of organic matter that is highly polymerized. Main macromolecular components are cellulose, hemicellulose and lignin. Cellulose is a high-molecular weight polymer synthesized from exclusively β-D-glucose, considered the most important structural component of plant cell walls where its long chains associate to crystalline fibrils, accomplishing the 40 % relative weight amount of the total cell wall, although it can vary between species. Hemicellulose consists of 31 % of the cell wall, located between elementary cellulose fibrils (ECF's) and lignin. 28 % of the cell wall is occupied by lignin, which provides compressive strength, the rest is given by low-molecular weight substances like alcohols and aromatic compounds [24].

Middle lamella is the first layer to be formed during cell growth, it consists predominantly of lignin, acting as a glue between neighboring cells. Primary wall (P) contains cellulose fibrils kind of randomly connected over the cell wall, then the secondary cell wall is built after cell expansion stops and consists of two or three layers of cellulose fibrils that are close packed and oriented parallel to each other. In the first cellulose layer (S1), fibrils are wound around

the cell in a slow helix while in the second cellulose layer (S2) are wound around the cell in a steep helix. This second layer represents the mayor part of the cell wall with a thickness of approximately 80% of the total in earlywood and 85% in latewood tissue. Furthermore, inside the architecture of S2 layer, particularly the tilt angle of the cellulose fibrils with respect to the longitudinal cell axis, the microfibril angle (MFA) is of great mechanical importance, although it changes between cells of a single tree and between species, therefore mechanical properties mainly rely on this secondary cell wall structure. A complete perspective on the structure scale is shown in Figure 4.

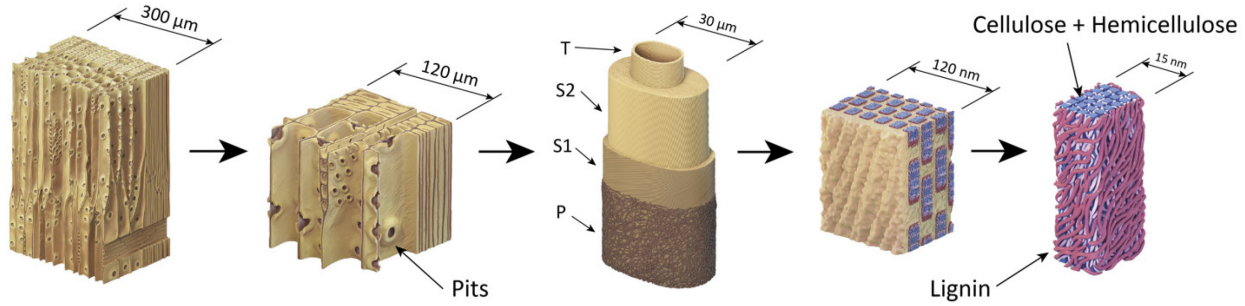

Figure 4: Wood structure from Tracheids in macroscopic scale to nanoscopic arrangement of Cellulose, Hemicellulose and Lignin, with permission from [25].

1.2 X-Ray Scattering on Wood

X-ray scattering is an appropriate tool for the investigation of structures on scales below 100 nm that are no longer accessible by light microscopy. Scattering methods not only allow one to study objects of very small sizes, but they also provide average structural parameters of the irradiated sample volume and therefore, usually yield good statistics in a comparably short time. The main drawback of scattering methods, however, is that one does not get an image in real space but in reciprocal space. One has to rely on models to deduce structural parameters of the sample from its scattering pattern.

In principle, two main different X-ray scattering methods are suitable for the study of wood structure. Wide-Angle X-ray Diffraction (WAXD), which has been successfully and widely used in the past [8], and Small-Angle X-ray Scattering (SAXS) [26]. According to the principle of reciprocity, scattering at wide angles gives information on objects on small length scales and scattering at small angles information on objects that are large compared to the wavelength. Accordingly, WAXD provides information in the range of interatomic distances in crystal lattices, whereas SAXS is appropriate to investigate objects in the nanometer range. Although in this study only WAXD and SAXS were used, Grazing Incident Small-Angle X-ray Scattering (GISAXS) also serves as a versatile tool for characterizing nanoscale density correlations or the

shape of nanoscopic objects at surfaces, buried interfaces or thin films [27]. Further analysis on surface modifications after thermal treatments would be convenient, as well as interfaces between wood and coatings or chemical treatments. GISAXS requires precise sample preparation as smooth thin films or coatings, and since wood samples are naturally complex and hierarchical, their bulk properties are better suited for SAXS and WAXD.

The basic principle is based on the interactions between the incoming X-ray beam and the electron cloud from the sample (Figure 5). The incident beam goes through the sample and exits partly as a scattered beam with different angle (2θ degrees) due to sample interactions. If the scattered beam has changed its energy and therefore the wavelength, the phenomena is called inelastic scattering. Usually, energies around 5-20 KeV are indicated as hard X-rays and lower energies (< 5KeV) as soft X-rays, which have higher probability to be absorbed by the sample. Elastic scattering or Thompson scattering occurs when there is no change in wavelength from the incoming beam, although the relative contribution of elastic and inelastic scattering depends on the wavelength. Also, the transmitted beam is observable, which does not change its direction from incoming beam and is stopped before the detector [28].

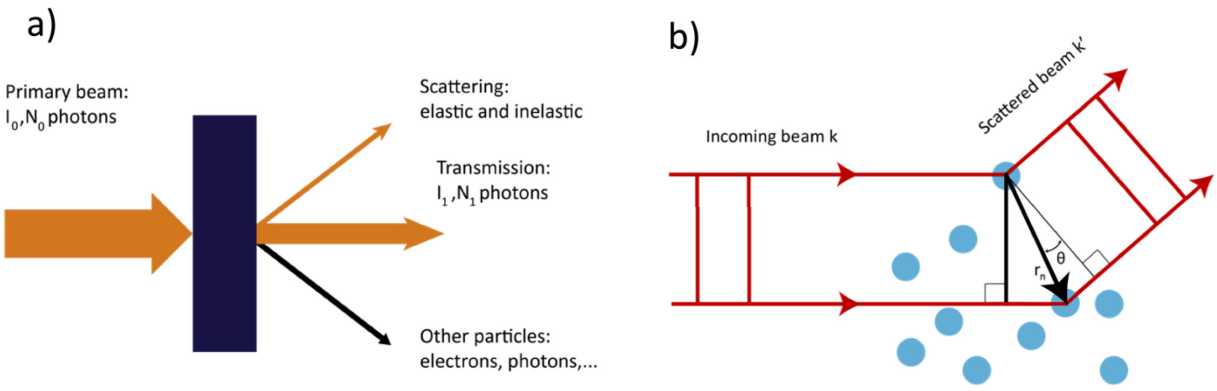

Figure 5: Scattering principle schematically described: a) Incident X-Rays can be scattered, transmitted or generate secondary particles, b) Scattered beam geometry representation.

SMALL-ANGLE X-RAY SCATTERING FROM WOOD

Small-angle X-ray scattering is appropriate for the investigation of nano-sized particles, if there is a sufficient electron density contrast between them and their surroundings. In contrast to X-ray diffraction, both object and surrounding may well be amorphous and therefore SAXS is not restricted to crystals, and it has been applied in different materials for example the study of bones [3]. In the case of a finite volume system, consisting of only two phases with different electron density, the intensity of the radiation scattered at small angles can be written as

$$I(\boldsymbol{q}) = I_0 \, (\rho_A^e - \rho_B^e \,)^2 \left| \int \quad e^{(iqr)} d^3 \, r \right|^2 \qquad (1)$$

Where $\boldsymbol{q}$ is the scattering vector, illustrated in Figure 5b with k' and k as the incoming beam and scattered beam vectors, defined by $\boldsymbol{q} = \kappa' - \kappa$ with $q = |\boldsymbol{q}| = \frac{4\pi}{\lambda} sin\theta$, where λ is the wavelength of the incident beam and 2θ is the scattering angle between the incident and the scattered radiation. I_0 is a constant and depends on experimental parameters. $\rho_A^e - \rho_B^e$ is the electron density contrast difference between phase A and phase B. In the case of wood, phases are cellulose, which is highly crystalline, and hemicellulose with lignin as amorphous matrix. These phases can also be related to pore spaces or voids within the structure which results in higher contrast before thermal treatments. These features are characteristic of each material, depending on weather porosity is enhanced or not when thermal treatments are into consideration. The assumption of only two phases in a biological system is a simplification considering the most prominent phases already mentioned, but they often contain additional phases such as water or air (depending on their hydration state), even partially crystalline regions, which should not be ignored. Nevertheless, the use of multiple phase models is considered when intermediate phases are assumed, or additional features are observable in the scattering data. High resolution data from advanced techniques such as Synchrotron Radiation based anomalous scattering (ASAXS) are suitable for a multiple phases model, where the distinction between more than two phases is possible [28].

The integral in eq. 1 gives information about size, shape and arrangement of the cellulose fibrils. Although their shape in the wood cell wall is not known exactly, a good approximation can be described as long cylinders. Using conventional laboratory X-ray equipment, the diameter of the X-ray beam is usually in order of 1mm. Considering a mean diameter of 40 µm of a typical wood cell and a sample thickness of some hundreds of µm, this makes up hundreds of cells irradiated simultaneously. The irradiation of complete wood cells results in a scattering pattern influenced not only by the orientation of the microfibrils but also by the distribution of cell wall orientations, influenced mainly by S2 and partially by S1 cell wall layers. In Figure 6 is shown the main coordinate system related to the growth axis of the tree and the main orientation of ECF's.

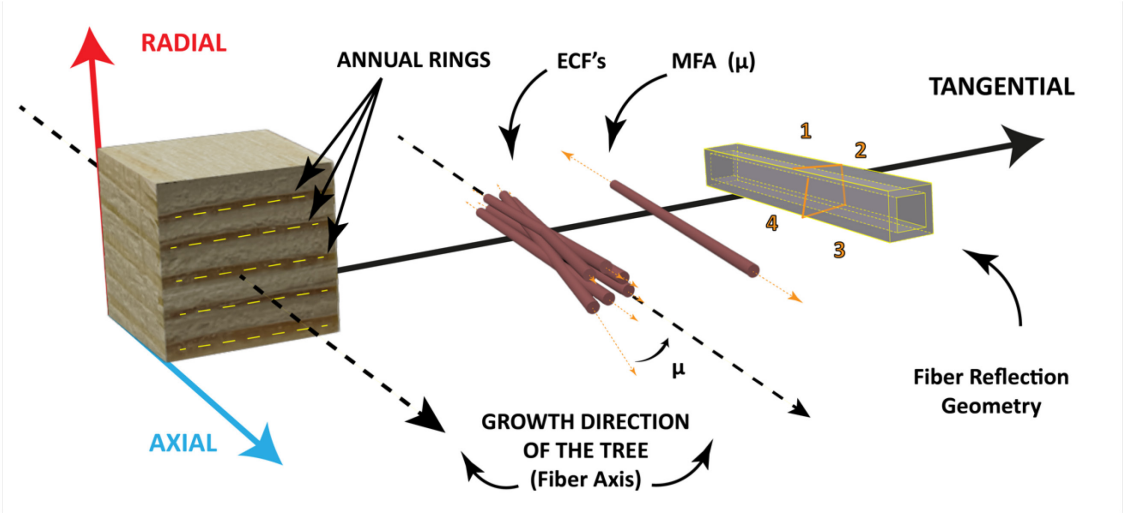

Figure 6: Main orientation of ECF's within wood structure along the axial axis or tree's growth direction.

This distribution is determined by both the shape of the cells and their alignment within the wood tissue, which is critical for SAXS and WAXD measurements, particularly when analyzing equatorial Bragg reflections from cellulose fibers, which refer to the diffraction peaks on the perpendicular direction to the primary structural axis of wood, showing the periodic arrangement of atoms or molecular structures in the plane orthogonal to the main direction. In the case of SAXS, this results in four discs in reciprocal space, each one perpendicular to one of the four fibril orientations. Therefore, from the scattering pattern that is obtained with an area detector, only a two-dimensional section of $I(\boldsymbol{q})$ perpendicular to the incident beam in real space is observed (Figure 7). The coordinates of the scattering vector $\boldsymbol{q}$ and the longitudinal cylinder axis is parallel to the axial direction, getting a disc-like region of high intensity in reciprocal space, that is oriented perpendicular to the fibril axis as the equatorial plane. The SAXS pattern of parallel fibrils corresponds to a section through the disc in the plane perpendicular to the incident beam. This results in a narrow streak perpendicular to the fibril. The streak orientation can be used to determine the fibril orientation with respect to the cell axis. In the special case of the beam being exactly parallel to the longitudinal fibril axis one obtains an isotropic pattern, which is not the exact case due to the natural curvature of wood in the tangential direction. Nevertheless, Ewald sphere effect, which will be further discussed, is more pronounced in WAXD geometry, where higher deviations occur with higher angles.

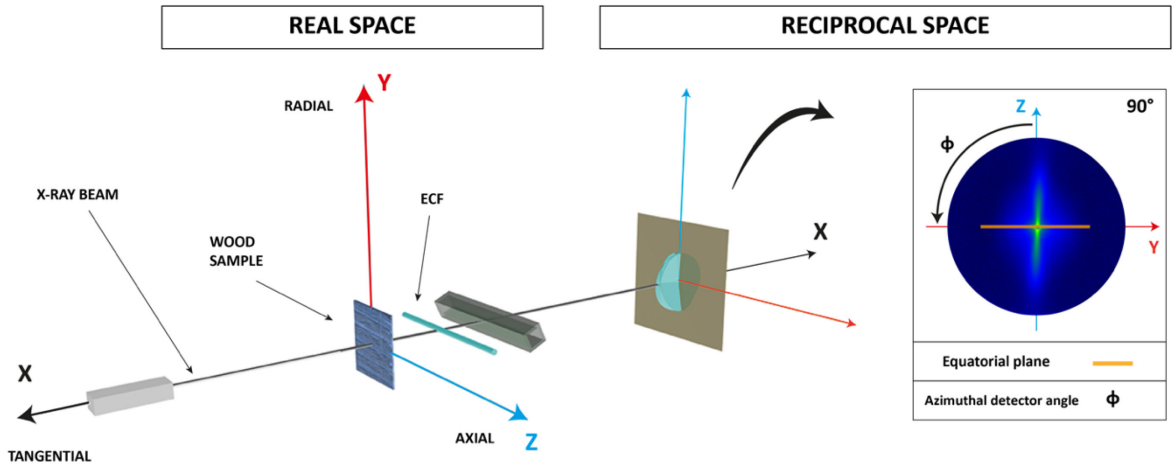

Figure 7: natural wood X-ray scattering set up at 90° with respect to the x-ray beam, scattering pattern of discs like shape in reciprocal space.

WIDE-ANGLE X-RAY DIFFRACTION FROM WOOD

Wide-angle x-ray diffraction is a widely used method for the investigation of atomic structures and orientation of crystals. The method of structure analysis by WAXD uses the fact that the radiation scattered by a crystal lattice appears as Bragg reflections at well-defined values of the scattering vector. The diffraction pattern represents a visual map of the crystal's internal structure, showing how X-rays are scattered by atoms. It is essentially a spatial fingerprint created through a mathematical calculation called Fourier transformation, which converts the real arrangement of atoms in the crystal into a pattern of spots, allowing to reconstruct type and orientation of the real crystal lattice. The Bragg condition for reflection can be written as $\boldsymbol{G} = \boldsymbol{Q}$, where $\boldsymbol{G}$ is a vector of the reciprocal lattice. This formulation of the Bragg condition is equivalent to the Ewald construction where the scattering pattern corresponds to an intersection of a reciprocal lattice point with the Ewald sphere of radius $k_1 = |k| = \frac{2\pi}{\lambda}$. WAXD on a square cell yields a similar situation: instead of the SAXS discs, there are equatorial reflection rings in the same planes. In Figure 8, the 020 reflection rings are sketched. In the center one can see the SAXS signal as smaller discs. Nevertheless, two-dimensional scattering pattern always correspond to the intersection of the Ewald sphere with the object in reciprocal space. In the case of SAXS, the Ewald sphere can be approximated by a plane perpendicular to the incident beam, but at larger scattering angles the curvature of the Ewald sphere leads to an intersection of the object in reciprocal space at points that are not separated by 180°, leading to asymmetric scattering patterns.

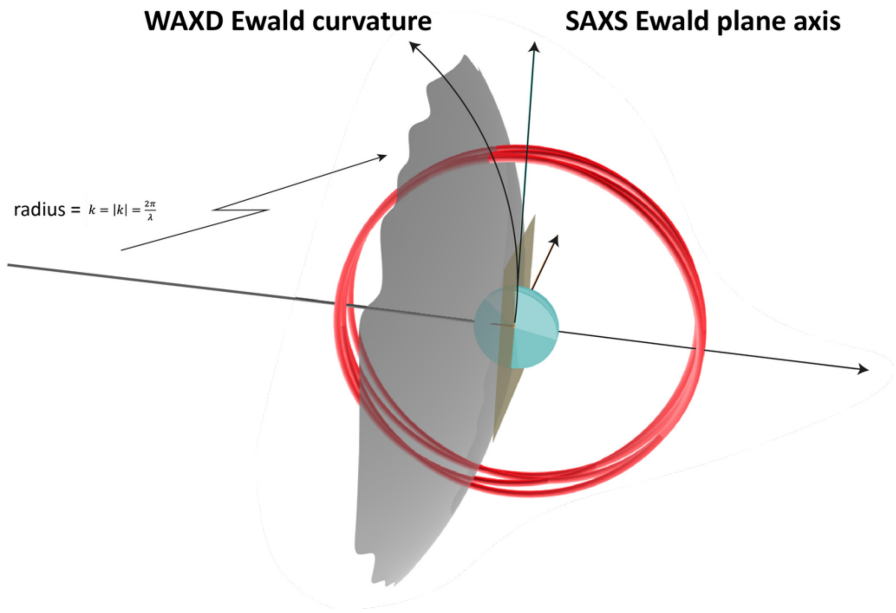

Figure 8: intersection of Ewald sphere with 020 reflection rings in reciprocal space.

WAXD on wood reveals the orientation of cellulose crystallites in the wood cell wall. The c-axis of the monoclinic unit cell has been found to be identical with the longitudinal fibril axis, which is quite fortunate, as it allows to deduce the fibril orientation from the crystalline orientation. The set up for WAXD analysis is shown in Figure 9, where sample is positioned according to fiber geometry, perpendicular respect to the X-ray beam. This geometry is suitable for a SAXS set up as well as for WAXD using the equatorial cellulose reflections for evaluation in the vertical axis. In this case, the only difference in experimental setups between SAXS and WAXD is the range of scattering angles and thus the distance from sample to detector or image plate detector that was used in this case for WAXD. In this work only samples with fiber orientation were studied.

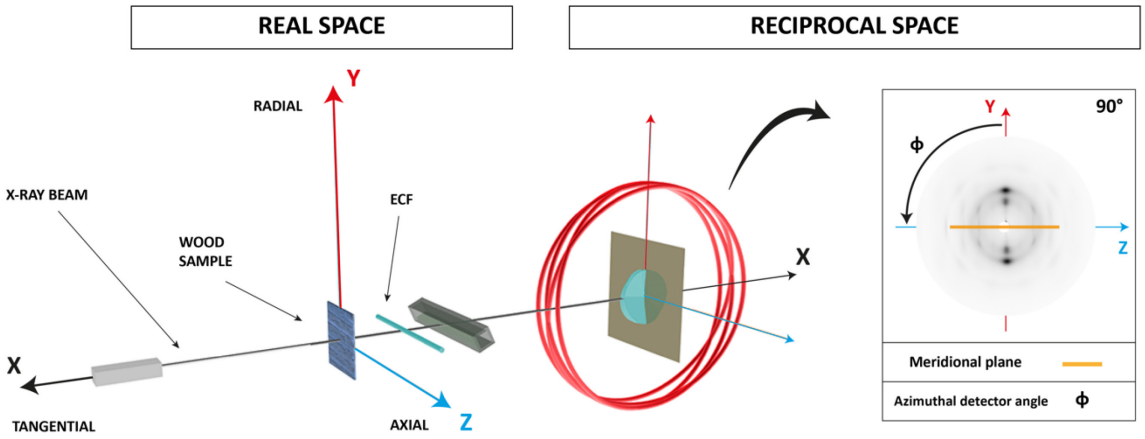

Figure 9: WAXD set up using fiber geometry at 90° with respect to the X-ray beam. Main reflections of cellulose crystallites in elementary cellulose fibrils on the equatorial vertical plane.

In Figure 10, the positions of selected Bragg reflections ($hk0$ and 001) are sketched as they appear in the reciprocal space patterns. The equatorial 020, 110, and $1\bar{1}0$ reflections are perpendicular to the meridional plane, they appear considerably broadened because of the small crystallite size (about 2.5 nm), whereas the 004 reflection is quite sharp due to crystallite size in c-direction of about 11 nm [23]. The same 110, $1\bar{1}0$ and 020 peaks are observed in Figure 11 as concentric circles when spotted the x-ray beam at 0° parallel to axial axis, the broad 110 and $1\bar{1}0$ reflections ($q = 1{,}1$ Å and $q = 1{,}2$ Å, respectively) overlap and are not easily resolved. These two orientations are key to observe the interactions between cellulose fibrils and their reciprocal space in X-rays, but as seen before with the Ewald sphere effect, the intersection with the object in reciprocal space leads to asymmetric scattering patterns, that can be studied with the azimuthal intensity distribution [29].

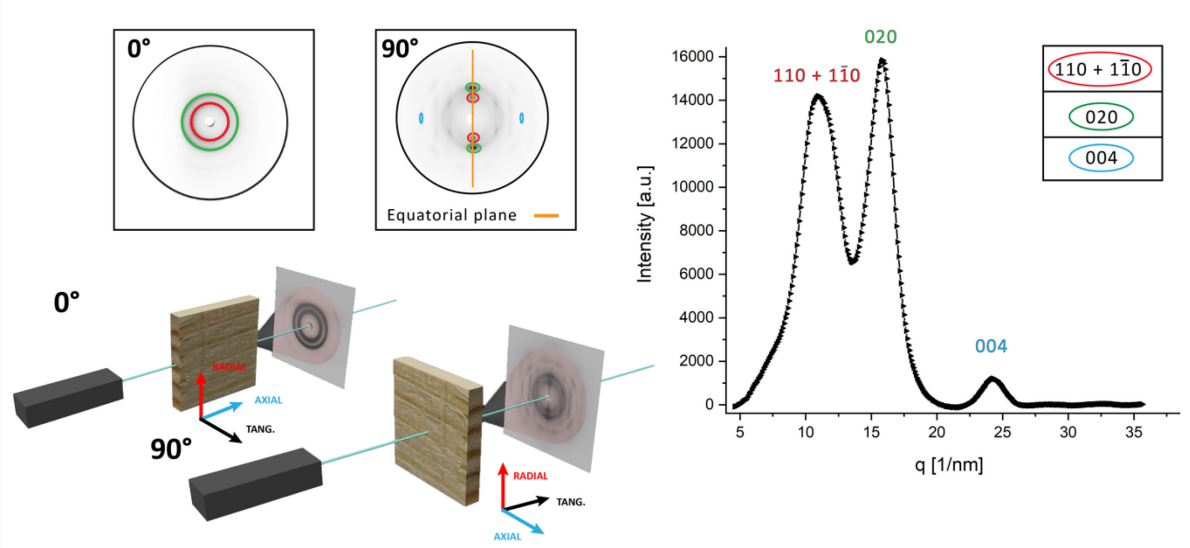

Figure 10: Equatorial Bragg's diffraction patterns plotted (90°) via intensity curves versus position of vector q, at 0°, and 90° (fiber geometry) respectively.

Azimuthal intensity distribution shows the intensity of the area integrated with respect to the angular position, observing the integration for the first peak of non-treated wood in Figure 11. This azimuthal distribution shows the asymmetry due to the Ewald sphere effect, but determination of the center of the beam on the image plate detector may be another feature to relate this shifting position, in which peaks distance in between should be 180 degrees. Nevertheless, azimuthal intensity distribution enables the analysis of each peak individually, calculating the eta η parameter from the integration of the area below the peaks and background, which is the area below the lowest peak intensity value. Definition and calculation of η parameter is shown later in the Experimental chapter of X-ray scattering.

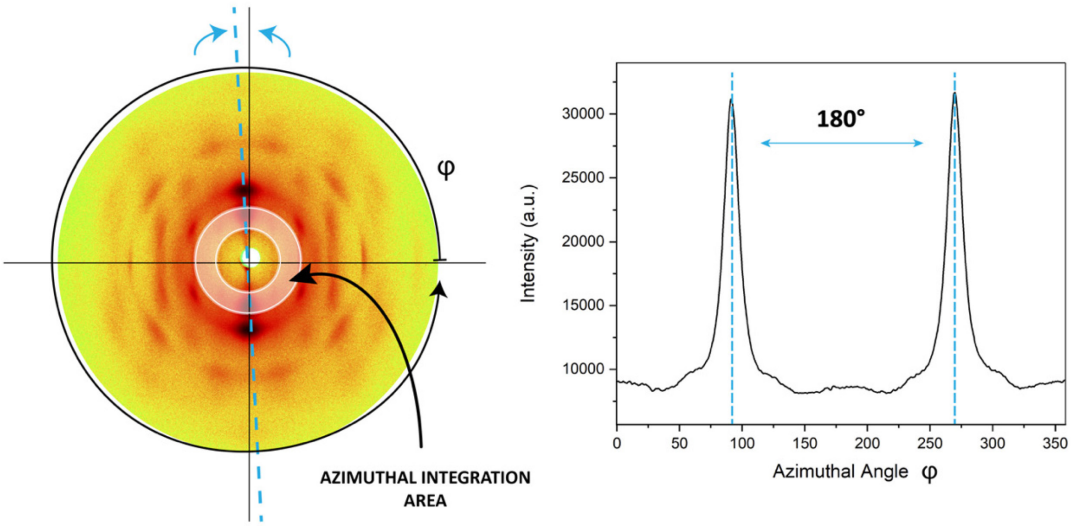

Figure 11: Azimuthal intensity distribution on the first <110> and <1$\bar{1}$0> peaks overlapped, showing the slightly asymmetric distribution.

1.3 Gas Sorption on Wood

Gas sorption analysis is commonly used to characterize nanoporous materials. The pore size range that is studied with this technique is approximately 0.5 - 100 nm in width approximately, including some qualitative analysis on macropore sizes (>50 nm). The other pore size ranges are categorized as mesopores (2-50nm), micropores (<2nm), supermicropores (0.7-2nm) and ultra-micropores (<0.7nm) as it is shown in Figure 12.

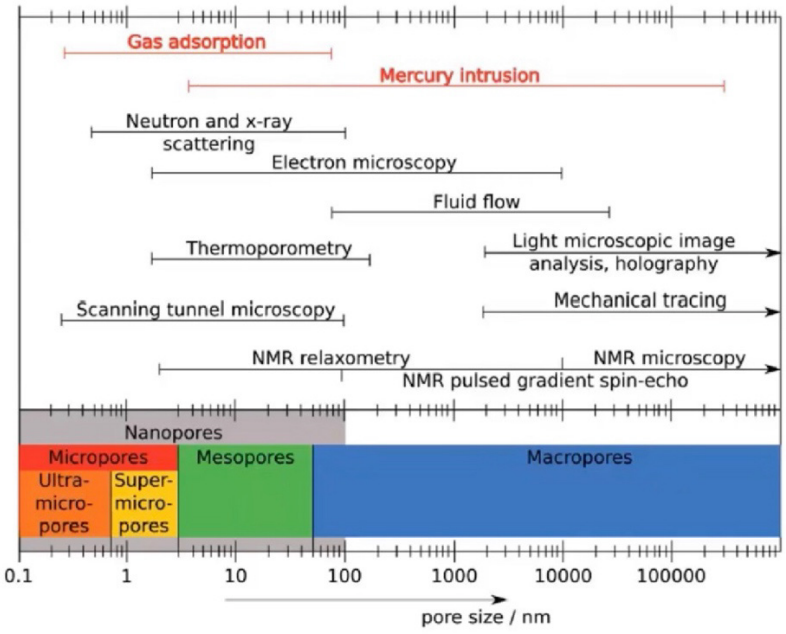

Figure 12: Pore size ranges and characterization techniques [30].

The principle relies on what happens during physisorption phenomena between the material and the gas of choice. Physisorption phenomena is the process by which an accumulation of gas molecules (adsorptive) in a condensed layer (adsorbate) at the surface of a solid (adsorbent) schematically shown in Figure 13. This occurs due to general or specific interactions between gas and solid by Wan der Walls interactions, where the interaction potential has a minimum relatively close to the surface. This leads to accumulation, near the surface, of gas molecules (adsorbate). It has to be differentiated from chemisorption, which is the chemical bonding between molecules, forming at higher enthalpies and as a non-reversible process or at very slow velocity, limited to a monolayer. On the other hand, physisorption involves multilayer formation at very low temperatures, with the analysis focusing on the entire surface rather than specific active sites. The amount of gas that is adsorbed on the surface is a function of strength of interaction between gas, solid, temperature, pressure and concentration. Isotherms are the visual tool to plot the adsorption and desorption behavior of the volume adsorbed versus relative pressure, at a certain temperature generally at a subcritical temperature of the adsorptive. Isotherms are divided in two reversible steps, adsorption and desorption and are classified by their shape, dictated

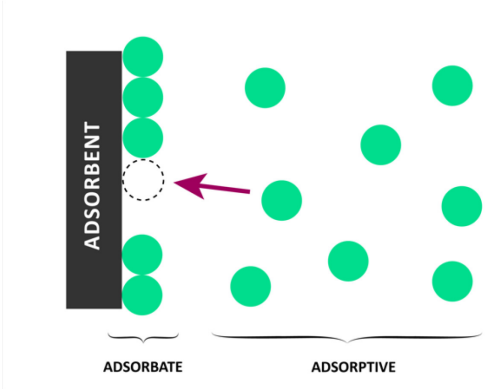

Figure 13: Monolayer formation process.

by the pore size and the surface chemistry of the material, as is described by the International Union of Pure and Applied Chemistry (IUPAC) [31]. Figure 14 shows the isotherm of a mesoporous material, which slightly differs from wood's micropore behavior. The general steps of adsorbate-adsorbent interactions while increasing the pressure on the analysis causes first spontaneous micropore filling (Fig. 14-A) at very low pressures. As the relative pressure increases, monolayer formation (Fig. 14-B) takes place in mesopores, macropores and external surface, followed by multilayer formation (Fig. 14-C) which depends on pore sizes to happen at different relative pressures. Capillary condensation (Fig. 14-D) is the mechanism that takes place at the end of the adsorption branch, where liquid-phase in mesopores below bulk liquid saturation pressure occurs, filling the pores completely. Desorption mechanism starts from this condensation of the gas at high pressures, and it occurs at equilibrium pressure

where the pore liquid starts to evaporate (Fig. 14-E,F), leading to a delayed desorption step as the pressure decreases, called hysteresis loop.

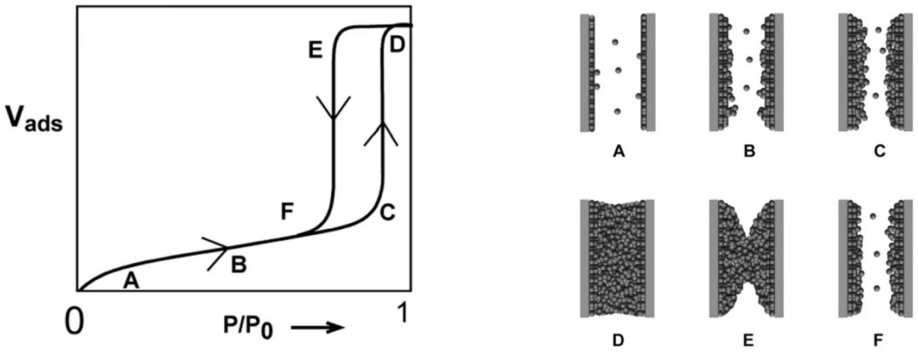

Figure 14: Adsorption and desorption mechanisms process on a Type IV Isotherm by the IUPAC [31].

Each isotherm shape is classified by the IUPAC (Figure 15), depending on the type of pore size distribution the material has and the adsorptive-adsorbent interactions. Type I isotherms are suited for micropores, where the uptake is achieved at the beginning of the curve and then the flat region or "plateau" means no longer adsorption in other pore sizes. Type IV isotherms belong to mesopores materials, where capillary condensation plays an important role showing that characteristic hysteresis loop. Type II is considered for low porous materials or with macropores, where the up taking step is at higher pressure values, even proximate to atmosphere pressures, due to higher pore structure. Type V and III isotherms are suited for weak adsorbent-adsorbate interactions, for example water adsorption within a hydrophobic carbon, finding the adsorption curve at high pressures. Type VI is referred to non-porous materials with a uniform surface where every step in the curve refer to each layer built on the surface. All these isotherms are only valid for the adsorption in subcritical temperature state of adsorptives on rigid solids, if the material to study has some structural changes or flexibility upon adsorption, the specific surface area and pore size characterization is no longer valid. This is why many adsorptives like Nitrogen are used at cryogenic temperature (77K) below their critical point. These types of isotherms serve as a fast way for data interpretation of the measurements.

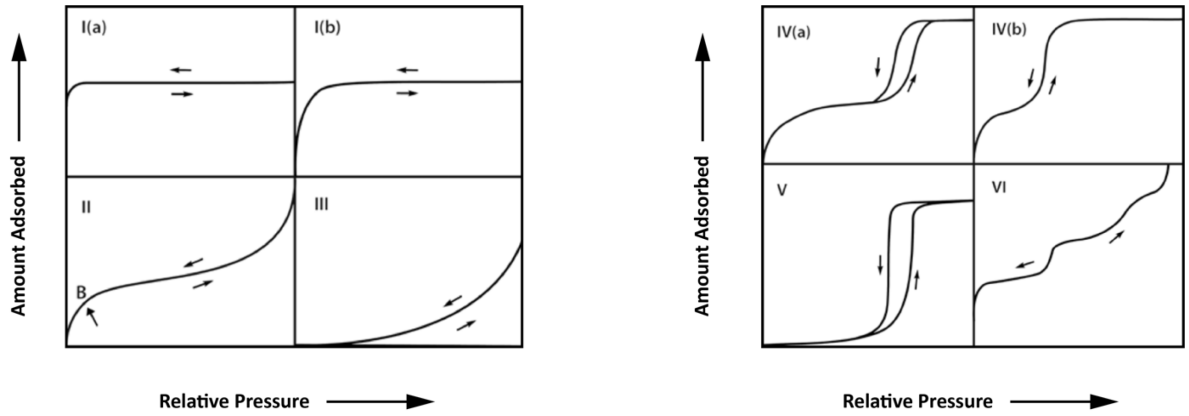

Figure 15: Classification of physisorption isotherms by the IUPAC [31].

On the other hand, isotherms where hysteresis appear, can be further classified depending on the type of hysteresis loop (Figure 16). Hysteresis loop usually appears in the mesopore region, where multilayer formation takes place, and it is distinctive of different types of pore geometries. H1 is related with uniform cylindrical mesopores, where parallel adsorption and desorption branch are achieved. In contrast, H2, H3 and H4 represent ink-bottle type pores, where pore body is only accessible through a narrow neck, showing a characteristic step down in the desorption branch, which is usually steeper than adsorption step, which means that the mechanism of desorption is no longer evaporation from equilibrium but the possibility of two other mechanisms called pore blocking or cavitation. Pore blocking occurs when the neck size is larger than 4nm, these pore bodies can empty until the desorption reaches the pressure where the necks are empty and then the entire system empties. In contrast, cavitation occurs with neck sizes smaller than 4nm, therefore, before even reach the pressure where the neck is empty, reaches the limit where the fluid in the pore body can no longer be a liquid and a spontaneous formation of vapor bubbles inside of the pore which then percolates out takes place. Cavitation is a property of the gas and temperature that is measured, happening at relative pressures between 0.4-0.6 p/po and pore blocking at higher relative pressures than 0.6 p/po. H4 hysteresis are found in micro-mesoporous carbons with a combination of Type I isotherms and a plateau where some hysteresis can take place. H5 are associated with pore structures containing both completely open and partially blocked mesopores. Each type is closely related to particular features of the pore structure and underlying adsorption mechanisms, where desorption branch can be found shifted depending on the mesopore structure and pore blocking effects, cavitation in the other hand, always occurs at the same relative pressures due to thermodynamics.

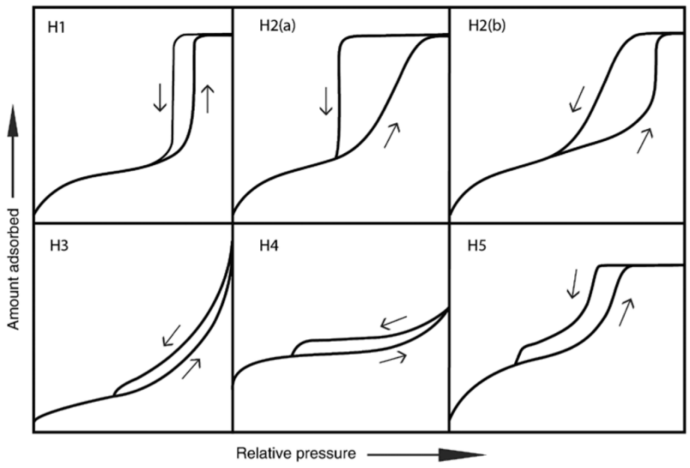

Figure 16: Classification of hysteresis loops by the IUPAC [31].

There exist many different methods to approach the analysis of nanoporous structures such as mercury intrusion or x-ray-based techniques already mentioned, moreover, secondary methods are required to extract surface area or pore volume data, whereas gas sorption is a direct technique that also offers the flexibility to choose between different adsorptive gases. Nitrogen is a traditional adsorptive for surface area and pore size characterization due to its availability and the fact that liquid nitrogen is relatively easy to obtain and there is a well-based understanding on how nitrogen is interacting with materials. However, there are other gases more suitable for the characterization because of the nitrogen quadrupolar nature. Every surface charge or polar nature of the surface can have a significant impact on pore filling pressures and packing of molecules. Carbon materials are non-polar surfaces, and they have no specific interactions with polar nitrogen molecules, therefore is possible to obtain accurate pore size information on carbon materials. Also, it is possible to combine nitrogen with carbon dioxide in order to assess carbon micropores down to 0.3-0.5 nm. For polar surfaces interactions, Argon is the adsorptive of choice, which may also faster, due to its non-polar nature and monoatomic structure compared to Nitrogen.

Analysis in this study are made using Nitrogen (77K) and CO_2 (273K) adsorptives as an ideal combination for the microstructure analysis on wood derived carbons. At elevated temperatures and higher absolute pressures (273K and po=35 Bar), CO_2 can access micropores that are not accessible for N_2 (77K) or Ar (87K) due to its smaller kinetic diameter, therefore it is suited for ultra micropores characterization (<0.7 nm) and a good combination to study the pore size distribution derived from the cumulative pore volume at very small sizes. This information is well interconnected with the surface area, which helps to ensure reliable data within activated and non-activated surfaces. CO_2 measurements are faster, due to higher diffusion rates, this way equilibrium is achieved earlier, which has a big impact on analysis time. CO_2 measurements take around 6 h compared to N_2 of typically between 10-40 hours.

2 Experimental

2.1 Sample Preparation

In the present work all the experimental treatments and processes were carried out at the Chair of Physics at Montanuniversität Leoben. Natural spruce wood samples originally from the surroundings of Leoben were processed in sample sets for each pre-oxidation temperature and an extra non-oxidated natural wood set, following cutting, cleaning, and drying steps. Every sample set is composed by four cubes of 1 cm^3, and every wood sample was cut with a chainsaw from a long stick of a quadratic 1 cm^2 cross section, selected methodically between different sticks with different radial-tangential cross-sectional view. The selected ones show uniform and parallel annual rings as it is shown in Figure 17. To stablish a uniform annual ring distribution similar on each sample is key when thermal treatments and characterization techniques are considered. Hydration state of natural wood is a common property due to the humid environment in an open atmosphere, Therefore, impurities and surface contaminants were removed from every sample set with a mixture of Toluol and Ethanol (2:1 by weight) through 3 different batches in chronological order for two hours at 50°C with a steering magnetic piece, right after, a last batch of only Toluol was set for 12 h with no heat to complete the process (Figure 17a). Afterwards, they all were dried under vacuum at 50°C for 2 h to eliminate any hydration state in the bulk of the sample. Nevertheless, natural deviations need to be considered for shrinkage and x-rays measurements due to the curvature in tangential direction of the tree. Besides those features, x-rays sample preparation required another cut with the fiber geometry before mentioned, on the axial-radial plane (Figure 17b). This cut was made with a blade, trying to not infer critical mechanical loadings or stresses which may affect the results afterwards.

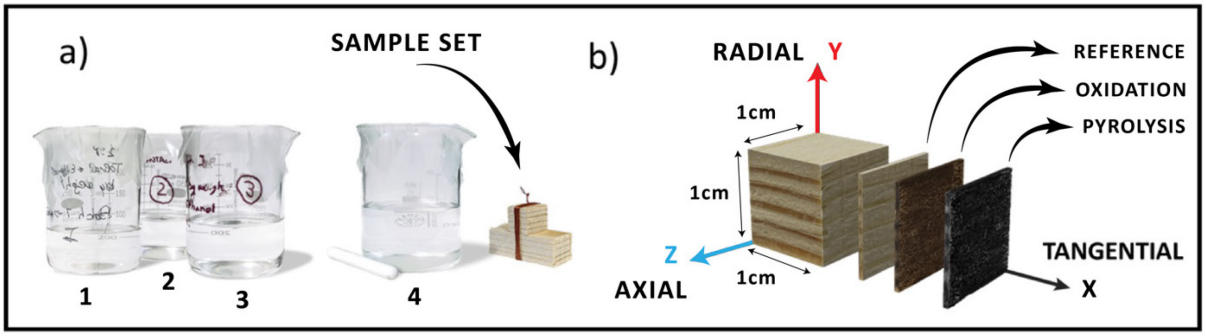

Figure 17: a) batches in chronological order of use. Each sample set consists of 3 cm stick of 1 cm^2 cross section and one single cube that were cut into four cubes, b) cutting orientation of wood cubes and sample preparation cuts for x-ray measurements.

Thermal treatments were proceeded in chronological order: pre-oxidation, pyrolysis and activation. Samples are labeled by the pre-oxidation treatment temperature first, followed by pyrolysis temperature, heating rate and atmosphere, followed in the case of activated samples of the activation temperature and atmosphere. Samples used for each treatment are shown in Table 1 as a design of experiment, where different temperatures from pre-oxidation step are the main indicator (250°C, 275°C, 287°C, 300°C and 325°C). A reference (i.e., non-pre-oxidated) sample was used named as REF to compare the influence of partial oxidation and pyrolysis conditions, which are divided into three treatments indicated by the atmosphere, heating rate and temperature parameters, named as Pyro 1, Pyro 2 and Pyro 3, respectively. For activation, samples were selected from pyrolyzed samples between two pyrolysis conditions: Pyro 1 and Pyro 3. Due to the furnace limitation capacity and to get an overview on how activation could modify different sets of temperatures, 275 and 287 from Pyro 3 under vacuum and 300 and REF from Pyro 1 were chosen. Matrix of samples is not completed due to the decisions during experiments and which samples to treat mainly due to furnace capacity.

	250°C	275°C	287°C	300°C	325°C	REF
Pre-Oxidation 1h	X	X	X	X	X	
Pyrolysis 1 - 7°C/min NITROGEN 1h 800°C		X		X	X	X
Pyrolysis 2 - 1°C/min NITROGEN 1h 800°C	X	X	X	X	X	
Pyrolysis 3 - 1°C/min VACUUM 1h 800°C	X	X	X			X
Activation - CO_2 1h 800°C		X	X	X		X

Table 1. Design of Experiment table. Colors are followed for all diagrams in the results chapter.

2.2 Thermal Treatments

Five different heat treatments took place using a cylindrical tube furnace (Carbolite Gero), which was controlled manually by the program settings. The main set-up consists of the furnace with the ceramic tube, the gas handling system, valve of exit gases and to close the cylindrical tube, and two gas mass flow controllers were used, operated externally with the software Bürkert Communicator. Figure 18 shows the furnace set up in the laboratory.

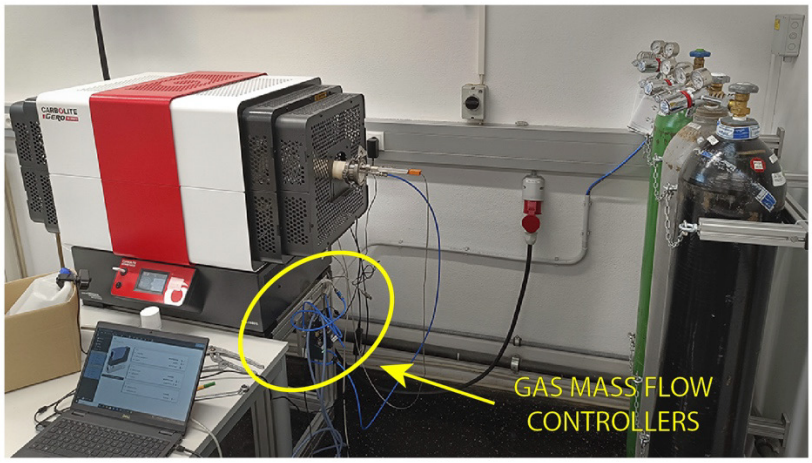

Figure 18: Heat treatment set up by the gases on the right part of the image, connected to the gas mass inputs on the left with blue wires.

The samples were prepared in a ceramic sample holder suited for cylindrical furnaces with space for only four cubes of samples, as shown in Figure 19. The alignment of the samples with the gas mass flow inside the chamber was parallel to the axial direction Z, since this might allow a better gas transport process through the tracheids.

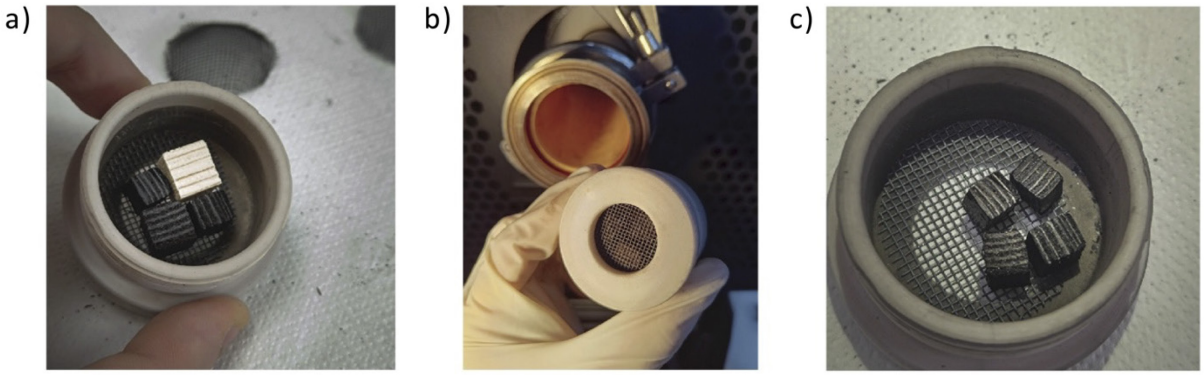

Figure 19: Set of four samples prepared for furnace treatment: a) pre-pyrolyzed and native samples, b) introduction of the sample set into the cylindrical furnace with axial axis oriented parallel to the gas flow inside the tube, c) post-pyrolyzed samples.

Before and after every thermal treatment, samples were weighted, and their three main dimensions (axial, radial and tangential) were measured with a vernier caliper, to get mass loss and shrinkage data. Only activated samples were no longer able to measure their lengths, due to strong deviation of the samples from cubic shape after material characterization extraction of the samples, as shown in Figure 20.

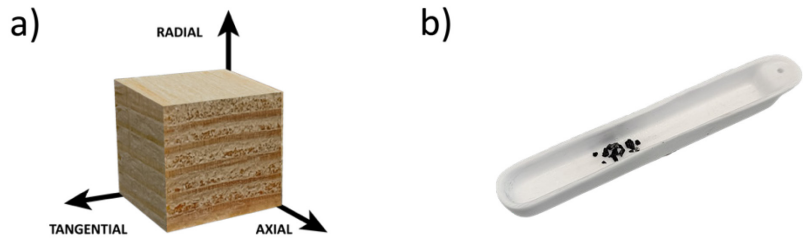

Figure 20: a) Lengths orientations measured on every sample, b) Activation sample preparation.

Parameters for every thermal step are further explained individually in detail. Although in every treatment the temperature ranges are discussed, there exists a deviation on the temperature with the settings. The temperature sensor controller has the function to not overshoot the desired temperature, therefore furnace settings were designed with an extra time of 5 min to get closer to it. This results in a temperature offset for every treatment which is in order of 3°C cooler than the set value. The furnace diagram for oxidation is the one that has these features, pyrolysis and activation diagrams don't need this extra time due to the flow during heating. First diagram to explain is oxidation process, which can be divided into four sub-areas divided by dots line (Figure 21). The first area was used for heating with the heating rate of 2°C/min. This was followed by the inserted additional holding time of 5 min. The third sub-area is the partial oxidation-relevant holding time, which is reflected in the naming of the samples. Finally, a cooling down to room temperature. During sub-areas I, II and IV, the furnace was set with a flow rate of 500 ml/min N_2. In the natural furnace cooling, N_2 flow was continued for two hours to prevent adsorption of humidity and other impurities, then until reaching a safe temperature range, the flow was stopped and the vent valve of the furnace was closed. As a result, the sample was still in the N_2 atmosphere for the remaining cooling. At the beginning of the partial oxidation step, the sub-area III, the gas could be converted from only N_2 (at a flow rate of 450 ml/min) to a mixture of O_2 (2%) and N_2 (98%) (at 50 ml/min flow rate). The cooling procedure took place at the end of sub-area 3, where again a flow rate of 500 ml/min of only N_2 was set to maintain the total flowing rate.

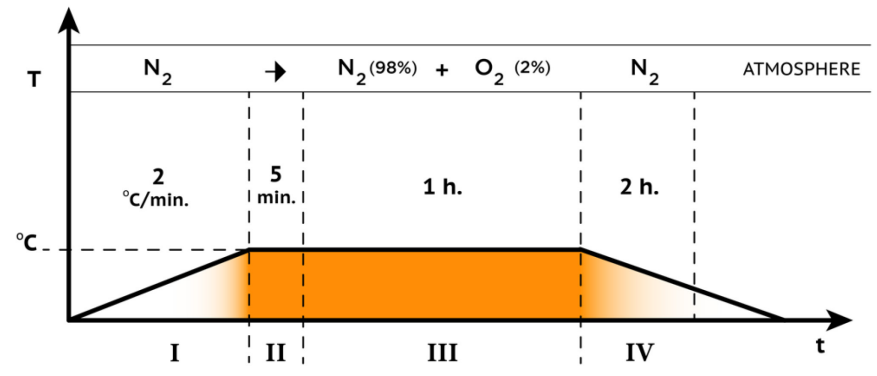

Figure 21: pre-oxidation time-temperature diagram.

The furnace diagrams of pyrolysis treatments can be described by the same three sub-areas I-II-III observed in Figure 22, in these diagrams no extra holding time was used. First difference between Pyro 1-2 and Pyro 3 is the atmosphere under Nitrogen and under vacuum respectively. Furthermore, different heating rates were set on each: Pyro 1: 7°C/min until 800°C (Figure 22-a), Pyro 2: 7°C/min until a temperature of 250°C (which is the first oxidation temperature), followed by a second heating rate of 1°C/min until 800°C (figure 22-b), and Pyro 3: 7,5°C/min until 250°C, followed by a heating rate of 0,2°C/min until 400°C and 1°C/min until 800°C (Figure 22-c). The third sub-area is the relevant holding time for 1 h. Finally, a cooling down step until reach room temperature. For Pyro 1-2 the furnace was set with a flow rate of 500 ml/min N_2. In the cooling stage, N_2 flow was dispensed until cross a safe range temperature of 250°C to prevent adsorption of humidity and other impurities, after this, the flow was stopped and the vent valve of the furnace was closed. As a result, the sample was still in the N_2 atmosphere for the remaining cooling time.

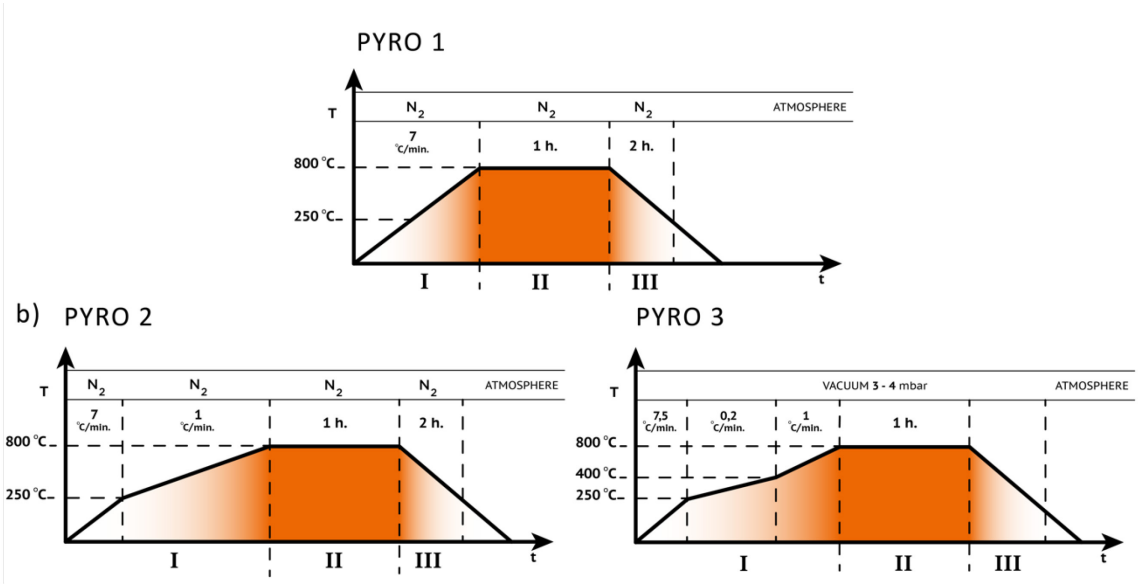

Figure 22: Pyrolysis diagrams.

The activation treatment diagram can be divided into four sub-areas (Figure 23). The first area was used for heating with a heating rate of 7,5°C/min until 800°C. This was followed by the inserted additional holding time of 5 min. The third sub-area is the activation-relevant holding time, which was for 1 hour. Finally, a cooling down to room temperature. During sub-areas I, II, and IV, the furnace was set with a flow rate of 500 ml/min N_2. In the natural furnace cooling, N_2 flow was continued for two hours to prevent adsorption of humidity and other impurities as well as the mixture with air and possible decomposition of the structure at still high temperatures, this is why it was maintained until lower a safe temperature range of less than 100°C. After reaching that temperature, flow was paused, and the vent valve of the furnace was closed. As a result, the sample was still in the N_2 atmosphere for the remaining cooling. At the beginning of the activation step, the sub-area III, the gas flow was changed from N_2 to

CO_2 with a flow rate of 177 ml/min. The cooling procedure took place at the end of sub-area III, where again a flow rate of 500 ml/min of N_2 was set.

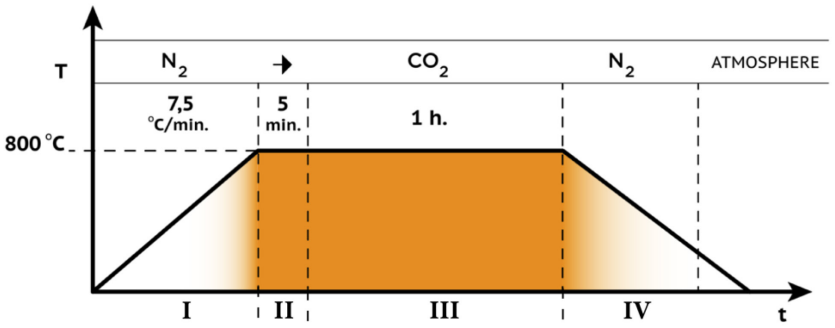

Figure 23: Activation treatment process time-temperature diagram.

2.3 X-Ray Scattering

2D-SAXS patterns were integrated by sectors, main information on the streak from the pattern was integrated as a whole cake, but also two more sectors were integrated with an amplitude of 45°, as it is shown in figure 24, which makes possible to indicate other possible pore orientations in the structure. Nevertheless, due to the influence of cracks in wood, only at high q values this influence should be small enough to make realistic judgements.

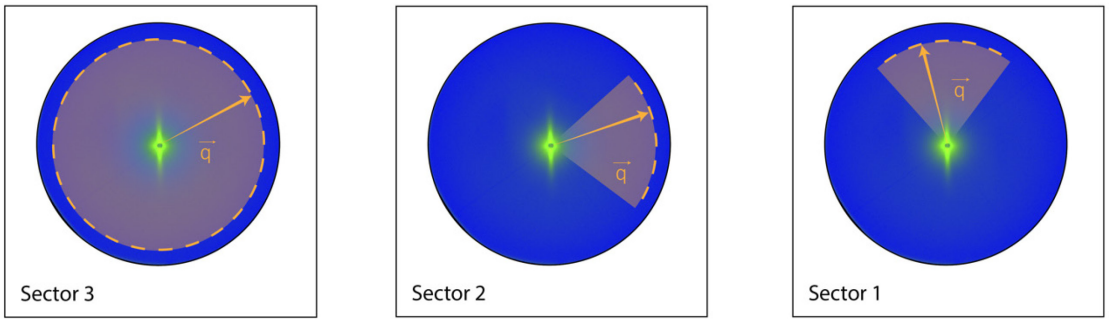

Figure 24: SAXS patterns analysis by sectors on pre-oxidated wood at 300. Amplitude angle of Sector 1 and 2 is 45°

The X-Ray measurements were performed in two different instruments. The samples were positioned in the same position, fiber geometry oriented 90° with respect to the x-ray beam (Figure 10). The scattering patterns show the reciprocal space of fibrils. When oriented horizontally, patterns showed vertical discs for SAXS and the points or ellipses that are surrounding those discs in the case of WAXD. The main difference between WAXD and SAXS

analysis is the distance between sample and detector, resulting in a bigger scattering angle for WAXD, as it is shown in Figure 25.

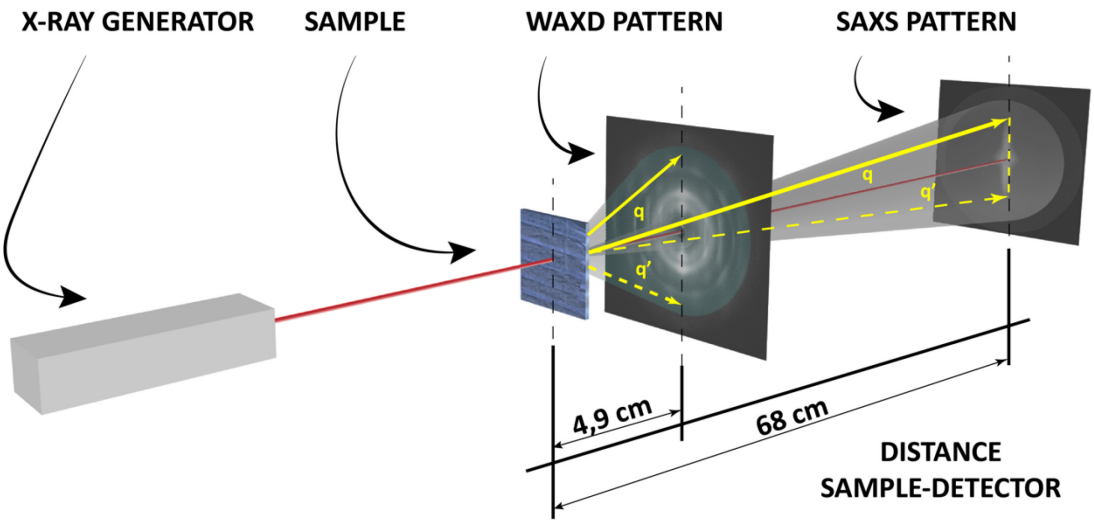

Figure 25: Set up for WAXD and SAXS.

The SAXS analyses were performed with N8-Horizon laboratory instrument using a microsource X-ray generator (N8, Bruker AXS). The X-ray source operated at 45 kV and 650 μA, using a beam with a wavelength of 1,54 Å, and the 2D patterns were collected under vacuum conditions. The distance from the sample to the detector is 68 cm. Every measurement has a measurement time of 30 minutes, which was set as minimum time to get good resolution patterns. The collection of scattering patterns was externally controlled by computer. The software package SAXS (Brucker AXS) was used for data collection and MULIP SAXS-2D, created by Dr. Gerhard Popovski, for data evaluation. Samples were placed on the sample holder with scotch tape with the fiber geometry orientation, using the same sample holder as in WAXD device.

The WAXD analyses were performed with a Nanostar laboratory X-ray instrument using a microsource generator (Bruker AXS). The X-ray source operated at 45 kV and 650 μA. The beam wavelength is 1,54 Å, and the 2D patterns were collected under vacuum by using an image plate of 50 μm pixel size with a hole in the center, to let pass the x-ray beam. The distance from the sample to the detector is 4,7 cm. Measurement time of 30 min was used too. Scanned imaged plate for every sample output is a TIFF file which had to be analyzed with the same software MULIP SAXS-2D program. The sample holder used for both SAXS and WAXD is shown in Figure 26-a, and Figure 26-b shows the position of the sample holder inside the chamber and image plate position, using afterwards the scanner to take the images from the image plate first.

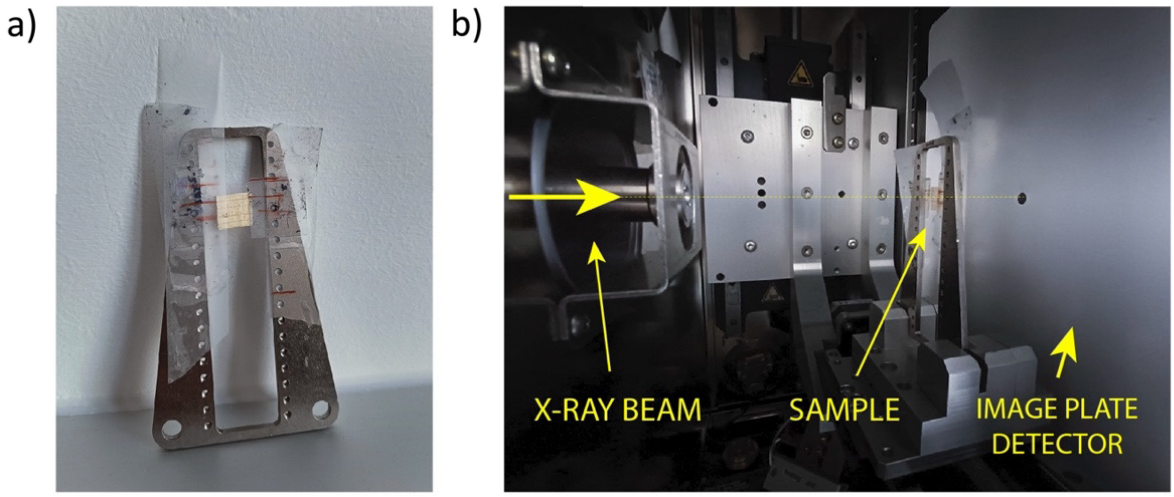

Figure 26: a) sample holder used in SAXS and WAXD, b) WAXD set up inside the chamber.

Every measurement needed to be prepared previous erasing of the image plate for every analysis, using the scanner Fujifilm, FLA-8000 and image plate and Fujifilm Eraser 3 shown in Figure 27. Erasing time for about 3 minutes for every sample.

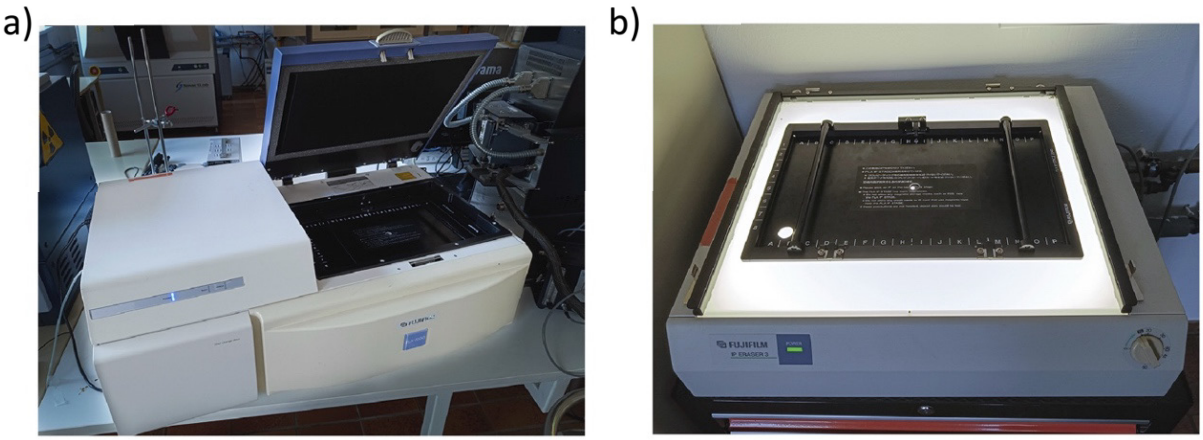

Figure 27: a) Fujifilm Scanner and b) Fujifilm Eplaser3, used for screening the image plate before and after every measurement.

Azimuthal intensity distribution was evaluated in sector for the pyrolyzed samples, observing the two peak areas according to 002 plane and 100 reflections from turbostratic carbon, as seen in Figure 28, with the respective azimuthal intensity distribution diagram. Peaks on the 100 are expected to appear around 0° and 180° respectively, while 002 shows at 90° and 270° as it is observed in the image, nevertheless, Ewald sphere effect and other features like sample position, beam center adjustment, several irregularities on the samples, and possibility of tilted samples and image plate detector made difficult to analyze in a perfect way the x-ray 2D patterns, where here is observed the non-exactly position of the peaks where they should

be. All the WAXD azimuthal diagrams can be seen in the Appendix compared each sample with 002 and 100 positions. Here is shown Pyro 2 for 287°C.

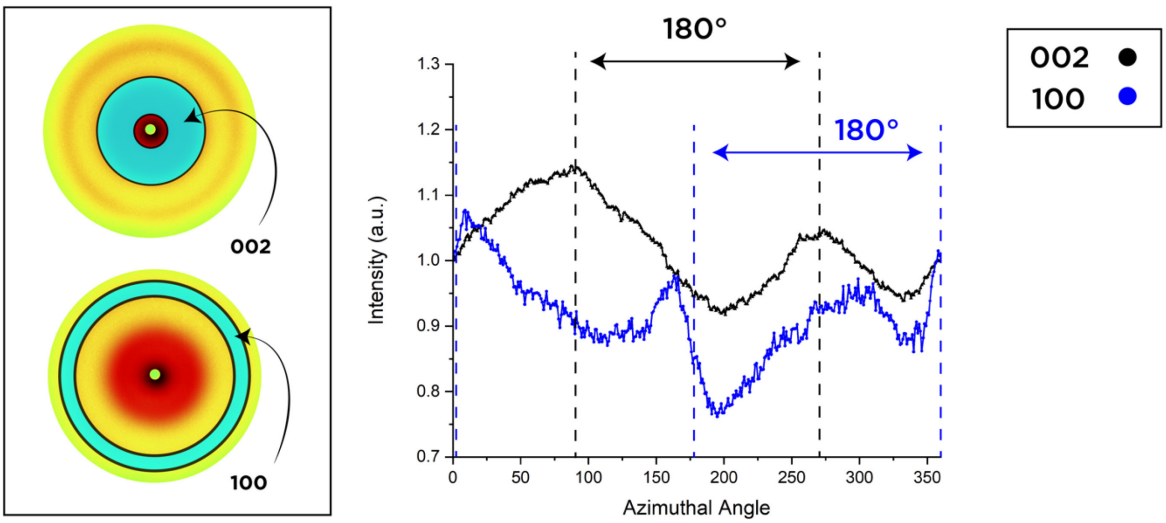

Figure 28: Azimuthal integration sectors at q: 8-20 nm^{-1} for 002, and q: 30-35 nm^{-1} for 100.

Peak Analysis

In order to evaluate the half-value widths of the Bragg peaks from WAXD, main 002 and 100 peaks from pyrolyzed samples were analyzed to determine the crystallite sizes of turbostratic carbon in two different directions, suitable fit functions had to be selected and used on the WAXD peaks by using OriginLab Pro 2023b for evaluation. First background was removed by baseline fitting with a spline mode, adjusting the points manually. Then, a new curve without background is analysed with peaks fitting function. The fit used is Pseudo-Voigt for the <002> and <100> peak. Both peaks fit in all the samples, where an r^2 of 0.99 is reached in all of them. Figure 29 shows the steps removing background and fitting the peaks, while the rest of the peaks fitting curves and baseline analysis can be found in the Appendix. The full-width-half-maximum (FWHM) and the peak position, i.e. the abscise value of the maximum of the fit, could be obtained from the peak fits. Using the formula

$$L = \frac{k * 2 * \pi}{FWHM} \qquad (2)$$

FWHM was collected from the FWHM values Lc and La. Where k is a constant, L is the crystallite size and FWHM is the full width half maximum of the corresponding peak. For Lc and La, the constant k was used as 0.9 and 1.84 respectively [32].In this case, Lc is to be interpreted as the average extension of the coherently spreading areas in the [002] direction,

which result from the parallel stacking of the graphene layers. La corresponds to the average extent of the ordered areas along the [100] direction, i.e. in the in-plane direction.

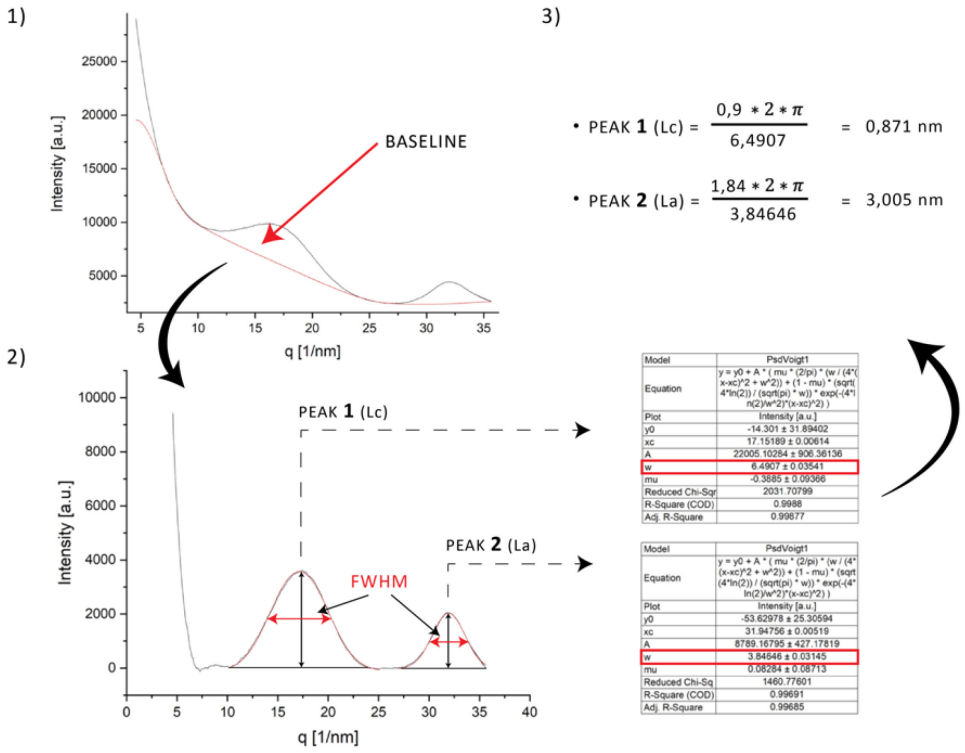

Figure 29: 1) spline-baseline manually points adjusted for background removal, 2) PsDVoigt1 Fit method used for the FWHM analysis, 3) Lc, Lc calculations for the peak fit.

Furthermore, azimuthal intensity distribution was also analysed by a model using the following equation to fit the peaks from original cellulose 110, $1\bar{1}0$ and 020:

$$f(\alpha) = B + A\,sin^2\alpha \qquad (3)$$

where the area below the peaks as background and the area below the peaks is fitted resulting in equal amplitude peaks as seen in Figure 30 from Pyro 1 example, the rest of the fitting curves can be found in the Appendix divided by each thermal treatment. After fitting the curves, parameter η of preferred orientation was extracted in comparison with temperature treatment.

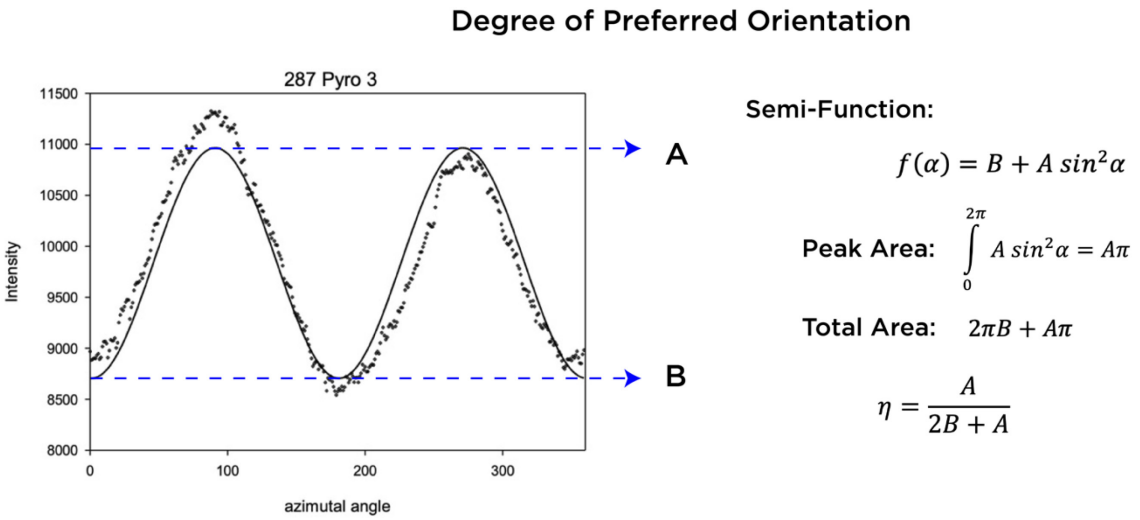

Figure 30: Fitting curve from azimuthal intensity distribution, where original data is presented as dashed line and fitting curve in continuous black line using eq. 3.

2.4 Gas Sorption Analysis

The gas sorption measurements took place at the gas sorption laboratory, using the Quantachrome Autosorb iQ from Anton Paar company in Graz, Austria, as well as their software Quantachrome ASiQwin for data analysis. Sample cells used were 9 mm tubular and 6 mm spherical cells (Figure 31). Steps to conduct the analysis were carried out after heat treatments, therefore every sample was first degassed under vacuum to eliminate any moisture or contamination on the material surface. Partial oxidation samples were degassed for 24 h at 120°C to and pyrolyzed and activated ones for 24 h at 250°C. This is simply because partial oxidation temperatures range is set between 250°C and 325°C, therefore degassing step was set clearly below 250°C for partial oxidation to avoid any microstructural changes. Nitrogen at boiling point temperature of 77K and Carbon dioxide at 273K were used as adsorptives. The set up for each of those relies on a cooling bath at 0°C for CO_2 and a nitrogen bath at -196°C for the N_2.

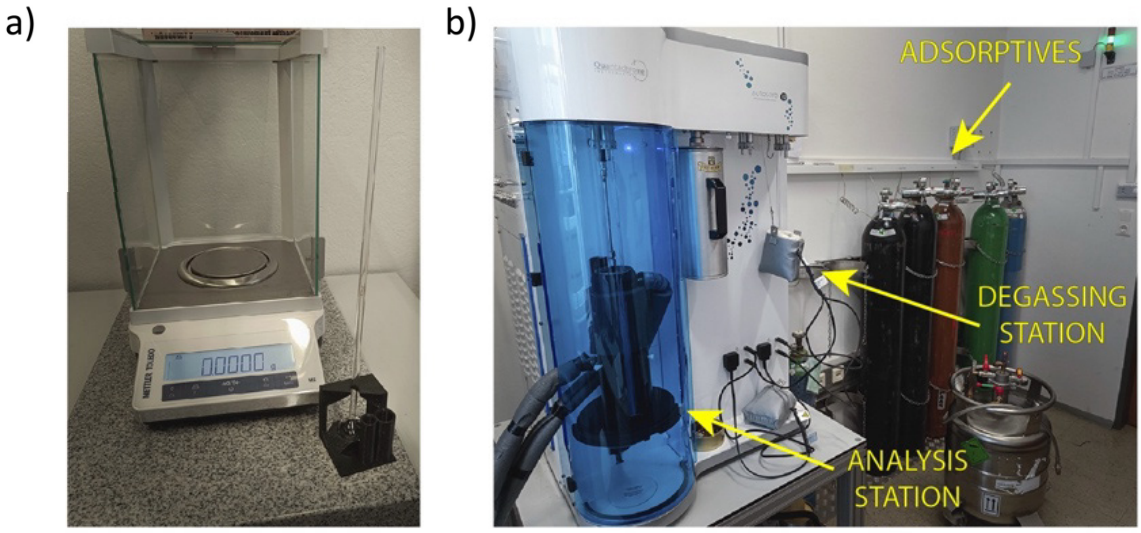

Figure 31: Gas sorption analysis station: a) 6mm spherical cell, b) Quantachrome Autosorb set up analysis for CO_2 measurement.

Data point from N_2 analysis were set at low relative pressures of 10^{-5} mbar in order to achieve the BET plot. This was the main issue that was found when testing partial oxidation samples and some pyrolyzed too, where N_2 took very long time to analyze and even for many samples relative pressure was set down to 10^{-2} mbar to at least achieve the main beahaviour on the isotherms. To obtain the isotherms from the data, modern methods based on statistical mechanics describe configuration of adsorbed molecules on a molecular level, Density Functional Theory (DFT) for micro-mesopore size range are calculated. Adsorption potential depends on adsorptive-adsorptive and adsorptive-adsorbent interactions and considers geometrical considerations (pore geometry). For a given pressure and temperature DFT allows one to calculate the equilibrium density profile for a fluid confined in a pore of given geometry, this leads to a calculation of theoretical adsorption isotherms for a given pore width of an adsorptive-adsorbent system. Generation of "kernel" to fit this analysis which consist of up to or more than 100 theoretical, individual pore isotherms. In this case, wood derived carbons were assumed to contain slit-like and cylindrical pores due to the wood morphology, therefore kernels used for N_2 measurements were "N_2 at 77K on carbon (slit/cylindrical pores, QSDFT adsorption branch)" whereas for CO_2 ones, a Monte Carlo model was used.

3 Results

3.1 Pre-Oxidation

The first observable change in the samples from experiments were mass loss and shrinkage. Pre-oxidation treatment shows the first trend in mass loss in Figure 32. The five different

temperatures follow a progressive decrease in mass loss, where lower temperatures such as 250°C and 275°C remain the highest yields with only 20% and 32% lost respectively. 287°C yields 47% loss which is quite in the middle point of the diagram, while the highest temperatures 300°C and 325°C overpass the middle point with 62% and 68% respectively.

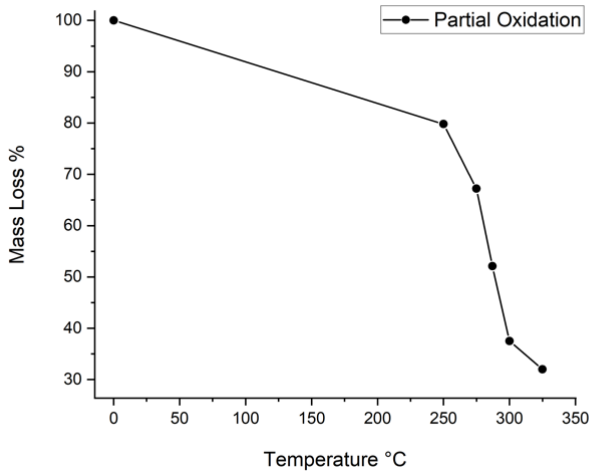

Figure 32: Partial oxidation of wood from this thesis.

On the other hand, shrinkage from pre-oxidation was measured and the trend is shown in Figure 33, where the main three axis were affected differently. Three trends are observable respectively for tangential, radial and axial directions. Tangential direction is the most affected in all the samples by average, followed by radial with a slightly lower values and axial in a lower extent. This might be due to the cell-wall arrangement in wood, where S1 and S2 layers are aligned to the ECF's orientation, while in tangential and radial direction the matrix elements are more prone to shrink in between the cellulose fibers where hemicellulose is placed.

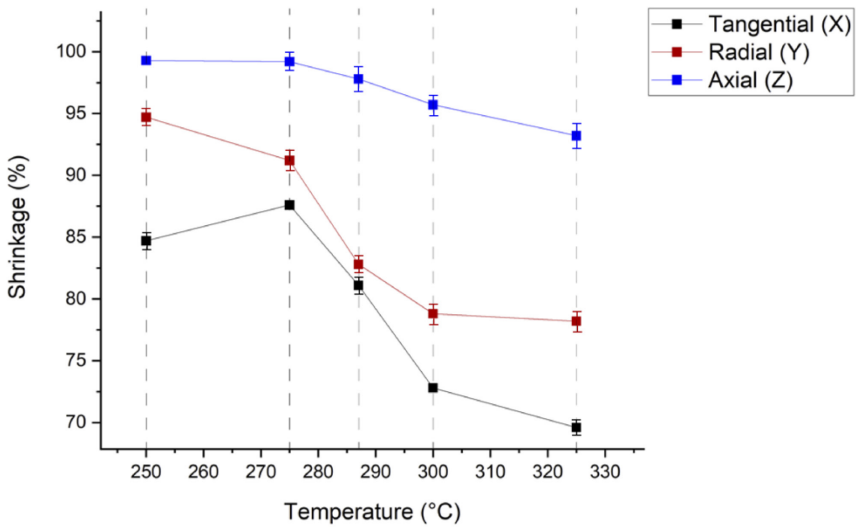

Figure 33: Shrinkage values on the three main directions for pre-oxidized samples, on each vertical dashed line.

First resulted X-ray patterns were the pre-oxidation treatment ones, which were studied in a hole sector of the integrated pattern. This sector 3 was declare the main differentiator of the results for the intensity curves, shown in the Figure 34, which were shifted up and down to fit the power law proximate to 0.4 at a same point to be able to analyze them in a qualitative way.

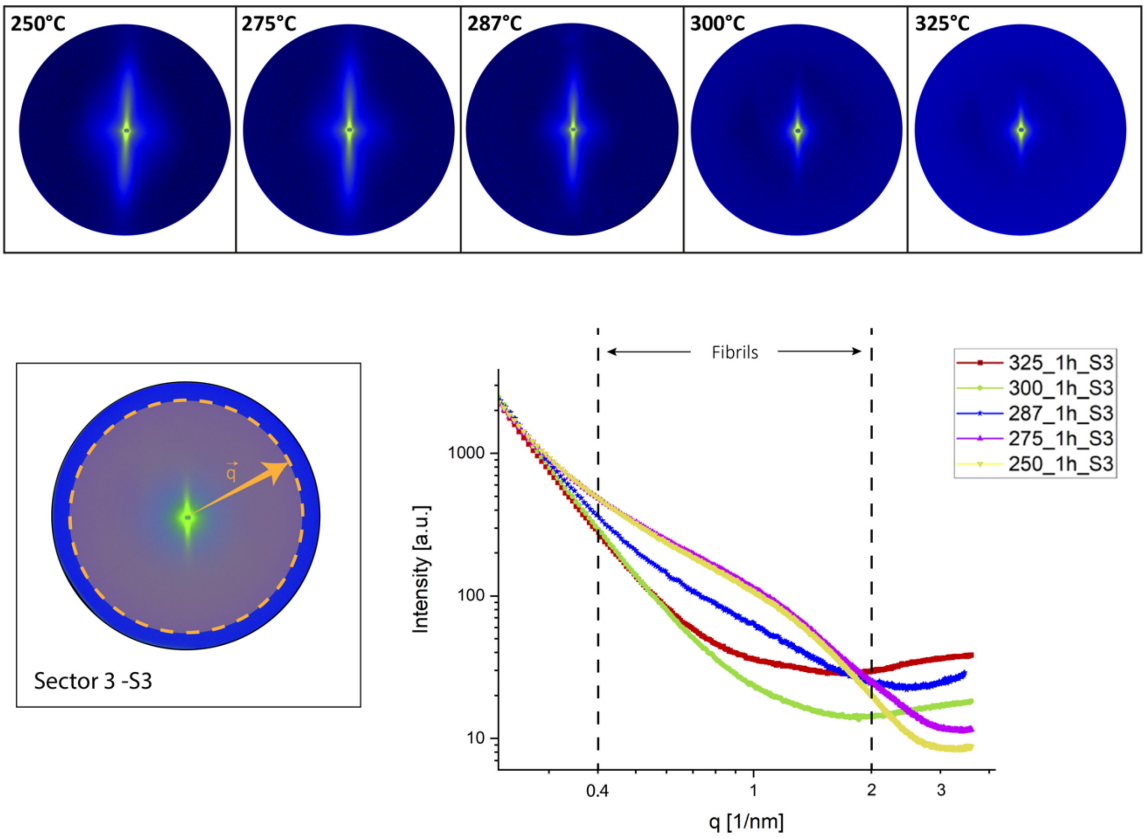

Figure 34: SAXS intensity curves after partial oxidation treatment on sector 3. Curves were fixed at a normal value to make them even to show in the diagram and compare.

The samples can be further analyzed qualitatively based on their power law scattering behavior. A representative example for the 1D scattering function $I(q)$ SAXS curves show the scattering intensity as a function of q for five different partial oxidation temperatures, the intensity patterns differ between these temperatures, reflecting changes in the nanostructure of the cellulose fibrils and their surrounding matrix of hemicellulose and lignin due to oxidation treatment. The q ranges that are differentiated in Figure 34 refer to the scale of fibrils between q= 0.4 nm^{-1} and q=2 nm^{-1} range, observable in real scale of $\frac{\pi}{q} = 7{,}8 - 1{,}6\ nm$ approximately. In the first range, where 250°C and 275°C display high intensity curves followed by a shoulder, which means the phase density contrast between cellulose and matrix is still relevant and oxidation process has almost not affected the structure, this might lead to a less degraded structure while hemicellulose has not decomposed. In contrast, 287°C shows an intensity decrease at the same q range, providing a steeper curve, followed by 300°C and

325°C where no shoulder is observable, indicating similarities in phase density contrast between cellulose and matrix, leading to a degraded structure by what could be a completed decomposition of hemicellulose. The 287°C curve is relevant due to the not completed degradation of the structure where still some phase density contrast differences. Therefore, a partial decomposition effect on 287°C is observable with some hemicellulose remaining in the structure.

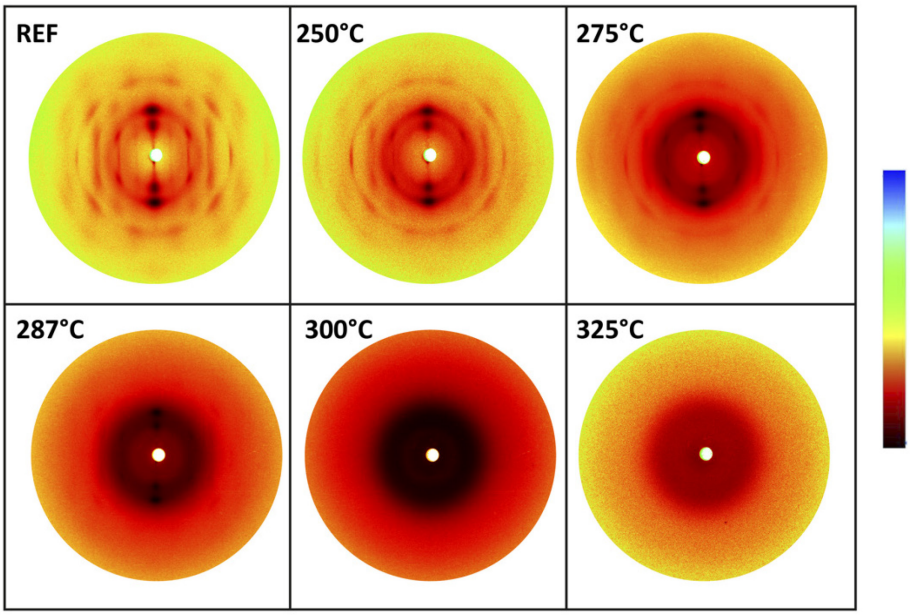

Figure 35: Pre-oxidation treatment WAXD 2D patterns, where high intensity is related with dark colors.

The resulted WAXD 2D patterns from Figure 35 show the structural evolution of wood through pre-oxidation. From 250°C, where the crystallinity of cellulose looks intact, observing the main peaks at (020) and (110) + $(1\bar{1}0)$ previously described in Figure 10. 275°C shows the same arrangement with not many differences, conserving the orientation on the (020), (110) and $(1\bar{1}0)$ planes. This changes with 287°C pattern, where a more diffuse pattern is found, as an extensive breakdown of the crystalline regions, where (020), (110) and $(1\bar{1}0)$ orientations still observable as well as an amorphous dark ring, most probably due to the hemicellulose partial decomposition. 300°C and 325°C show exclusively this amorphous ring only with uniform intensity, where the cellulose structure is already degraded and shifting at elevated temperatures, following the SAXS curves is elucidated the temperature steps as no degradation (250-275°C), partial degradation (287°C), and complete degradation (300-325°C).

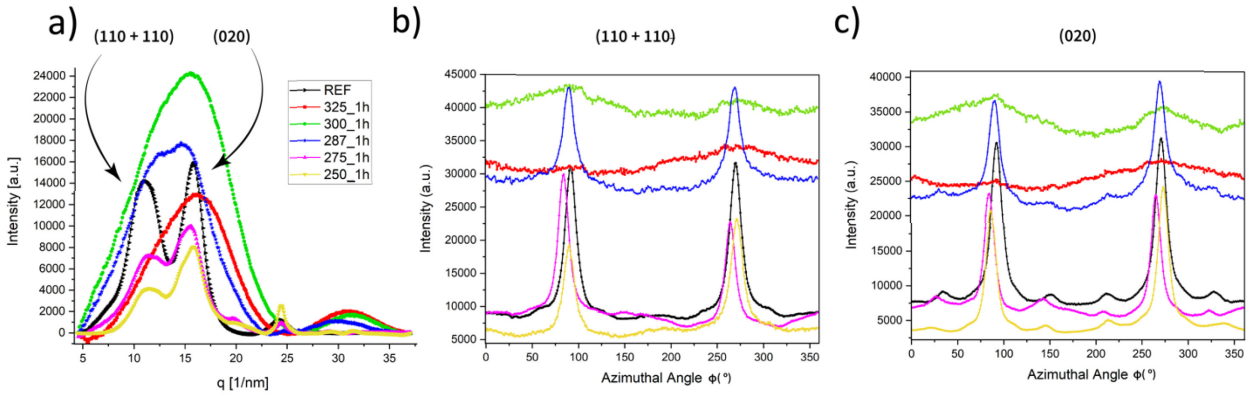

Figure 36: WAXD intensity curves from partial oxidation treatment and azimuthal integration of the two main peaks from cellulose (110 + 020).

The WAXD diagram and azimuthal intensity distribution for cellulose peaks, in Figure 36, displays intensity versus q (nm^{-1}) and versus azimuthal angle for the pre-oxidation step, where intensity peaks indicate the crystalline nature and structural ordering of the native cellulose structure, as observed on the REF curve, which belongs to the non-pre-oxidized wood sample. The prominent peak observed between q= 10-15 nm^{-1} is characteristic of the (110) and ($1\bar{1}0$) planes, and between q=15-20 nm^{-1} is characteristic of the (020) plane of crystalline cellulose, for 250°C is appreciable the small peak at q=25nm^{-1} which relates the feature with Ewald sphere cut for the 004 being visible in the WAXD TIFF image (Figure 10). From REF to the lower temperatures a diminish in intensity is observed, which is related with the cellulose small degradation. Then from 250°C to 287°C curves, both (110), ($1\bar{1}0$) and (020) peaks increase the intensity while merging together, as seen in azimuthal distribution, 287°C keeps the orientation at some extent for both peaks. 300°C and 325°C show first an increase in intensity and then a steep decrease between q=10-20 nm^{-1}, where crystalline peaks no longer retain the orientation for 325°C.

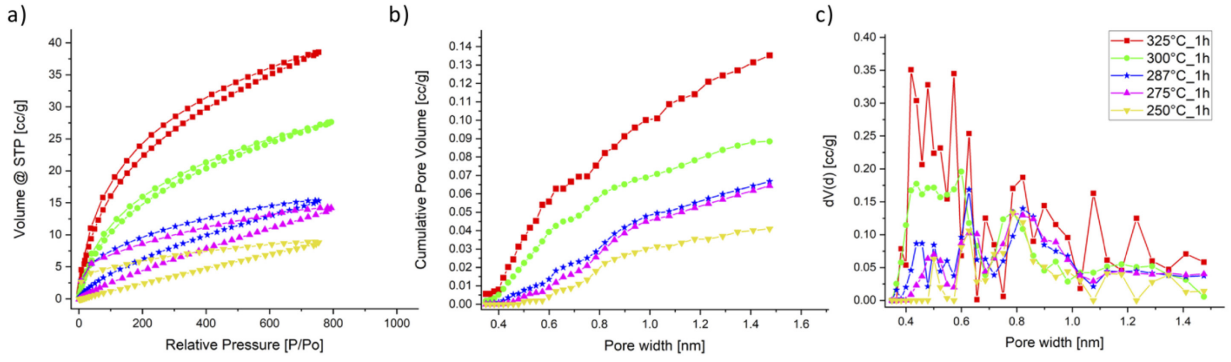

Figure 37: CO_2: a) isotherms, b) cumulative pore volume, c) pore size distribution from oxidation treatment.

Gas sorption analysis with CO_2 as adsorbate at 273K displays the adsorption volume versus the relative pressure of the isotherms registered (Fig. 37-a). First observation is that pre-oxidation samples are not yet fully carbonized, therefore their analysis must be focused on

the trends and main features, without correlating carbon states yet. The highest adsorption volume is achieved at 325°C, then 300°C follows with slightly lower adsorption capacity. 287°C, 275°C and 250°C samples exhibit progressively lower adsorption volumes. This reveals significant insights into the porosity evolution of partial oxidation treatment, related with the mass loss and enhancing the pore volume uptake. Nevertheless, low volume values describe a difficult morphology to be studied due to the incomplete carbonized form and pellet-like shape. N_2 analysis at 77K was tried with partial oxidation (see Appendix A.I). Cumulative pore volume diagram (Fig. 37-b) shows a main trend as in the isotherms, directly related with increasing the temperature of partial oxidation, the more volume is up taken, counting the main steps in pore width where this happens. 325°C shows the highest adsorption volume across the entire pressure range, indicating a significant development of porous structures, 300°C follows with a slightly lower adsorption capacity, and 287°C, 275°C and 250°C with less developed porosity show progressively the lower adsorption volumes. The pore size distribution curves (Fig. 37-c) show that 325°C sample has prominent distribution of micropores centered around 0.4 - 0.6 nm, with secondary peaks extending to about 1.2 nm. This indicates a well-developed network of micropores. At 300°C significant presence but fewer prominent peaks, indicating a relatively more uniform pore distribution compared with 325°C. 287°C, 275°C and 250°C show fewer distinct peaks, containing fewer micropores.

	mass loss (%)	SSA (m^2/g)	Pore Vol. (cc/g)	Pore Width Ø (nm)
325_1h	68	407,8	0,135	0,438
300_1h	62,5	274,1	0,089	0,600
287_1h	47,9	172,3	0,067	0,627
275_1h	32,8	156	0,064	0,785
250_1h	20,2	98,7	0,041	0,785

Table 4. Mass loss, SSA, Pore volume and pore width diameter values from oxidation treatment.

In Table 4 data extracted from gas sorption analysis indicate the main qualitative differences between oxidation samples. High SSA values are correlated with higher mass loss and shrinkage, which indicates the more opened structure as a factor of the oxidation process, then follows pore volume which also increase and therefore pore width shrinks due to the densification of the structure at high temperatures, due to the destruction or amorphous arrangement, while in lower temperatures, due to the minimum mass loss and shrinkage, keeping pore spaces or structure inside almost intact.

3.2 Pyrolysis 1

Then pyrolysis thermal treatments show the structural decomposition, first in mass loss from partial oxidation evolution, as seen in Figure 38, where approximately all the samples finish with a 20-25% mass remaining but 300°C showed a mass loss more proximately to 30% remaining, slightly lower compared to the rest. Nevertheless, the samples exhibit similar mass loss, which indeed open speculations on how microstructure is oriented and for each partial oxidation temperature, how evolves within the pore structure analysis. Shrinkage values show the radial and tangential axes are the main directions to shrink after pyrolysis, observing higher shrinkage on the non-pre-oxidated sample and the lowest on 300°C.

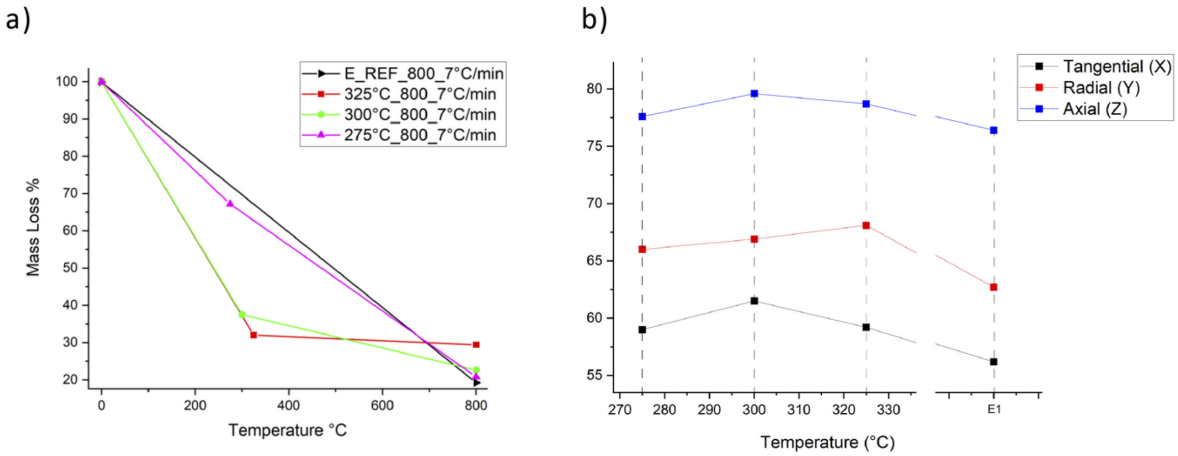

Figure 38: Pyro 1: a) cumulative mass loss and b) cumulative shrinkage.

The 2D SAXS patterns obtained from the second pyrolysis process are shown in Figure 39, where the ones on the sides remain more appreciable peaks intensities, related to 275°C and REF 1 non partially oxidized, then quite lower peaks in the center for 300°C and 325°C showing still a vertical strike. Nevertheless, SAXS is somehow ambiguous in interpretation, because of cracks between cells and cell wall layers, a realistic judgement of preferred pore orientation is only valid at larger q values, where the influence of cracks should be small, and only in concern with preferred carbon orientation from WAXD.

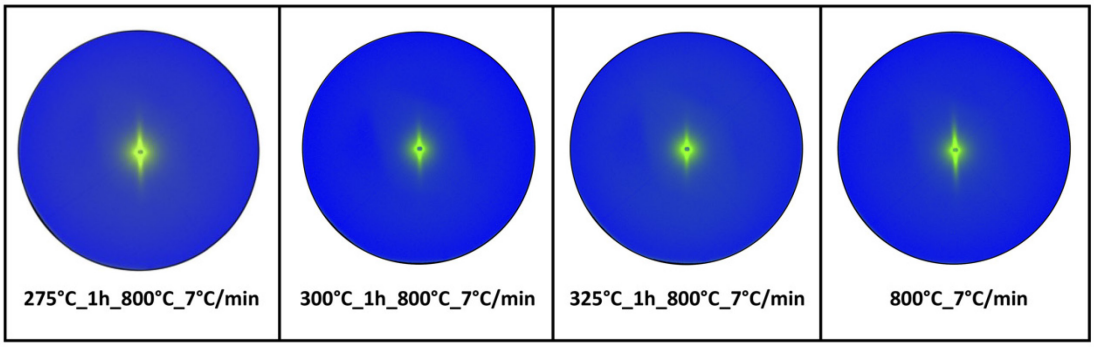

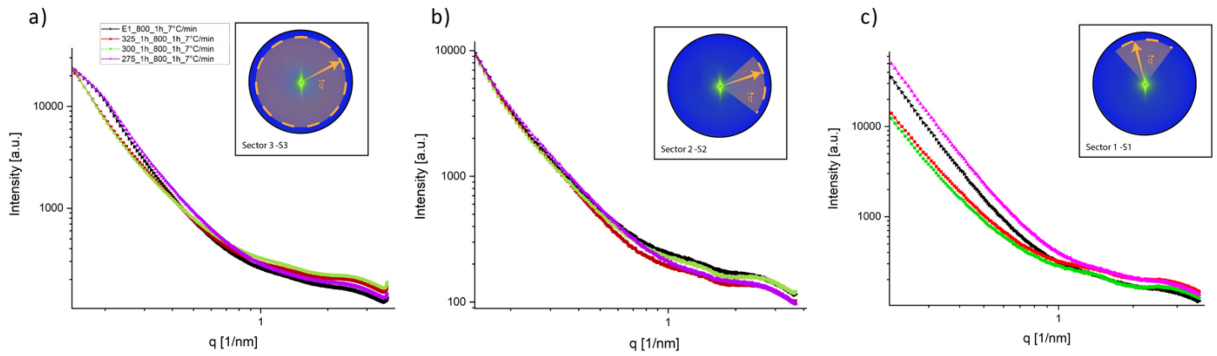

Figure 39: SAXS patterns from PYRO 1 and intensity curves from the three sectors.

In this case for pyrolyzed treatment at 800°C with a heating rate of 7 °C/min, SAXS data is divided by sectors where the first hole integration of the azimuthal angle is shown, followed by sector 2 and sector 1 respectively (Figure 39 a-b-c). For sector 3, the presence of larger pores or less compact structures could be prominent on the lower oxidation temperatures, where 275°C reveals a slightly higher intensity. 325°C and 300°C display similar scattering intensities, quite lower than 275°C but a bit higher than the direct 800°C reference without oxidation step. The similarity in the slopes across the curves at mid to high q values suggest that the microporous features may be comparable across all samples. Sectors 2 and 1 are shown, noticing higher intensities in sector 1 where all the main scattering point are recorded, which means more pronounce curves, but is found in both small shoulders from the remaining structural orientations, nevertheless As an overall description, Pyro 1 seems to result in degraded structures for almost all the samples.

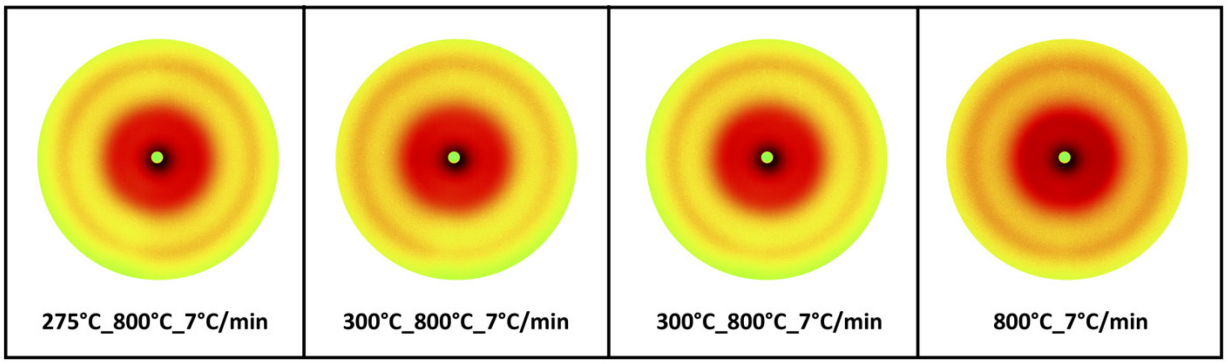

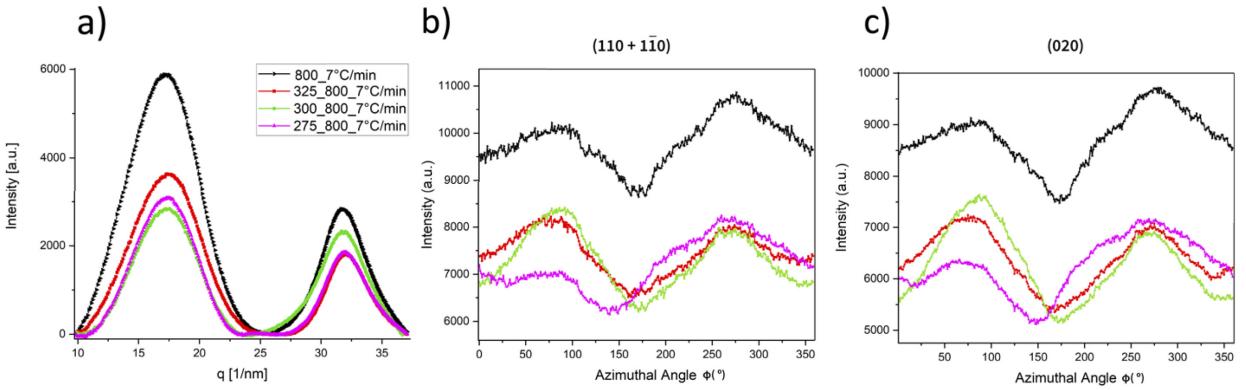

Figure 40: WAXD 2D patterns, a) intensity curves versus q vector and b), c) versus azimuthal intensity distribution on the cellulose peaks (110 and 020, respectively), from PYRO 1 treatment.

WAXD data shows the main distribution of the peaks through the structure (Fig. 40), where the main peak at q=8-20nm^{-1} is associated with (002) plane, a secondary peak at q= 30-35nm^{-1} may represent (100) plane, indicative of carbon structures forming from cellulose during pyrolysis. The highest trends are shown by non-pre-oxidized sample, directly pyrolyzed at 800°C, followed by 325°C, 275°C and 300°C progressively with lower intensities. For the azimuthal intensity distribution, peaks from cellulose positions remain some orientation, as it is observed the peaks at 90° and 270°. In Table 5 are shown the crystallite sizes (La, Lc) for each sample.

	mass loss (%)	La (Å)	error (Å)	Lc (Å)	error (Å)	Average number of graphene layers in [002] direction	error
E1_800_7°C /min	80,8	23,02	0,71	8,15	0,41	2,20	0,01
325_800_7°C /min	80,6	26,10	1,00	8,38	0,47	2,30	0,01
300_800_7°C /min	77,4	24,17	0,49	9,22	0,38	2,55	0,01
275_800_7°C /min	79,2	24,17	1,47	9,42	0,55	2,57	0,01

Table 5: WAXD intensity curves of pyrolyzed treatment at 800°C for 1 hour with a heating rate of 7°C/min.

There exists a correlation with the results and the pre-oxidation temperatures, as the temperature increases, higher lateral growth appears, and distance between layers get closer, shrinking and allowing a denser structure, highlighting non-pre-oxidized sample showing the lowest La and Lc values.

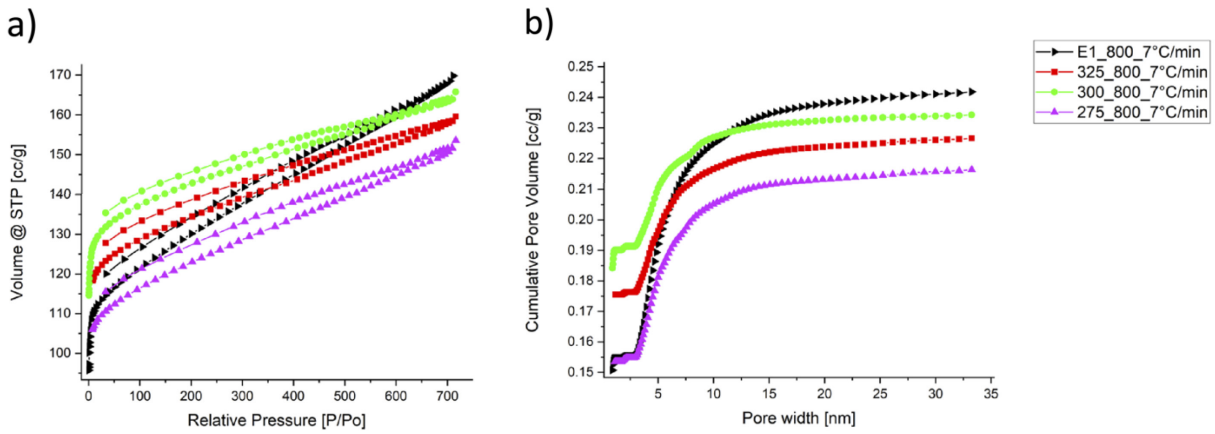

Figure 41: Gas sorption Analysis with N2 at 77K of pyrolyzed treatment at 800°C for 1 hour with a heating rate of 7°C/min. a) Isotherms b) Cumulative Pore Volume.

Nitrogen at 77K isotherms (Fig. 41) shows the trends in volume uptake against relative pressure for Pyro 1. All isotherms display Type IV behavior with a hysteresis loop indicating the presence of mesopores alongside micropores, the cumulative pore volume shows those steps where the volume is taken at different pore widths. 300°C shows the highest adsorption volume among all the samples, indicating a well-developed porous structure and significant surface area. 325°C and E1 exhibit similar adsorption behavior, with slightly lower volumes than 300°C but higher than 275°C where is observed the lowest adsorption volume, suggesting a less-developed porous structure and surface area compared to the other samples. This quantitative analysis is in parallel considered with CO_2 measurements as qualitative analysis focusing on Specific Surface Area (SSA), Pore volume and pore width properties.

For CO_2 gas sorption analysis on Pyro 1, isotherms (Fig. 42-a) display the trends showing 300°C as the highest overall adsorption volume followed by 325°C and E1, with slightly lower adsorption volumes, indicating good porosity although their structure may be less optimal compared to 300°C. 275°C has the lowest adsorption volume, indicating less developed microporous network and lower adsorption capacity. In cumulative pore volume diagram (Fig. 42-b) is observed mostly similar trends with 300°C as the highest cumulative pore volume trend and 325°C and E1 following. 275°C shows the lowest cumulative pore volume, consistent with more restricted pore structure.

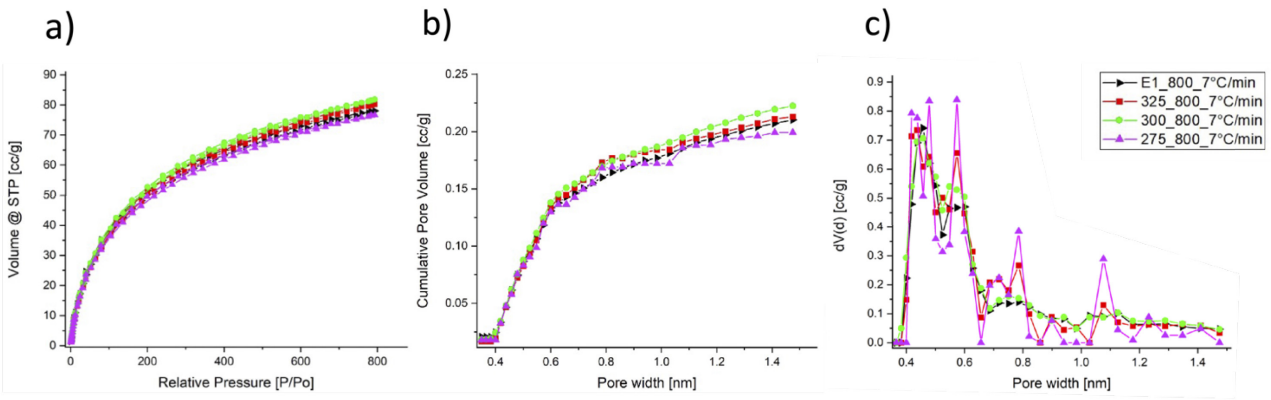

Figure 42: CO_2 at 273K of pyrolyzed treatment at 800°C for 1 h with a heating rate of 7°C/min gas sorption: a) isotherms b) cumulative pore volume, c) pore size distribution.

Here in pore size distribution trends (Fig. 42-c) 300°C shows significant favorable microporous structure against the other samples, with a pore distribution centered around 0.4-0.6 nm, characteristic of micropores that are effective for CO_2 adsorption. 325°C and E1 show similar distribution but less pronounced peaks, while 275°C indicates a notable distribution at smaller widths but not prominent peak as in 300°C sample, indicating fewer micropores. In Table 6 is shown the SSA, Pore volume and Pore width values from gas sorption data.

	mass loss (%)	SSA (m^2/g)	Pore Vol. (cc/g)	Pore Width Ø (nm)
E1_800_7°C /min	80,8	743,09	0,211	0,458
325_800_7°C /min	80,6	752,34	0,213	0,438
300_800_7°C /min	77,4	780,03	0,223	0,458
275_800_7°C /min	79,2	717,28	0,199	0,573

Table 6: Gas sorption data from Pyro 1.

The maximum SSA is observable in 300°C with also the highest pore volume due to the increased porosity. While 275°C shows limited pore formation due to insufficient degradation of structural components. For this pyrolysis treatment, 300°C is the one which better performance achieved indication good microporosity and highest surface area.

3.3 Pyrolysis 2

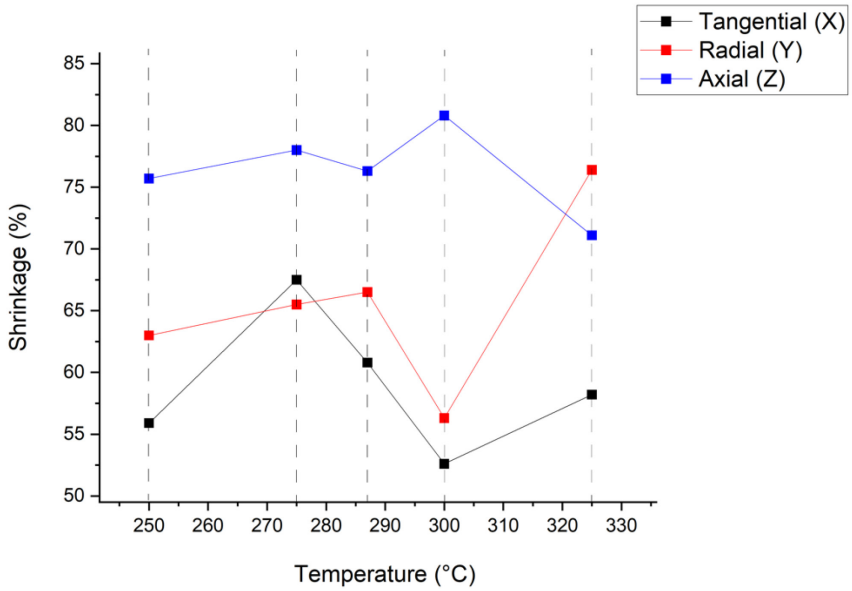

Figure 43: Shrinkage diagram after Pyro 2 treatment, each dashed vertical line refers to each temperature from pre-oxidation treatment.

Shrinkage on Pyro 2 is shown in Figure 43, where trends on axial direction indicate the lower shrinkage orientation, similar to prior Pyro 1, although some disparities are observed first on 275°C where radial shrinks more than tangential. This could be result of sample irregularities on the surface at the time to measure every axis, as well as for 325°C where radial shows less shrinkage than axial orientation, which is not possible in wood. These values are very similar, and their trends do not differ too much in comparison with previous wood pyrolysis studies mentioned in the introduction part.

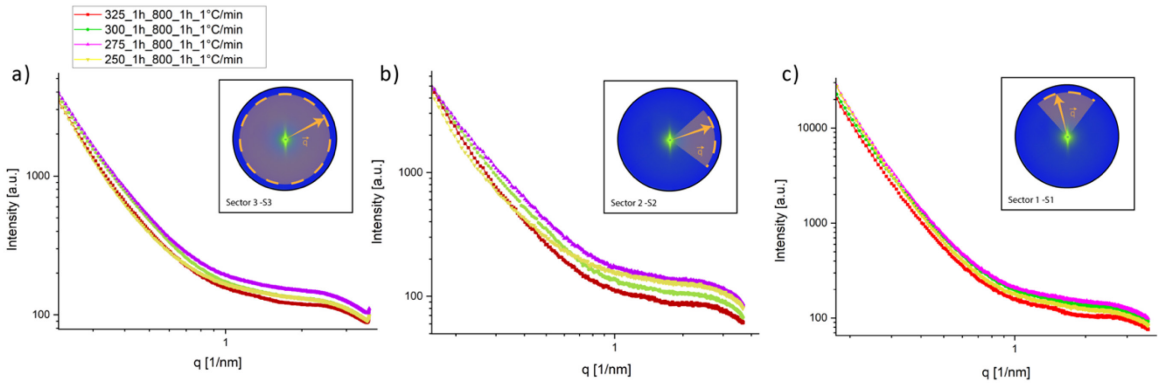

Figure 44: SAXS intensity curves analysis by sectors from Pyro 2 samples.

In Figure 44, SAXS curves from three sectors show 325°C as the lowest scattering intensity at low q, with a denser structure. 300°C is slightly higher but still low, not as denser at 325°C structure, on the other hand, 275°C shows higher intensity curve than previous ones and 250°C behaves similar. All four curves are in a range of low intensities, and very small shoulder or phase is observable at low q, which decrease for almost all the samples indicates the diffuse structure originated, but not possible to identify if there is any preferred orientation. The structure appears almost amorphous for the higher temperatures, while keeping a vertical pattern. For the second sector diagram 325°C curve shows the lowest intensities at low q, while 250°C indicates a steeper decrease as well as in sector 3, conserving most of the structure or more organized as in 275°C with the highest intensity, besides that, degradation and extinction of the structure in the 325°C is observable, while the rest show the same trend as in sector 3. Sector 1 shows the same trend as previous diagrams with 325°C as the lowest intensity level, but in all the curves a slightly higher intensity values, due to the main peaks are vertically oriented. This case 250°C shows much flatter step than in sector 2.

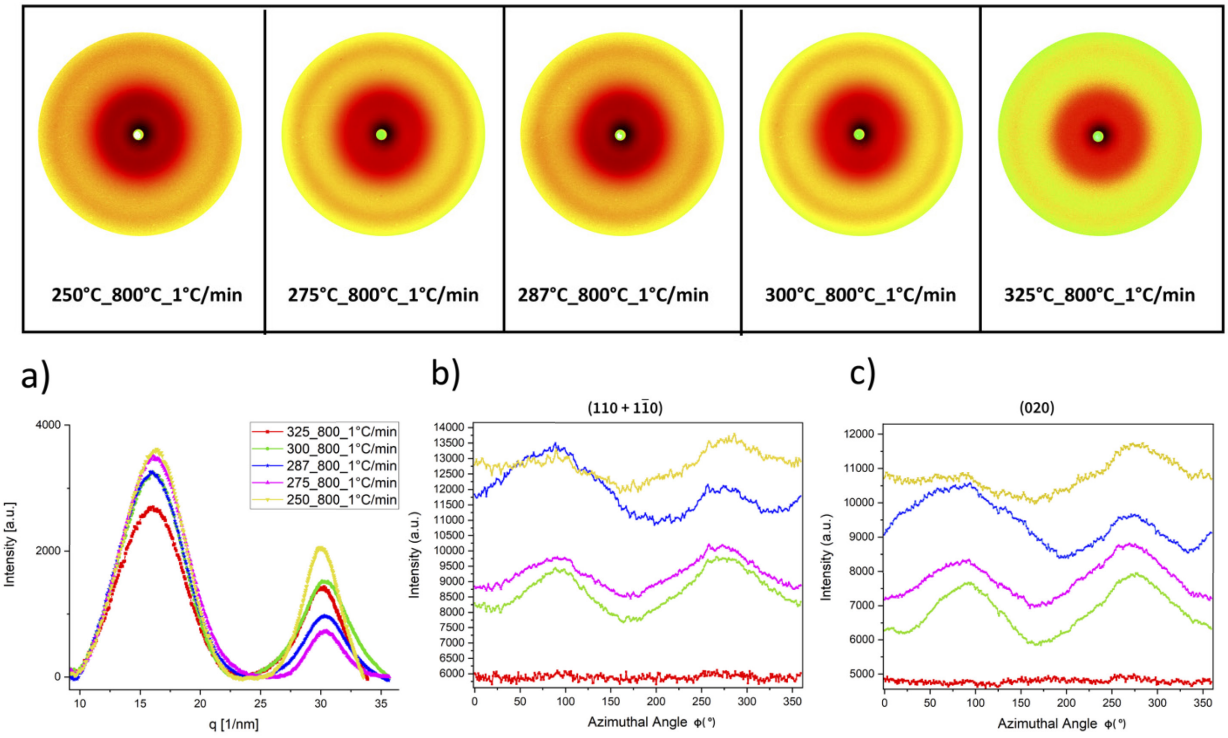

Figure 45: WAXD 2D patterns, a) intensity curves versus q vector and b), c) versus azimuthal intensity distribution on the cellulose peaks (110 and 020, respectively), from Pyro 2 treatment.

WAXD 2D patterns from Pyro 2 (Figure 45) show the diffused ring at low q values due to the carbonization step and development of (002) peak of the structure, as observed previously in Pyro 1. Here as well, a ring on high q values refers to the (100) peak development. Azimuthal intensity distribution shows the original cellulose peaks still remaining small orientation, similar as in Pyro 1. In table 7, data from the crystallites sizes is shown, where 275°C exhibits

the largest La (33,69 Å) representing several lateral structural growths. Higher oxidation temperatures resulted in reduced La and similar degradation, where Lc remained similar between every sample, as well as mass loss, therefore oxidation emphasizes the changes in crystallinity more than bulk decomposition due to laterals microstructural changes rather than vertical in the (002) direction.

	mass loss (%)	La (Å)	error (Å)	Lc (Å)	error (Å)	Average number of graphene layers in [002] direction	error
325_800_1°C /min	80,4	28,36	0,48	8,47	0,36	2,26	0,0
300_800_1°C /min	79,2	22,70	0,61	8,94	0,44	2,27	0,01
287_800_1°C /min	78,2	24,23	0,58	9	0,34	2,29	0,01
275_800_1°C /min	79,4	33,69	0,21	9,05	0,27	2,33	0,01
250_800_1°C /min	80,4	30,06	0,31	8,71	0,35	2,38	0,01

Table 7: Crystallite sizes from Pyro 2 samples.

The gas sorption analysis with Nitrogen at 77K for the pyrolyzed treatment at 800°C for 1 hour with a heating rate of 1°C/min study the isotherms and cumulative pore volume trends, despite of the not completed desorption branch as seen in Figure 46-a for the isotherms diagrams. A Type IV a) isotherm is clear from the IUPAC classification. 300°C achieves the highest adsorption volume, indicating a well-developed porous network, follows 325°C with a slightly lower adsorption volume and 250°C and 275°C show progressively lower adsorption volumes. Cumulative pore volume diagram (Fig. 46 b) indicates that 300°C has the highest cumulative pore volume followed by 325°C with slightly lower values between 0.2 and 0.22 cc/g. 250°C and 275°C have lower cumulative pore volume related to the same trends as in the isotherms.

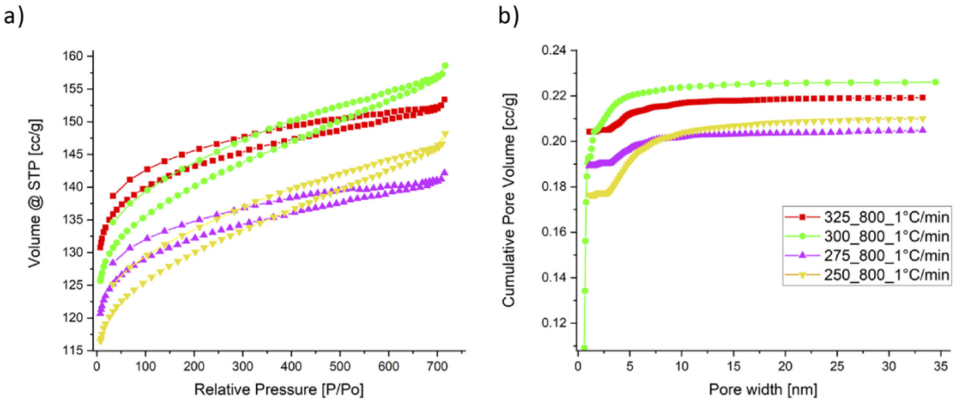

Figure 46: Gas sorption Analysis with N2 at 77K Pyro 2. a) Isotherms b) Cumulative Pore Volume.

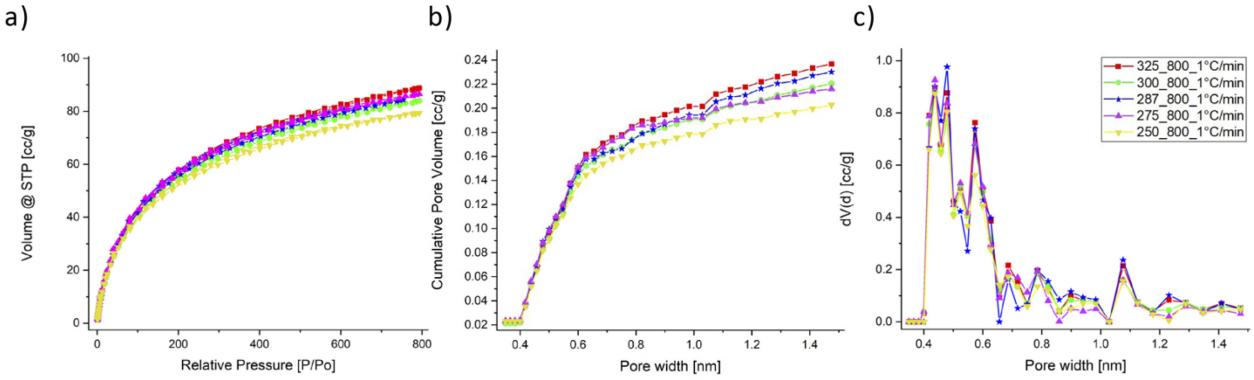

Figure 47: Gas sorption analysis with CO_2 at 273K from Pyro 2. a) Isotherms, b) Cumulative pore volume.

The CO_2 sorption analysis of pore size distribution In Figure 47-a), Isotherm curve of 325°C indicates the highest adsorption capacity correlated to a well-developed microporous structure, follows 300°C and 287°C with slightly lower adsorption volumes. The 275°C and 250°C show progressively lower adsorption volumes. In Figure 47-b) cumulative pore volume diagram shows the trends for 325°C with the highest cumulative pore volume, with the same progressively trend downwards for the rest of the samples, observing 250°C the lowest cumulative pore volume. Pore size distribution is shown in Figure 47-c, where the presence of micropores centered around 0.4-0.6 nm across all samples is observable. Some differences indicate a little enhancement in pores of 1.2 nm for 287°C upon the rest, while for smaller pores 287°C shows a less uniform distribution. 275°C indicates the highest volume in those smaller pores, similar as 325°C. The lowest temperature sample 250°C has the lower volumes for the pore size distribution compared to the rest.

	mass loss (%)	SSA (m^2/g)	Pore Vol. (cc/g)	Pore Width Ø (nm)
325_800_1°C /min	80,4	840,6	0,237	0,438
300_800_1°C /min	79,2	790,7	0,220	0,438
287_800_1°C /min	78,2	818,4	0,230	0,458
275_800_1°C /min	79,4	802,9	0,216	0,438
250_800_1°C /min	80,4	745,4	0,203	0,438

Table 8: Gas sorption data from Pyro 2.

In Table 8 SSA, Pore Volume and Pore width values for the samples are shown. It is observable the clear enhanced porosity on the 287°C partial oxidation temperature, which shows higher SSA and a significant pore volume and higher pore width in comparison with the others, also

the lowest mass loss between the ones in similar range. 325°C achieves the highest porosity, with higher pore volume and lower pore width, indicating that higher temperatures allow the enhancement of structural decomposition to increase porosity. 250°C which has the lowest SSA and pore volume, shows this incomplete decomposition without effective porosity development.

3.4 Pyrolysis 3

The third pyrolysis process was proceeded under vacuum conditions and same heating rate as in Pyro 2 of 1°C/min. Shrinkage data as a cumulative value from pre-oxidation treatment is shown in Figure 48, where trends show the higher yield in tangential direction for 287°C, while similar values as compared to Pyro 1 are observed, here the non-preoxidized sample shows the highest shrinkage.

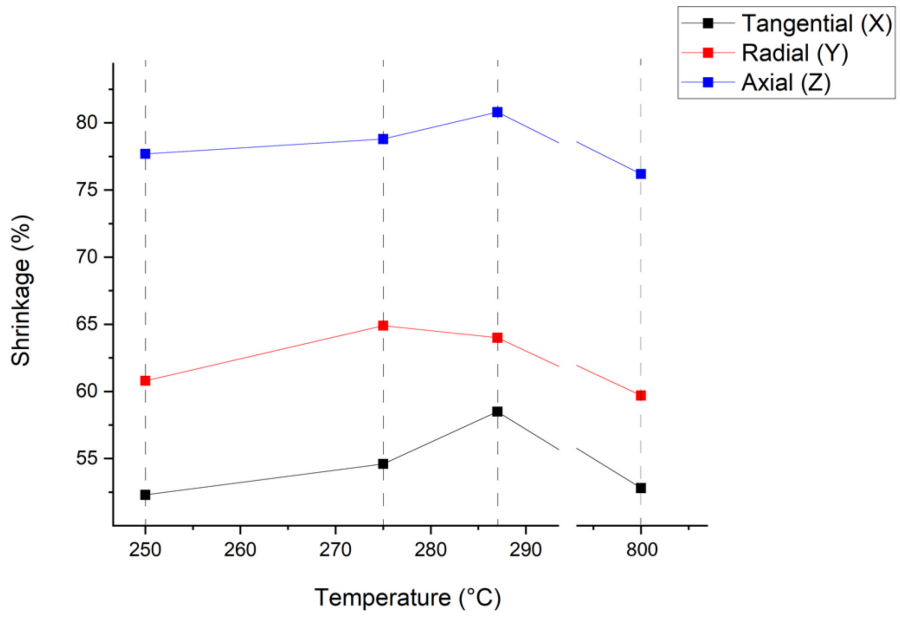

Figure 48: Shrinkage diagram from Pyro 3.

WAXD patterns shown in Figure 49 exhibit the amorphous ring arrangement, with no clear or visible orientation, nevertheless if look closely, the concentrical ring is more appreciable in the middle (Fig. 50-b), which maybe with longer exposures more accurate orientation could be achieved. It is also shown the absence of air doesn't affect different the patterns with same heating rate.

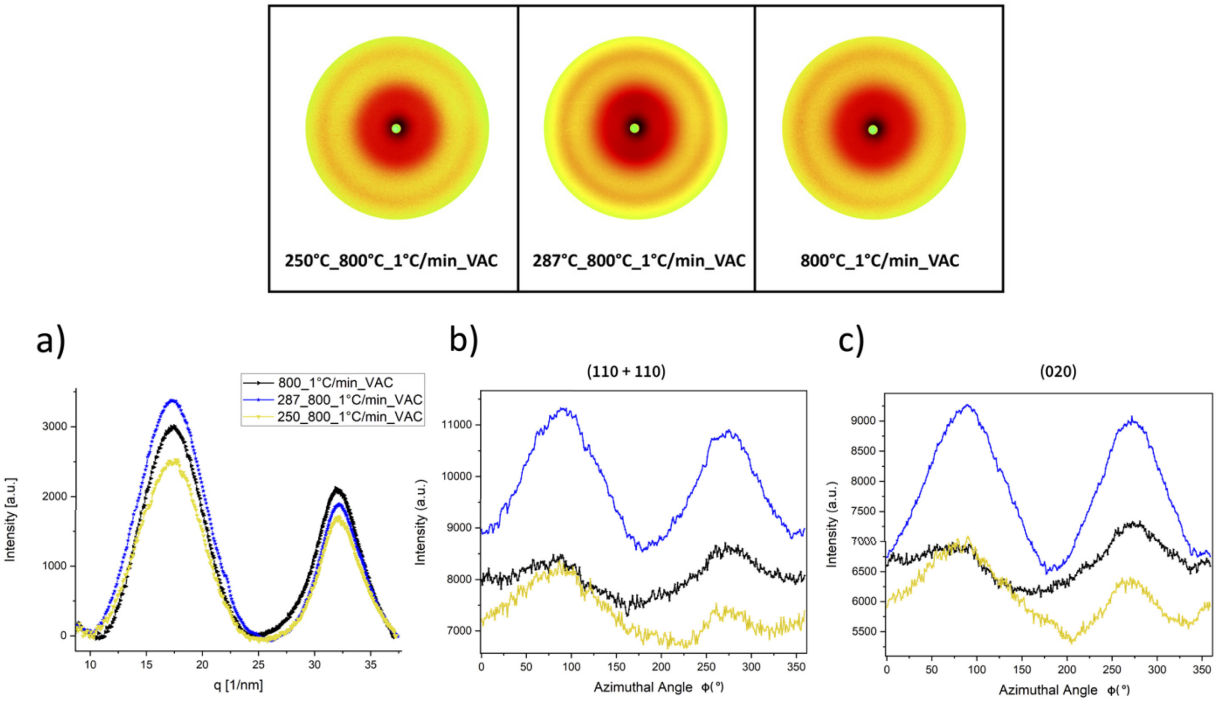

Figure 49: WAXD 2D patterns, a) intensity curves versus q vector and b), c) versus azimuthal intensity distribution on the cellulose peaks (110 and 020, respectively), from Pyro 3 treatment.

WAXD patterns shown in Figure 50 from pyrolyzed at 800°C for 1 hour, with a heating rate of 1°C/min and under vacuum are observable the same peaks for (002) and (100) as observed in Pyro 2 under Nitrogen atmosphere, while here 287°C shows a more development orientation than 250°C and non-preoxidized sample. Azimuthal intensity distribution indicates same behavior for the maintaining of oriented peaks from cellulose, pointing out the highest orientation for this process for 287°C. In table 9 data from the crystallites is shown, where non-preoxidized sample exhibits the largest La (24,15 Å) representing several lateral structural growths. Lc remained similar between the three samples, while 287°C yields the most.

	mass loss (%)	La (Å)	error (Å)	Lc (Å)	error (Å)	Average number of graphene layers in [002] direction	error
E2_800_1°C /min_VAC	83,1	24,15	0,45	9,14	0,41	2,51	0,01
287_800_1°C /min_VAC	79,4	23,77	0,60	8,27	0,24	2,25	0,00
250_800_1°C /min_VAC	82,4	23,52	1,01	8,46	0,60	2,30	0,01

Table 9: Crystallite sizes from Pyro 3 samples.

Gas sorption analysis can reflect the behavior during pyrolysis under vacuum, where low pressure values were an issue with nitrogen measurements, nevertheless some data was acquired shown in Figure 53. 250°C and 275°C isotherms are not closed but is possible to see

some features such as the volume uptake, which is higher for 275, according to the more decomposed structure and lower for 250°C. The cumulative pore volume shows the trends in the steps where the uptake takes place related with pore sizes, where for 275°C is higher volume in two steps, 250°C shows same trend at lower volume values.

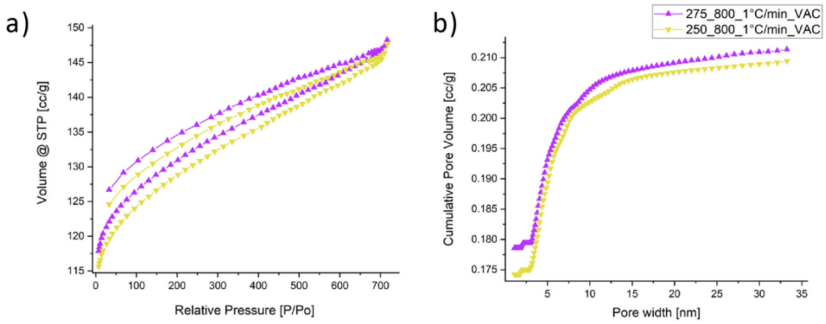

Figure 50: Gas sorption analysis with N_2 at 77K from Pyro 3. a) Isotherms, b) Cumulative pore volume.

CO_2 isotherms, CPV and PSD (Figure 51) show the trends for 287°C as the higher volume compared with the rest, this might be due to the controlled environment kinetics reactions, lower heating rate under vacuum enhancing the volume uptake for the sweet spot from oxidation step. The rest of the samples show similar trends in PSD, commonly a bimodal pore size is observed at 0.4 and 0.6 nm size, similar to previous Pyrolysis steps, with a small difference at CPV, where the non-preoxidized sample shows higher amount of volume uptake around 0.7-0.8 nm pore sizes, and lower after 1.2, opposite as 250°C and 275°C, showing less open pores sizes of 0.7 and wider at 1.2.

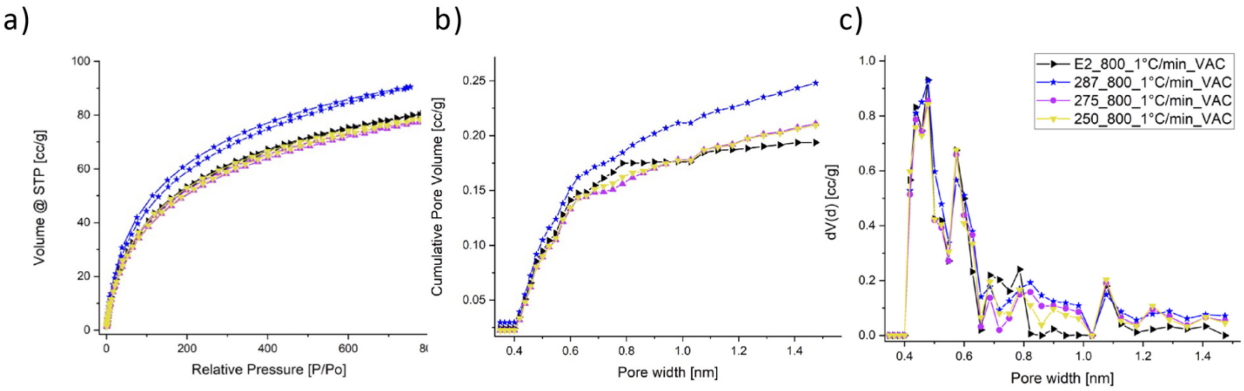

Figure 51: Gas sorption analysis with CO_2 at 273K from Pyro 3. a) Isotherms, b) Cumulative pore volume, c) Pore size distribution.

In table 10 quantitative values from gas sorption analysis are shown, comparing between different pore volume, achieved the higher for 287°C, but same pore width in all the samples, which indicates controllable pore width under vacuum, also has the lowest mass loss and highest SSA. Nevertheless, SSA can't be reliable very much due to the non-fidelity within the

carbon layers arrangement, that might be blocked different pore spaces or conducts. These expectations are evaluated after considering the issues with nitrogen measurements and data from CO_2.

	mass loss (%)	SSA (m^2/g)	Pore Vol. (cc/g)	Pore Width Ø (nm)
E2_800_1°C /min_VAC	83,1	739,1	0,194	0,479
287_800_1°C /min_VAC	79,4	877,7	0,248	0,479
275_800_1°C /min_VAC	82,6	746	0,211	0,479
250_800_1°C /min_VAC	82,4	748,4	0,209	0,479

Table 10: Gas sorption data from Pyro 3.

3.5 Activation

Activation step was the last thermal treatment, only realized on four samples, from two different heat treatments, showing their diffraction patterns in Figure 52 respectively, where is possible to observe similar features, diffused ring in the center, very weak. These patterns show similarities with previous pyrolysis showing no ellipses or diffraction peaks.

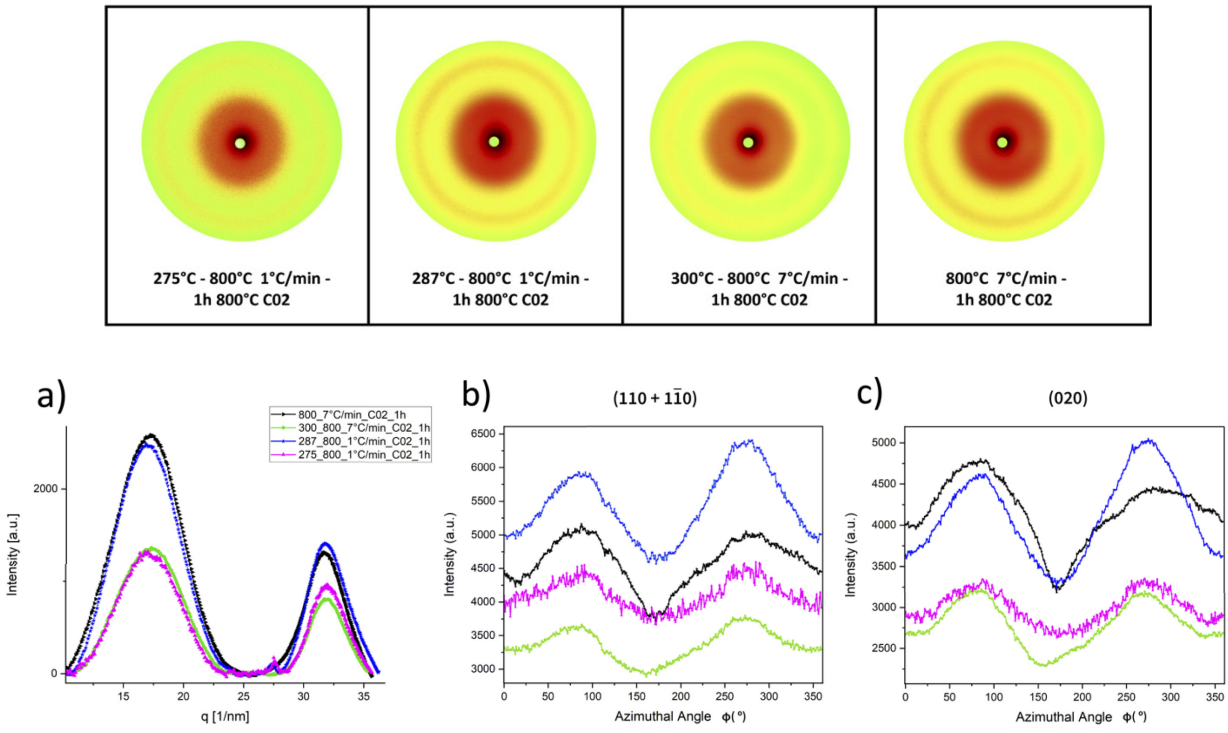

Figure 52: WAXD 2D patterns, a) intensity curves versus q vector and b), c) versus azimuthal intensity distribution on the cellulose peaks (110 and 020, respectively), from Activation treatment.

Figure 52 shows the trends from the intensity curves, as well as the orientation remaining on the celliulose peaks, observing 287°C keeping the highest remaining orientation. Intensity versus q position shows different peaks heights, pointing out the higher values on 287°C and non-preoxidized sample. Table 11 the crystallite sizes, where in plane shows lower values than 275°C and slightly higher in 002, but not much difference. This indicates that 275°C has suffered less shrinkage in the radial and tangential orientations as in 287°C, also mass loss is a big effect that indicates big differences between these two. 287°C almost lost 28 % from pyro to activation, where 275°C up to 65%. The error in these values is a 5% for 287°C respect to the small amount of material that was used. In the other hand, non-preoxidized and 300°C samples show similar mass loss, 31% and 39% respectively, and similar La and Lc sizes.

ACTIVATED CO_2 - 800°C - 1h	mass loss rel. (%)	La (Å)	error (Å)	Lc (Å)	error (Å)	Average number of graphene layers in [002] direction	error
275_800_1°C /min	65,22	29,86	1,15	9,20	0,66	2,62	0,01
287_800_1°C /min	28,12	25,95	2,39	9,05	0,30	2,41	0,01
300_800_7°C /min	39,22	29,52	0,84	8,82	0,31	2,44	0,00
E1_800_7°C /min	31,71	29,94	0,28	8,50	0,26	2,31	0,00

Table 11: Crystallite sizes from Activation samples.

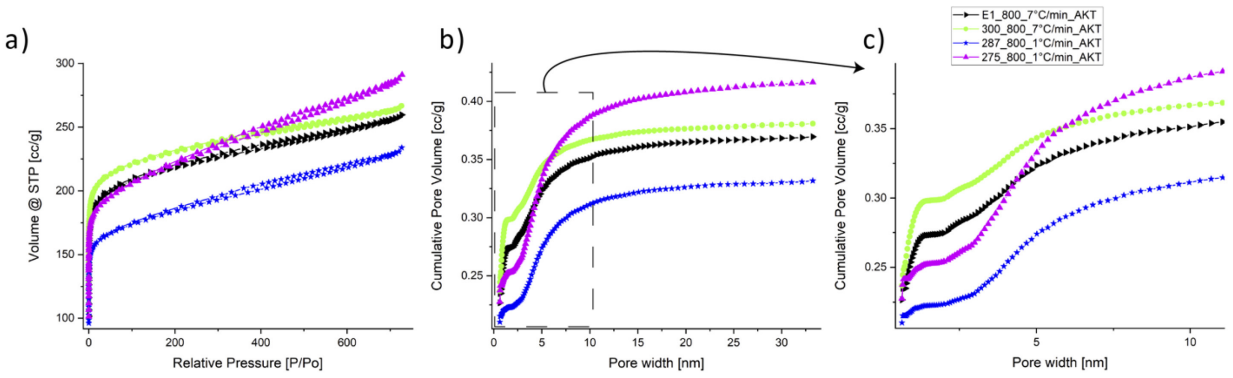

Figure 53: Gas sorption analysis with CO_2 at 273K of activation treatment at 800°C for 1 hour with CO2. a) Isotherms, b) Cumulative pore volume.

In Figure 53 nitrogen gas sorption isotherms and CPV are shown from activated samples, where 275°C shows the highest volume uptake and 287°C the lowest, while pyro 1 samples have similar isotherms. For CPV different steps are observed, while 300°C and non-pre-oxidized show steep uptake curves at low pore width sizes, 275°C and 287°C show less pronounced increased uptake curves at low sizes (0-5 nm). Is possible to say that 275°C has an increased uptake around 5 nm pore width size, while the others increase at lower sizes but similar overall.

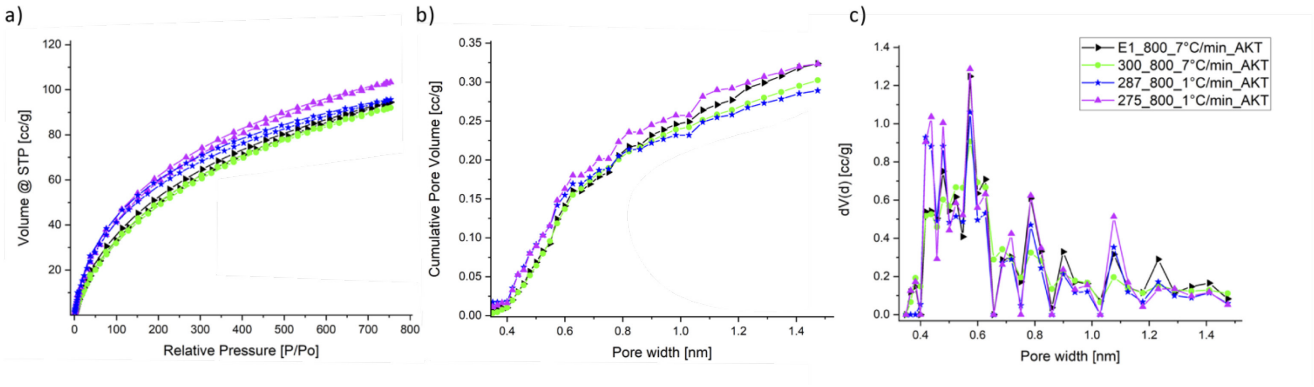

Figure 54: Gas sorption analysis with CO_2 at 273K of activation treatment at 800°C for 1 hour with CO2. a) Isotherms, b) Cumulative pore volume, c) Pore size distribution.

Gas sorption isotherms, CPV and PSD from CO_2 measurements are shown in Figure 54 respectively, where 275°C shows the highest pore volume, related with table 12, where the main quantitative values are shown. Isotherm also shows steep curve in comparison with the rest, which indicates good channels or microporosity connections, not expected from the temperature range right below the sweet spot at oxidation step. PSD shows different sizes, with prominent 0.6 nm and 0.4 but also at higher sizes, where non-preoxidized sample curve is over the rest. Last but not least, 287°C shows similar pore sizes as 275°C but definitely lower volume uptake with the lowest pore volume. All the samples show the same pore width, and highest SSA in 275°C followed by non-preoxidized and 287°C.

ACTIVATED CO_2 - 800°C - 1h	mass loss rel. (%)	SSA (m^2/g)	Pore Vol. (cc/g)	Pore Width Ø (nm)
275_800_1°C /min	65,22	1032,9	0,324	0,573
287_800_1°C /min	28,12	948,6	0,289	0,573
300_800_7°C /min	39,22	921,4	0,302	0,573
E1_800_7°C /min	31,71	967,1	0,324	0,573

Table 12: Gas sorption data from Activation.

4 Discussion of Results

Results from experiments revealed crucial insights into the transformation of hierarchically structured wood into carbon materials through controlled thermal treatments. One of the most significant findings is identifying the optimal pre-oxidation temperature of 287°C, which facilitated selective hemicellulose decomposition while preserving aspects of the original cellulose structure. The diminishing density phase contrast in SAXS and the reduction of cellulose peaks in WAXD confirmed that structural decomposition followed a controlled

pathway, suggesting that hemicellulose removal altered the lignocellulosic matrix while maintaining the fundamental alignment of cellulose fibrils to some extent. With increasing oxidation temperatures, the material evolved toward a more amorphous structure, as evidenced by WAXD patterns showing reduced crystallinity at 300°C and 325°C. Beyond this temperature range, excessive mass loss disrupted the structural hierarchy, diminishing the possibility of controlled porosity and alignment retention.

Subsequent pyrolysis treatments at 800°C with two different heating rates (1°C/min and 7°C/min) revealed significant trends: regardless of pre-oxidation temperature, all pyrolyzed samples underwent further amorphisation, leading to disordered turbostratic carbon structures. However, 287°C pre-oxidized samples exhibited the highest retention of preferred orientation (12%) as it is shown in Figure 55, particularly in Pyro 3 and Activation steps.

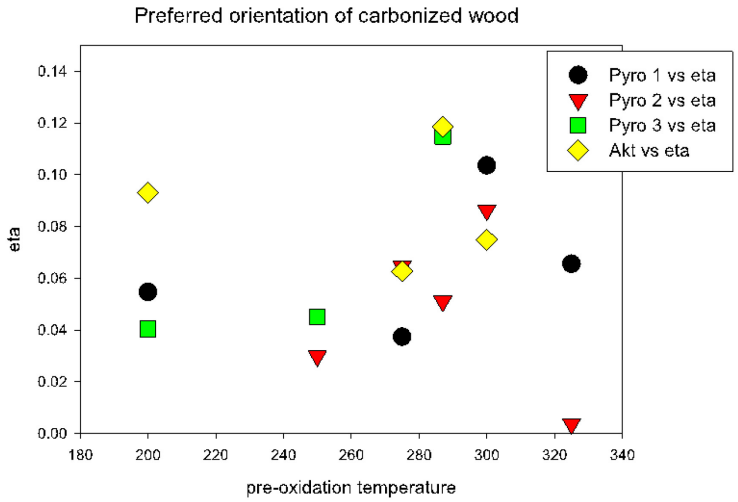

Figure 55: Degree of preferred orientation over all thermal treatments after pre-oxidation step. Every pre-oxidation temperature is located as vertically for each, while non-preoxidized samples are shown in the range of 200 °C.

The azimuthal intensity distributions from WAXD further confirmed this finding, indicating that structural alignment was not entirely lost, even after high-temperature treatments. These results highlight that pre-oxidation at 287°C provides a structural advantage, allowing for tailored porosity while partially maintainning wood's intrinsic anisotropy. Gas sorption experiments provided additional insights into porosity formation: CO_2 activation at 800°C for 1 h significantly enhanced micropore development. Nitrogen gas sorption measuremnts proved unreliable due to the non-ideal interactions between nitrogen's quadrapole moment and the carbonized surface, requiring a pressure adjustment from 10^{-5} to 10^{-3}, yet still lacking precision although trends in cummulative pore volume align with CO_2 ones, which in contrast provided more reliable data, allowing for detailed analysis of SSA and PSD too.The 287°C pre-oxidized and activated samples exhibited a balanced microporosity structure, maintaining some anisotropic characteristics in combination with SAXS and WAXD observations.

Analyzing the preferred orientation in biological-derived carbon materials presents inherent challenges. The Ewald sphere effect introduces complications, as well as detector tilting, sample rotation, surface irregularities or beam center determination, which resulted an issue with WAXD patterns, where the peak at about 35 nm^{-1} is way to high, therefore WAXD peak positions are not perfectly positioned due to the manually background removal entire process and fitting curves process. This not strongly influence the results, while only partially deviated curves are shown in this thesis, previous studies [33] on similar materials indicate these possible issues as main possible influence in azimuthal intensity distributions. The complexity of integrating sector-based SAXS patterns highlights the need for further methodological refinements, as for example the analysis on higher q values in SAXS interpretation, due to the lower influence of cracks at those ranges. Overall, this study provides compelling evidence that pre-oxidation at 287°C is a key factor in controlling structural degradation while maintaining partial orientation in pyrolyzed carbons.

5 Conclusions

This study has demonstrated that thermal pre-oxidation plays a crucial role in controlling the structural integrity of lignocellulosic materials during their transformation into nanoporous carbons with some anisotropy. The experimental results indicate that 287°C represents an optimal temperature for partial hemicellulose decomposition, which helps retain aspects of the natural alignment of cellulose fibrils. Higher pre-oxidation temperatures led to excessive material loss and amorphization, while lower temperatures did not sufficiently modify the lignocellulosic matrix to promote the desired porosity development. To improve the partial degradation process and enhance structural preservation at high pyrolysis temperatures, future research should explore the use of chemical stabilizers and protective coatings. Potential strategies include phosphoric acid or boron-based treatments to form thermally stable layers around cellulose fibrils, reducing excessive shrinkage and disordering at elevated temperatures. Additionally, mild crosslinking agents could help reinforce the lignocellulosic matrix, mitigating amorphization while promoting selective decomposition. Furthermore, controlled gas-phase treatments using oxygen-limited environments could allow for gradual structural modifications, ensuring greater control over pore formation while maintaining intrinsic anisotropy.

In summary, the findings of this study offer valuable insights into the thermal treatment of lignocellulosic materials for nanoporous carbon applications. By fine-tuning pre-oxidation conditions and exploring novel stabilization techniques, bio-derived carbon materials can be further optimized for filtration, energy storage, and catalytic applications, paving the way for high-performance, sustainable alternatives to conventional carbon materials.

6 References

[1] C. Sanchez, H. Arribart, M. Madeleine, and G. Guille, “Biomimetism and bioinspiration as tools for the design of innovative materials and systems,” 2005. [Online]. Available: www.nature.com/naturematerials

[2] E. Dujardin and S. Mann, “Bio-inspired materials chemistry,” *Advanced Materials*, vol. 14, no. 11, pp. 775–788, 2002, doi: 10.1002/1521-4095(20020605)14:11<775::AID-ADMA775>3.0.CO;2-0.

[3] W. Kaabar, A. Laklouk, O. Bunk, M. Baily, M. J. Farquharson, and D. Bradley, “Compositional and structural studies of the bone-cartilage interface using PIXE and SAXS techniques,” in *Nuclear Instruments and Methods in Physics Research, Section A: Accelerators, Spectrometers, Detectors and Associated Equipment*, Elsevier B.V., Jul. 2010, pp. 78–82. doi: 10.1016/j.nima.2010.01.040.

[4] D. Van Opdenbosch, G. Fritz-Popovski, O. Paris, and C. Zollfrank, “Silica replication of the hierarchical structure of wood with nanometer precision,” *J Mater Res*, vol. 26, no. 10, pp. 1193–1202, May 2011, doi: 10.1557/jmr.2011.98.

[5] A. S. Deshpande, I. Burgert, and O. Paris, “Hierarchically structured ceramics by high-precision nanoparticle casting of wood,” *Small*, vol. 2, no. 8–9, pp. 994–998, Aug. 2006, doi: 10.1002/smll.200600203.

[6] C. E. Byrne and D. C. Nagle, “Carbonization of Wood for Advanced Materials Applications,” Baltimore, Sep. 1996.

[7] Y. Zuo *et al.*, “Recent advances in wood-derived monolithic carbon materials: Synthesis approaches, modification methods and environmental applications,” May 01, 2023, *Elsevier B.V.* doi: 10.1016/j.cej.2023.142332.

[8] R. D. Preston, “PHILOSOPHICAL TRANSACTIONS The Organization of the Cell Wall of the Conifer Tracheid.” [Online]. Available: https://royalsocietypublishing.org/

[9] R. Hori and M. Wada, “The thermal expansion of wood cellulose crystals,” *Cellulose*, vol. 12, no. 5, pp. 479–484, Oct. 2005, doi: 10.1007/s10570-005-5967-5.

[10] R. Bacon and M. M. Tang, “Carbonization of Cellulose Fibers-II, Physical Property Study,” Pergamon Press Ltd, 1964.

[11] C. E. Byrne and D. C. Nagle, “Carbonized Wood Monoliths-Characterization,” 1997.

[12] R. Asakura, M. Morita, K. Maruyama, H. Hatori, and Y. Yamada, “Preparation of fibrous activated carbons from wood fiber,” 2004.

[13] G. Dorez *et al.*, “Effect of cellulose, hemicellulose and lignin contents on pyrolysis and combustion of natural fibers,” *J Anal Appl Pyrolysis*, p. 107, 2014, doi: 10.1016/j.jaap.2014.03.017ï.

[14] T. Hosoya, H. Kawamoto, and S. Saka, “Pyrolysis behaviors of wood and its constituent polymers at gasification temperature,” *J Anal Appl Pyrolysis*, vol. 78, no. 2, pp. 328–336, 2007, doi: 10.1016/j.jaap.2006.08.008.

[15] F. Cerciello *et al.*, “Xylan fast pyrolysis: An experimental and modelling study of particle changes and volatiles release,” *Fuel*, vol. 357, Feb. 2024, doi: 10.1016/j.fuel.2023.129983.

[16] M. M. Tang and R. Bacon, “Carbonization of Cellulose Fibers-I, Low Temperature Pyrolysis,” Pergamon Press Ltd, Ohio, 1964.

[17] W. Ruland, “X-ray studies on preferred orientation in carbon fibers,” *J Appl Phys*, vol. 38, no. 9, pp. 3585–3589, 1967, doi: 10.1063/1.1710176.

[18] L. Wang *et al.*, “Comparison of properties of biochar produced from different types of lignocellulosic biomass by slow pyrolysis at 600 °C,” *Applications in Energy and Combustion Science*, vol. 12, p. 100090, Dec. 2022, doi: 10.1016/j.jaecs.2022.100090.

[19] O. Paris, C. Zollfrank, and G. A. Zickler, “Decomposition and carbonisation of wood biopolymers - A microstructural study of softwood pyrolysis,” *Carbon N Y*, vol. 43, no. 1, pp. 53–66, 2005, doi: 10.1016/j.carbon.2004.08.034.

[20] O. Paris, *Handbook of textile fibre structure*, vol. 2. Cambridge, 2009.

[21] I. Lamata-Bermejo, M. D. Alba, and J. Ramírez-Rico, “Influence of the chemical activation with KOH/KNO3 on the CO2 adsorption capacity of activated carbons from pyrolysis of cellulose,” *J Environ Chem Eng*, vol. 12, no. 6, Dec. 2024, doi: 10.1016/j.jece.2024.114288.

[22] Harry. Marsh and F. . Rodríguez-Reinoso, *Activated carbon*. Elsevier, 2006.

[23] H. Lichtenegger, “The composite architecture of the wood cell wall - Nanostructure investigations with X-ray scattering,” Material Physics Institute, Wien, 1999.

[24] P. Dr. rer. nat. ,Dipl.-Chem. G. W. Dr. rer. sil. , Dipl.-H. Dietrich Fengel, “Wood Chemistry Fengel and Wegener,” 1989.

[25] J. Binswanger, “Josbin.ch.” Accessed: Nov. 22, 2024. [Online]. Available: https://josbin.ch/work/holzstrukturen/

[26] A. Reiterer, H. F. Jakob, S. E. Stanzi-Tschegg, and P. Fratzl, “Spiral angle of elementary cellulose walls of Picea abies determined by X-ray scattering,” Springer-Verlag, 1998.

[27] K. Juraić *et al.*, “GISAXS and GIWAXS analysis of amorphous-nanocrystalline silicon thin films,” *Nucl Instrum Methods Phys Res B*, vol. 268, no. 3–4, pp. 259–262, Feb. 2010, doi: 10.1016/j.nimb.2009.09.046.

[28] J. Als-Nielsen and D. McMorrow, *Elements of Modern X-ray Physics*, Second. John Wiley & Sons, Ltd, 2011.

[29] O. Paris and M. Müller, “Scanning X-ray microdiffraction of complex materials: Diffraction geometry considerations,” 2003. [Online]. Available: www.elsevier.com/locate/nimb

[30] K. Meyer and P. Klobes, “NIST recommended practice guide :,” Gaithersburg, MD, 2006. doi: 10.6028/NBS.SP.960-17.

[31] M. Thommes *et al.*, “Physisorption of gases, with special reference to the evaluation of surface area and pore size distribution (IUPAC Technical Report),” *Pure and Applied Chemistry*, vol. 87, no. 9–10, pp. 1051–1069, Oct. 2015, doi: 10.1515/pac-2014-1117.

[32] O. Paris *et al.*, *Structure and Multiscale Mechanics of Carbon Nanomaterials*. 2016. doi: 10.1007/978-3-7091-1887-0.

[33] Y. Zhang, O. Paris, N. J. Terrill, and H. S. Gupta, “Uncovering three-dimensional gradients in fibrillar orientation in an impact-resistant biological armour,” *Sci Rep*, vol. 6, May 2016, doi: 10.1038/srep26249.

7 Appendix

PRE-OXIDATION

WAXD data background removal via baseline manually applied in Origin

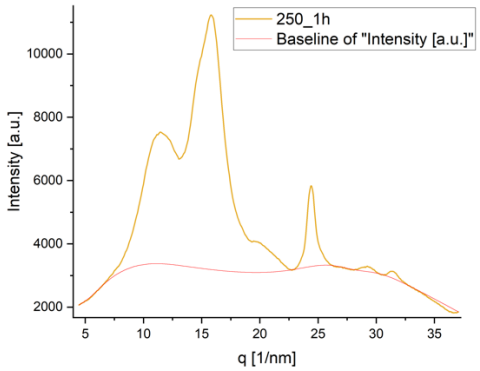

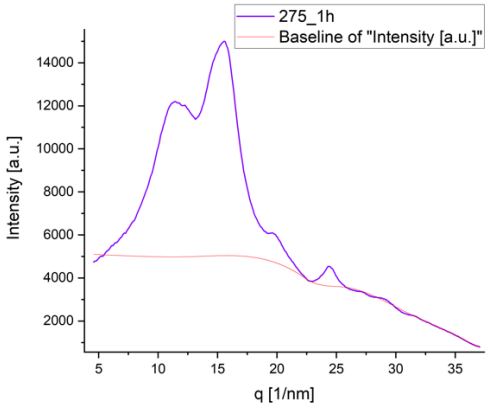

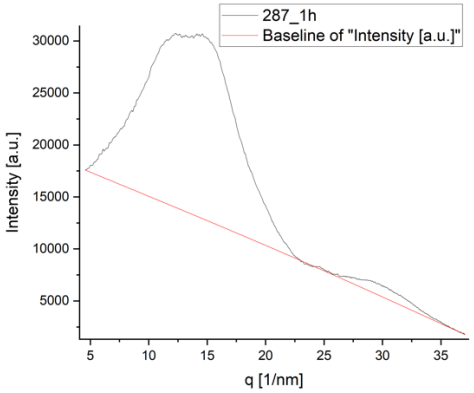

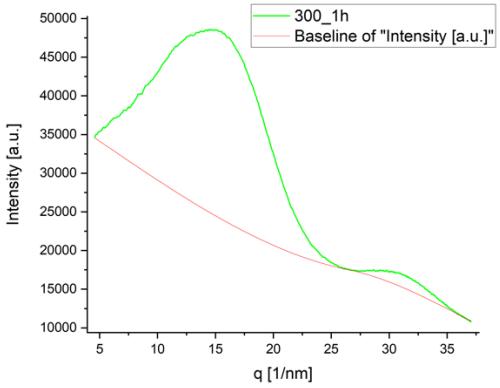

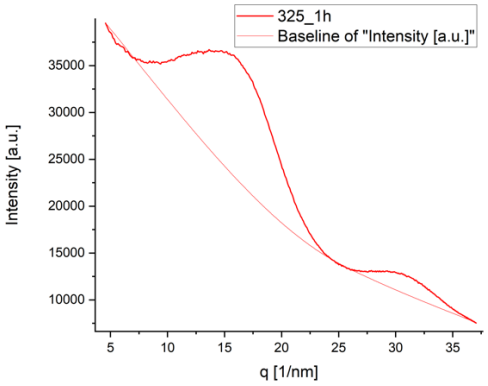

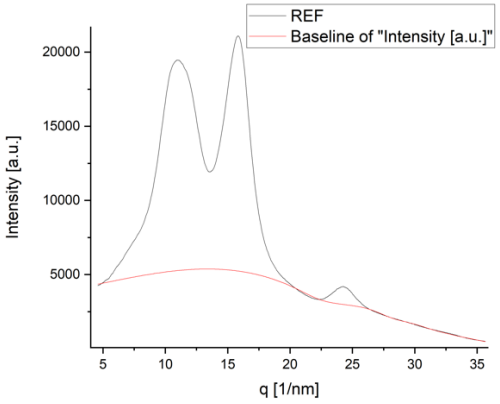

PYRO 1

WAXD

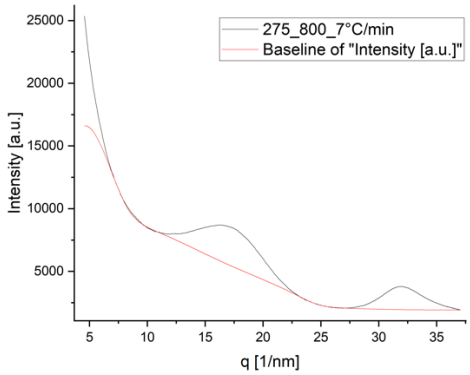
275_800_7°C/min
Baseline of "Intensity [a.u.]"
Intensity [a.u.]
q [1/nm]

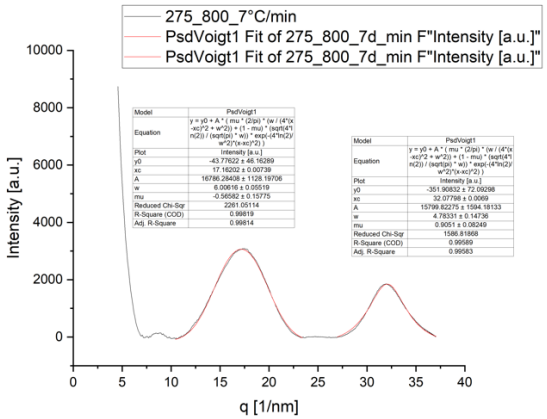
275_800_7°C/min
PsdVoigt1 Fit of 275_800_7d_min F"Intensity [a.u.]"
PsdVoigt1 Fit of 275_800_7d_min F"Intensity [a.u.]"
Intensity [a.u.]
q [1/nm]

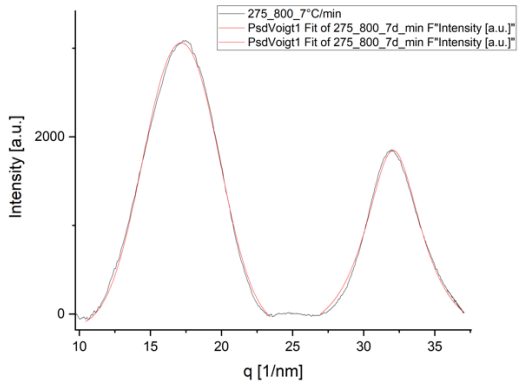
275_800_7°C/min
PsdVoigt1 Fit of 275_800_7d_min F"Intensity [a.u.]"
PsdVoigt1 Fit of 275_800_7d_min F"Intensity [a.u.]"
Intensity [a.u.]
q [1/nm]

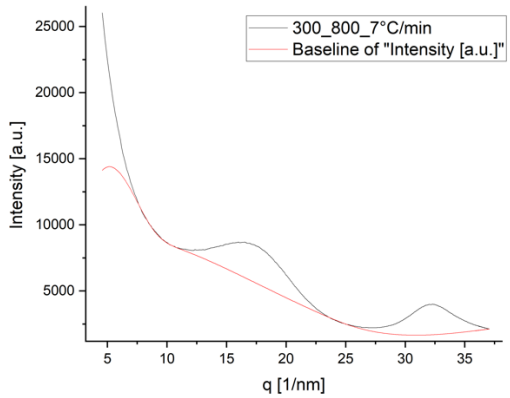
300_800_7°C/min
Baseline of "Intensity [a.u.]"
Intensity [a.u.]
q [1/nm]

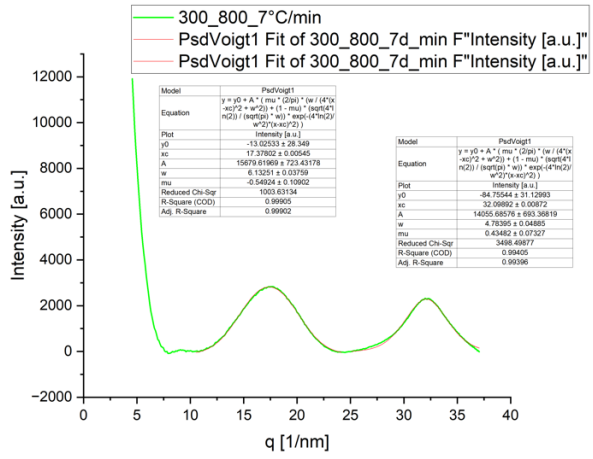
300_800_7°C/min
PsdVoigt1 Fit of 300_800_7d_min F"Intensity [a.u.]"
PsdVoigt1 Fit of 300_800_7d_min F"Intensity [a.u.]"
Intensity [a.u.]
q [1/nm]

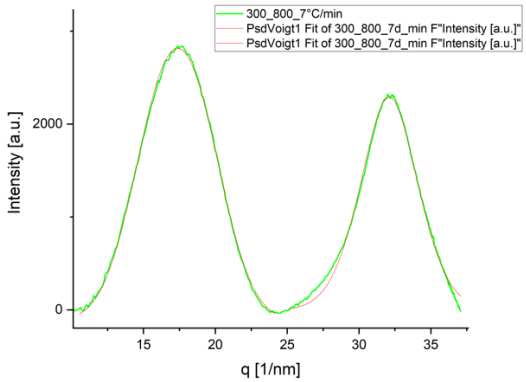
300_800_7°C/min
PsdVoigt1 Fit of 300_800_7d_min F"Intensity [a.u.]"
PsdVoigt1 Fit of 300_800_7d_min F"Intensity [a.u.]"
Intensity [a.u.]
q [1/nm]

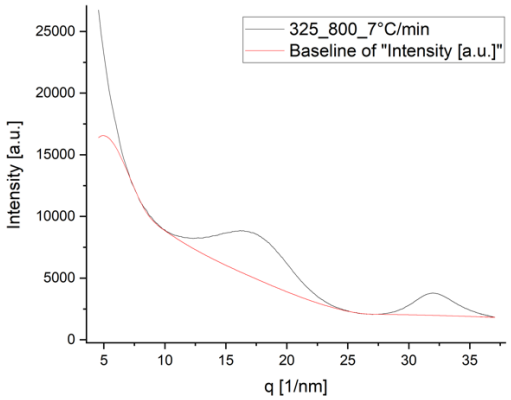
325_800_7°C/min
Baseline of "Intensity [a.u.]"
Intensity [a.u.]
q [1/nm]

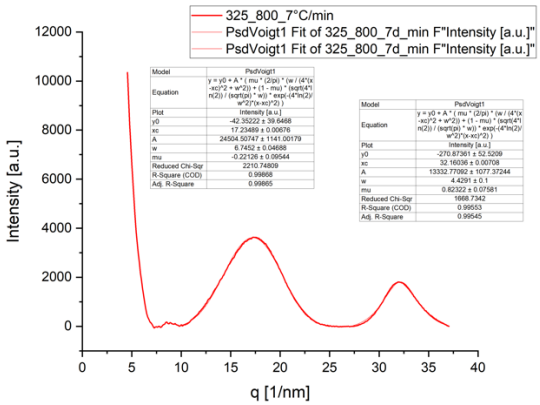
325_800_7°C/min
PsdVoigt1 Fit of 325_800_7d_min F"Intensity [a.u.]"
PsdVoigt1 Fit of 325_800_7d_min F"Intensity [a.u.]"
Intensity [a.u.]
q [1/nm]

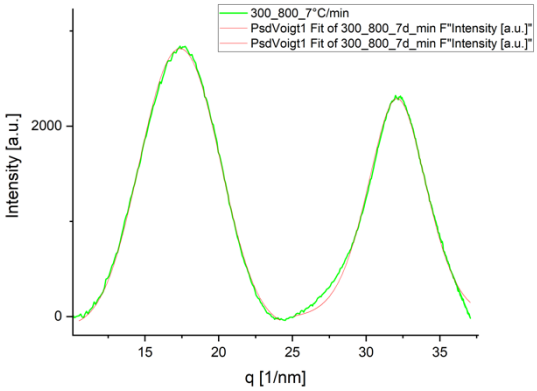
300_800_7°C/min
PsdVoigt1 Fit of 300_800_7d_min F"Intensity [a.u.]"
PsdVoigt1 Fit of 300_800_7d_min F"Intensity [a.u.]"
Intensity [a.u.]
q [1/nm]

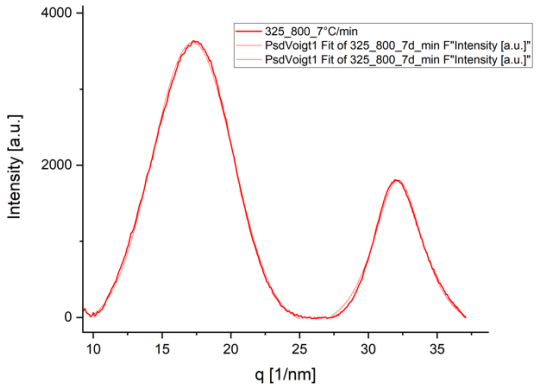
325_800_7°C/min
PsdVoigt1 Fit of 325_800_7d_min F"Intensity [a.u.]"
PsdVoigt1 Fit of 325_800_7d_min F"Intensity [a.u.]"
Intensity [a.u.]
q [1/nm]

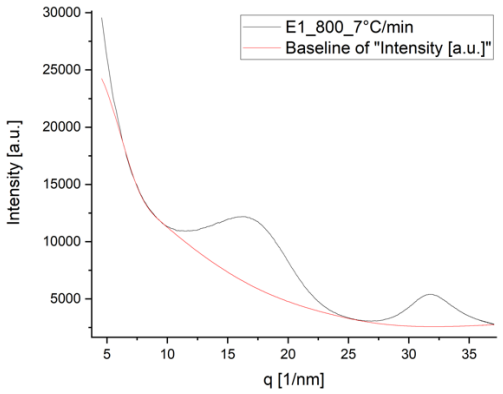
E1_800_7°C/min
Baseline of "Intensity [a.u.]"
Intensity [a.u.]
q [1/nm]

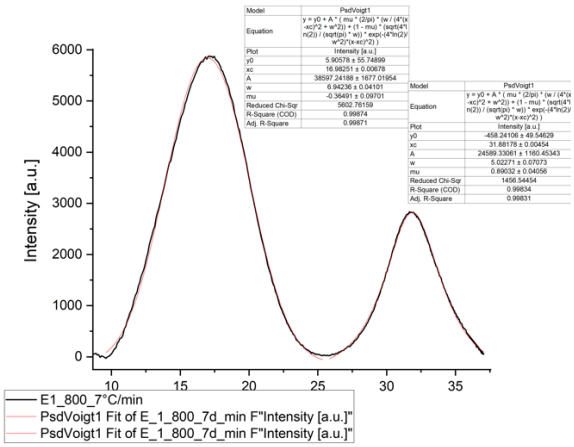
E1_800_7°C/min
PsdVoigt1 Fit of E_1_800_7d_min F"Intensity [a.u.]"
PsdVoigt1 Fit of E_1_800_7d_min F"Intensity [a.u.]"
Intensity [a.u.]

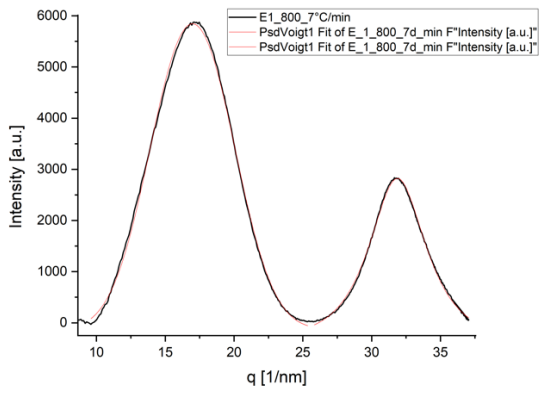
E1_800_7°C/min
PsdVoigt1 Fit of E_1_800_7d_min F"Intensity [a.u.]"
PsdVoigt1 Fit of E_1_800_7d_min F"Intensity [a.u.]"
Intensity [a.u.]
q [1/nm]

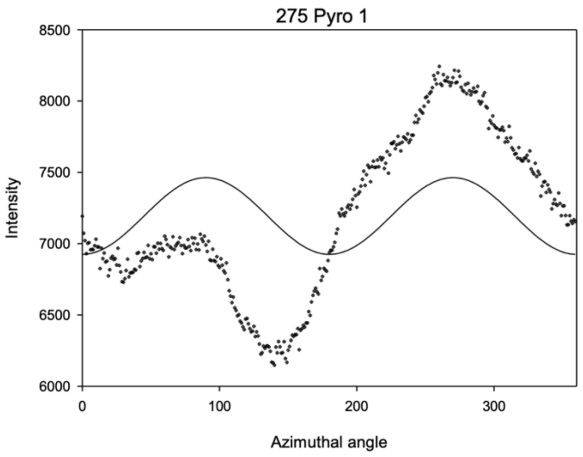
275 Pyro 1
Intensity
Azimuthal angle

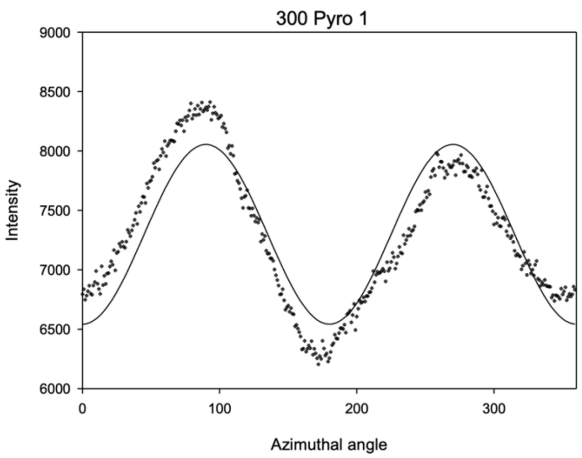
300 Pyro 1
Intensity
Azimuthal angle

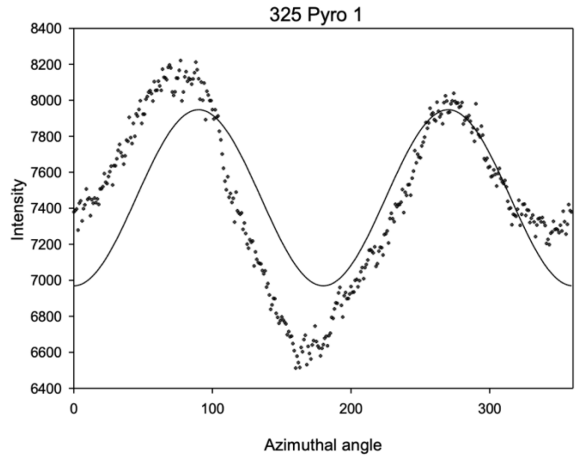
325 Pyro 1
Intensity
Azimuthal angle

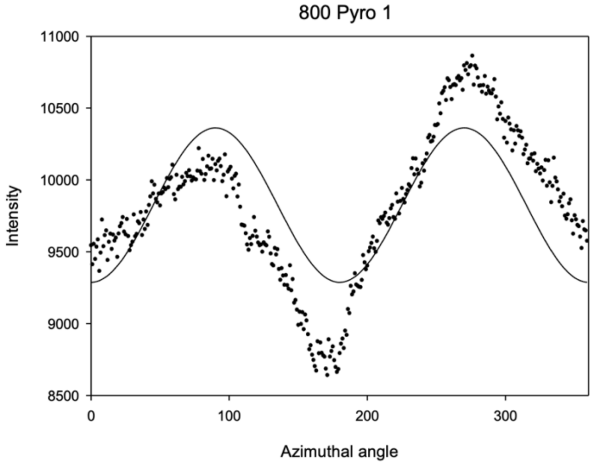
800 Pyro 1
Intensity
Azimuthal angle

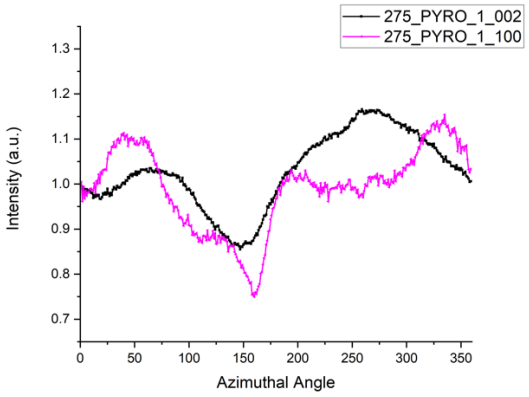
275_PYRO_1_002
275_PYRO_1_100
Intensity (a.u.)
Azimuthal Angle

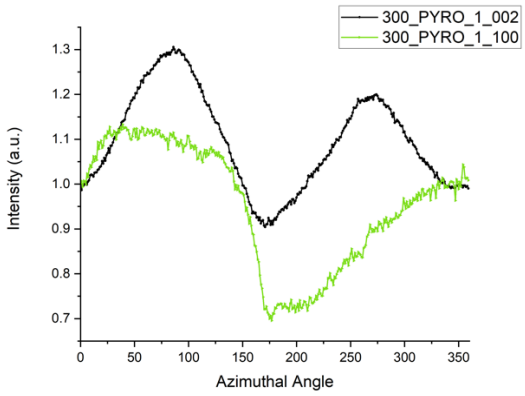
300_PYRO_1_002
300_PYRO_1_100
Intensity (a.u.)
Azimuthal Angle

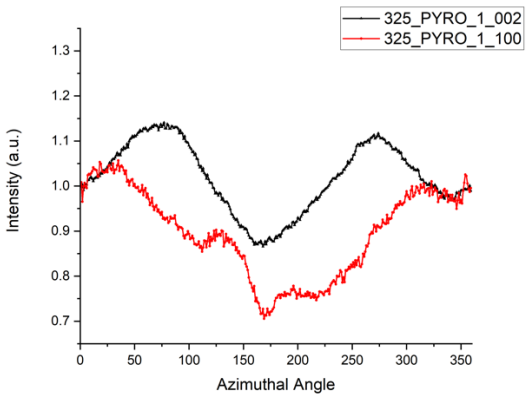
325_PYRO_1_002
325_PYRO_1_100
Intensity (a.u.)
Azimuthal Angle

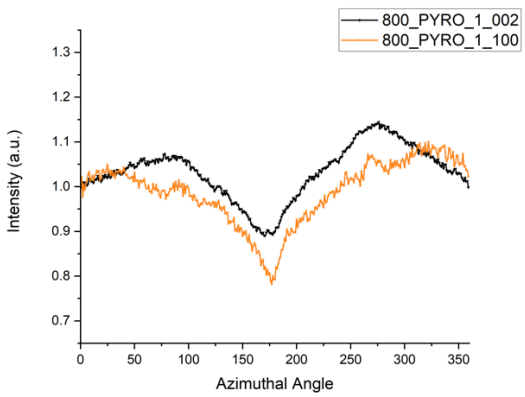
800_PYRO_1_002
800_PYRO_1_100
Intensity (a.u.)
Azimuthal Angle

PYRO 2

WAXD

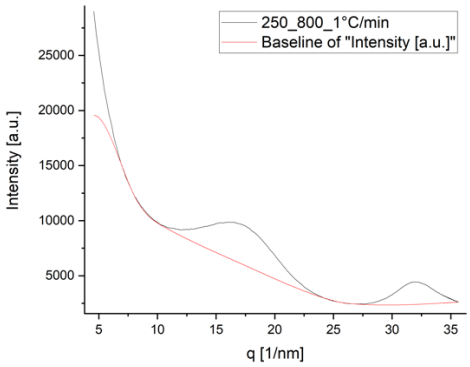

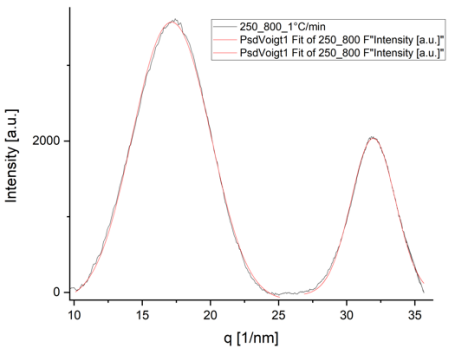

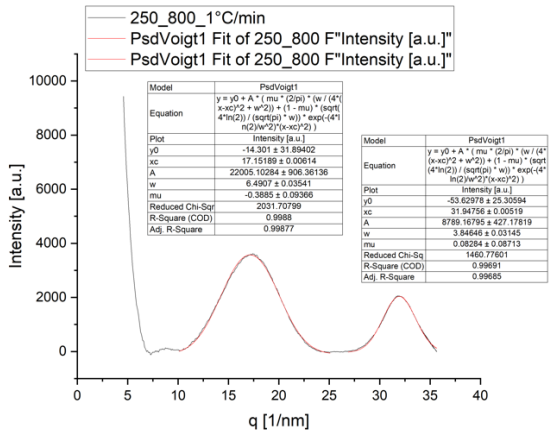

Model	PsdVoigt1
Equation	y = y0 + A * (mu * (2/pi) * (w / (4*(x-xc)^2 + w^2)) + (1 - mu) * (sqrt(4*ln(2)) / (sqrt(pi) * w)) * exp(-(4*ln(2)/w^2)*(x-xc)^2))
Plot	Intensity [a.u.]
y0	-14.301 ± 31.89402
xc	17.15189 ± 0.00614
A	22005.10284 ± 906.36136
w	6.4907 ± 0.03541
mu	-0.3885 ± 0.09366
Reduced Chi-Sqr	2031.70799
R-Square (COD)	0.9988
Adj. R-Square	0.99877

Model	PsdVoigt1
Equation	y = y0 + A * (mu * (2/pi) * (w / (4*(x-xc)^2 + w^2)) + (1 - mu) * (sqrt(4*ln(2)) / (sqrt(pi) * w)) * exp(-(4*ln(2)/w^2)*(x-xc)^2))
Plot	Intensity [a.u.]
y0	-53.62978 ± 25.30594
xc	31.94756 ± 0.00519
A	8789.16795 ± 427.17819
w	3.84646 ± 0.03145
mu	0.08284 ± 0.08713
Reduced Chi-Sq	1460.77601
R-Square (COD)	0.99691
Adj. R-Square	0.99685

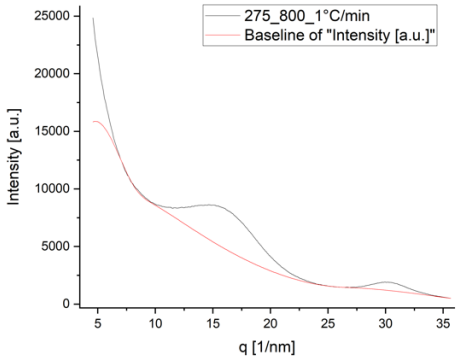

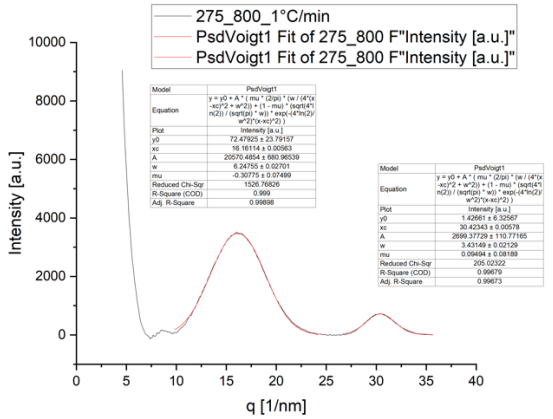

Model	PsdVoigt1
Equation	y = y0 + A * (mu * (2/pi) * (w / (4*(x-xc)^2 + w^2)) + (1 - mu) * (sqrt(4*ln(2)) / (sqrt(pi) * w)) * exp(-(4*ln(2)/w^2)*(x-xc)^2))
Plot	Intensity [a.u.]
y0	72.47925 ± 23.79157
xc	16.16114 ± 0.00563
A	20570.4854 ± 680.96539
w	6.24755 ± 0.02701
mu	-0.30775 ± 0.07499
Reduced Chi-Sqr	1526.76826
R-Square (COD)	0.999
Adj. R-Square	0.99898

Model	PsdVoigt1
Equation	y = y0 + A * (mu * (2/pi) * (w / (4*(x-xc)^2 + w^2)) + (1 - mu) * (sqrt(4*ln(2)) / (sqrt(pi) * w)) * exp(-(4*ln(2)/w^2)*(x-xc)^2))
Plot	Intensity [a.u.]
y0	1.42661 ± 6.32567
xc	30.42343 ± 0.00578
A	2699.37729 ± 110.77165
w	3.43149 ± 0.02129
mu	0.09494 ± 0.08189
Reduced Chi-Sqr	205.02322
R-Square (COD)	0.99679
Adj. R-Square	0.99673

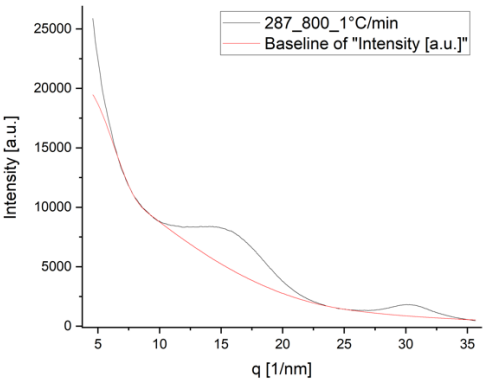

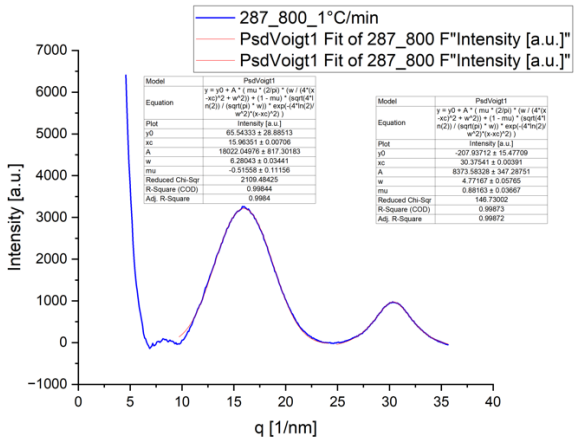
287_800_1°C/min
PsdVoigt1 Fit of 287_800 F"Intensity [a.u.]"
PsdVoigt1 Fit of 287_800 F"Intensity [a.u.]"
Intensity [a.u.]
q [1/nm]

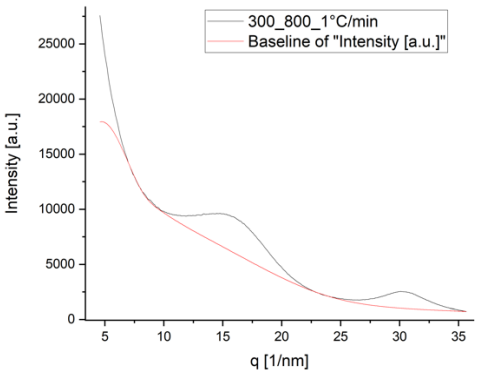
300_800_1°C/min
Baseline of "Intensity [a.u.]"
Intensity [a.u.]
q [1/nm]

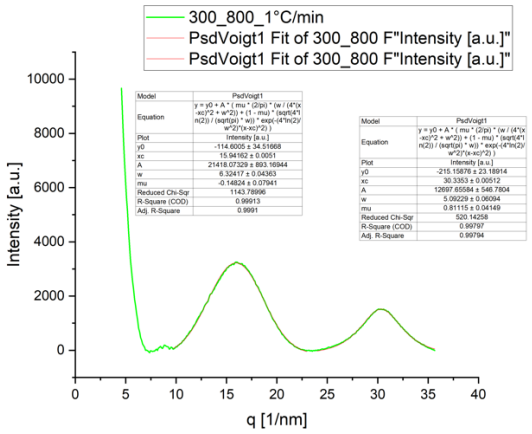
300_800_1°C/min
PsdVoigt1 Fit of 300_800 F"Intensity [a.u.]"
PsdVoigt1 Fit of 300_800 F"Intensity [a.u.]"
Intensity [a.u.]
q [1/nm]

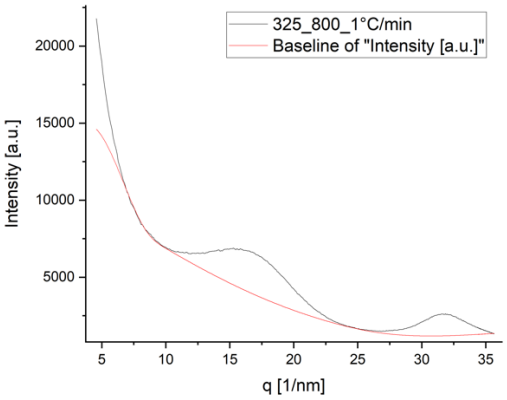
325_800_1°C/min
Baseline of "Intensity [a.u.]"
Intensity [a.u.]
q [1/nm]

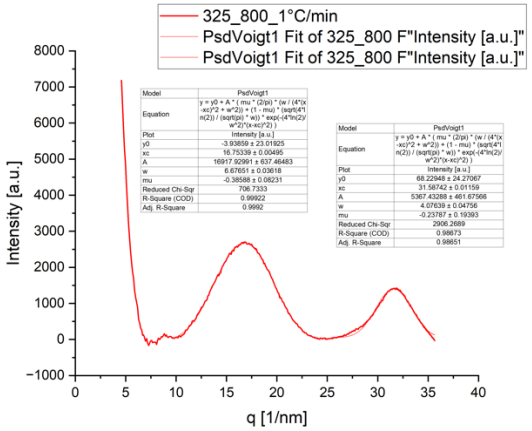
325_800_1°C/min
PsdVoigt1 Fit of 325_800 F"Intensity [a.u.]"
PsdVoigt1 Fit of 325_800 F"Intensity [a.u.]"
Intensity [a.u.]
q [1/nm]

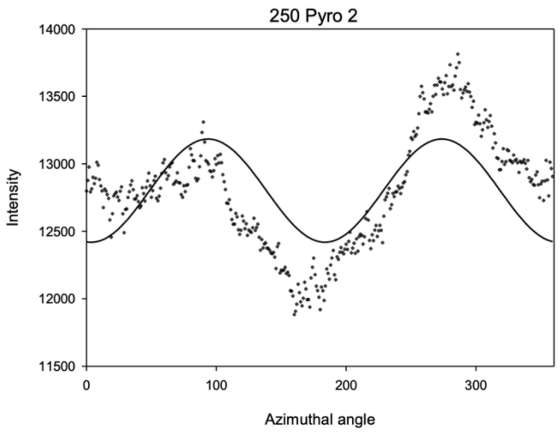
250 Pyro 2
Intensity
Azimuthal angle

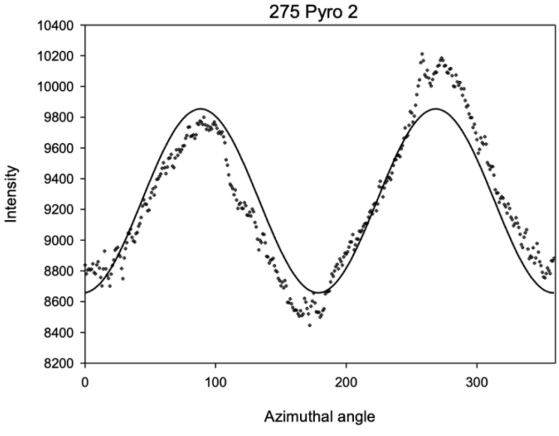
275 Pyro 2
Intensity
Azimuthal angle

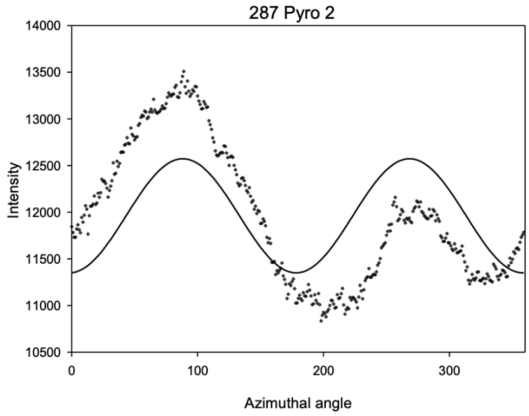
287 Pyro 2
Intensity
Azimuthal angle

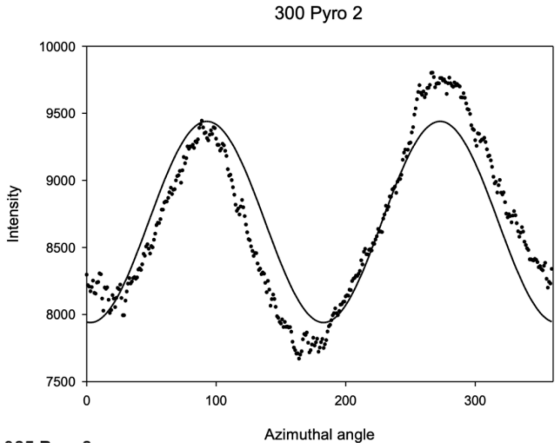
300 Pyro 2
Intensity
Azimuthal angle

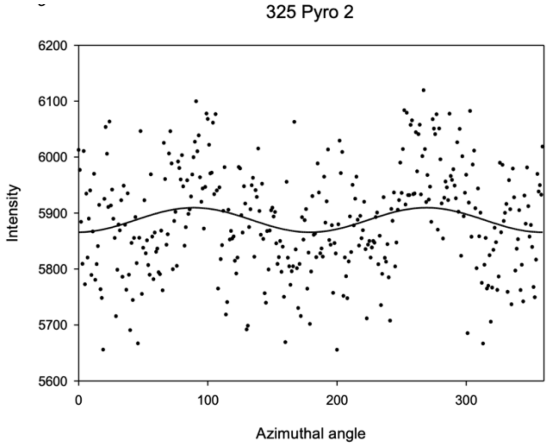
325 Pyro 2
Intensity
Azimuthal angle

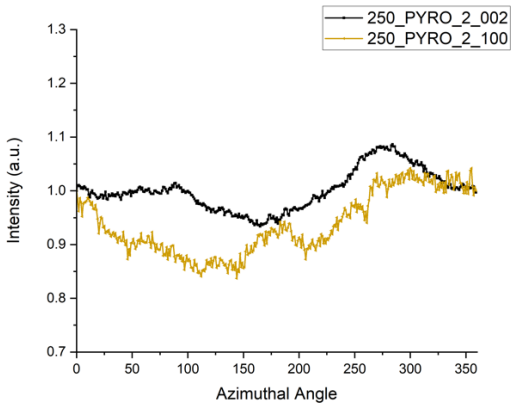
250_PYRO_2_002
250_PYRO_2_100
Intensity (a.u.)
Azimuthal Angle

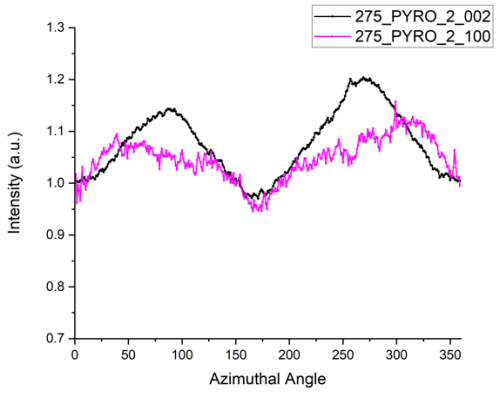
275_PYRO_2_002
275_PYRO_2_100
Intensity (a.u.)
Azimuthal Angle

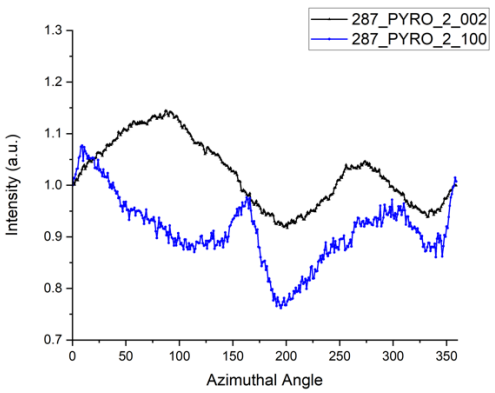
287_PYRO_2_002
287_PYRO_2_100
Intensity (a.u.)
Azimuthal Angle

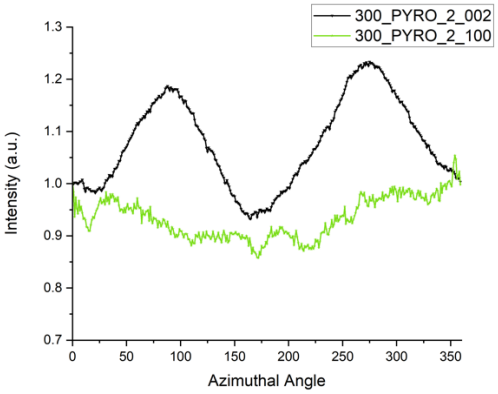
300_PYRO_2_002
300_PYRO_2_100
Intensity (a.u.)
Azimuthal Angle

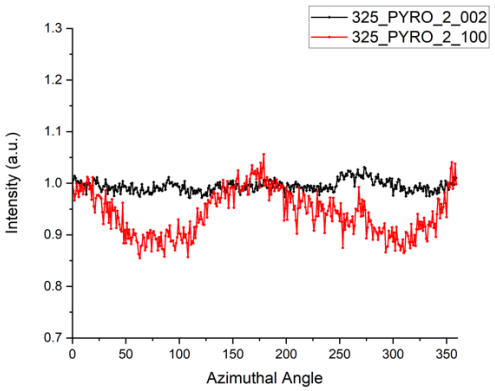
325_PYRO_2_002
325_PYRO_2_100
Intensity (a.u.)
Azimuthal Angle

PYRO 3

WAXD

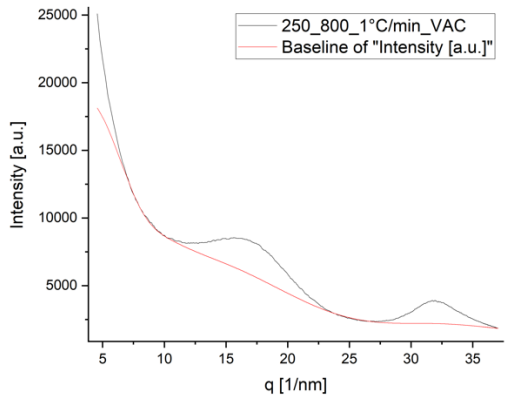
250_800_1°C/min_VAC
Baseline of "Intensity [a.u.]"
Intensity [a.u.]
q [1/nm]

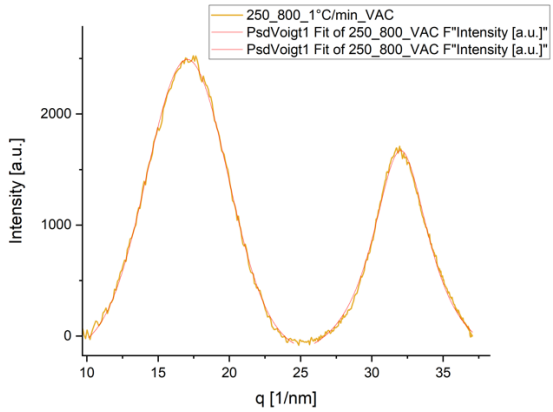
250_800_1°C/min_VAC
PsdVoigt1 Fit of 250_800_VAC F"Intensity [a.u.]"
PsdVoigt1 Fit of 250_800_VAC F"Intensity [a.u.]"
Intensity [a.u.]
q [1/nm]

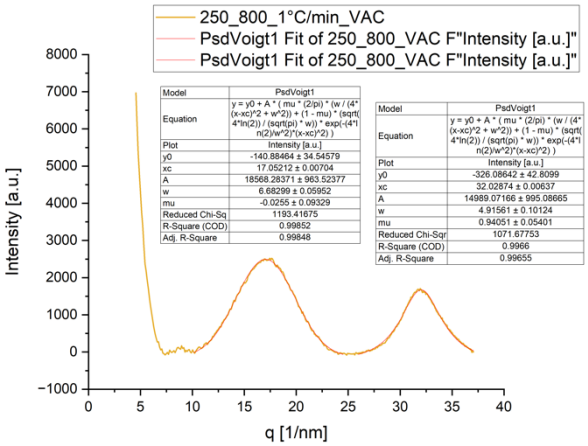
250_800_1°C/min_VAC
PsdVoigt1 Fit of 250_800_VAC F"Intensity [a.u.]"
PsdVoigt1 Fit of 250_800_VAC F"Intensity [a.u.]"
Model PsdVoigt1
Equation y = y0 + A * (mu * (2/pi) * (w / (4*(x-xc)^2 + w^2)) + (1 - mu) * (sqrt(4*ln(2)) / (sqrt(pi) * w)) * exp(-(4*ln(2)/w^2)*(x-xc)^2))
Plot Intensity [a.u.]
y0 -140.88464 ± 34.54579
xc 17.05212 ± 0.00704
A 18568.28371 ± 963.52377
w 6.68299 ± 0.05952
mu -0.0255 ± 0.09329
Reduced Chi-Sq 1193.41675
R-Square (COD) 0.99852
Adj. R-Square 0.99848
Model PsdVoigt1
Equation y = y0 + A * (mu * (2/pi) * (w / (4*(x-xc)^2 + w^2)) + (1 - mu) * (sqrt(4*ln(2)) / (sqrt(pi) * w)) * exp(-(4*ln(2)/w^2)*(x-xc)^2))
Plot Intensity [a.u.]
y0 -326.08642 ± 42.8099
xc 32.02874 ± 0.00637
A 14989.07166 ± 995.08665
w 4.91561 ± 0.10124
mu 0.94051 ± 0.05401
Reduced Chi-Sqr 1071.67753
R-Square (COD) 0.9966
Adj. R-Square 0.99655
Intensity [a.u.]
q [1/nm]

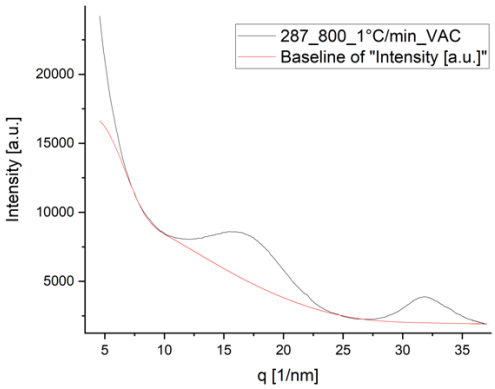
287_800_1°C/min_VAC
Baseline of "Intensity [a.u.]"
Intensity [a.u.]
q [1/nm]

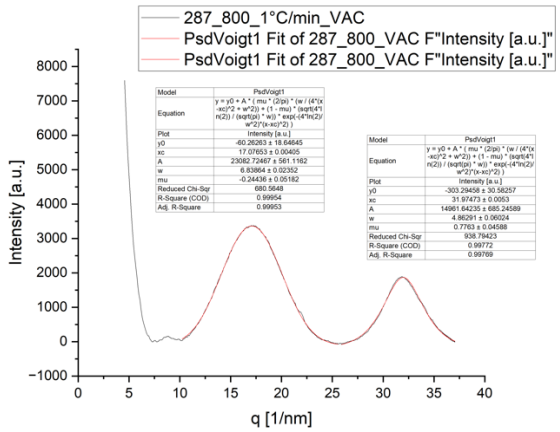

Model	PsdVoigt1
Equation	y = y0 + A * (mu * (2/pi) * (w / (4*(x-xc)^2 + w^2)) + (1 - mu) * (sqrt(4*ln(2)) / (sqrt(pi) * w)) * exp(-(4*ln(2)/w^2)*(x-xc)^2))
Plot	Intensity [a.u.]
y0	-60.26263 ± 18.64645
xc	17.07653 ± 0.00405
A	23082.72467 ± 561.1182
w	6.83864 ± 0.02352
mu	-0.24436 ± 0.05182
Reduced Chi-Sqr	680.5648
R-Square (COD)	0.99954
Adj. R-Square	0.99953

Model	PsdVoigt1
Equation	y = y0 + A * (mu * (2/pi) * (w / (4*(x-xc)^2 + w^2)) + (1 - mu) * (sqrt(4*ln(2)) / (sqrt(pi) * w)) * exp(-(4*ln(2)/w^2)*(x-xc)^2))
Plot	Intensity [a.u.]
y0	-303.29458 ± 30.58257
xc	31.97473 ± 0.0053
A	14961.64235 ± 685.24589
w	4.86291 ± 0.06024
mu	0.7763 ± 0.04588
Reduced Chi-Sqr	938.79423
R-Square (COD)	0.99772
Adj. R-Square	0.99769

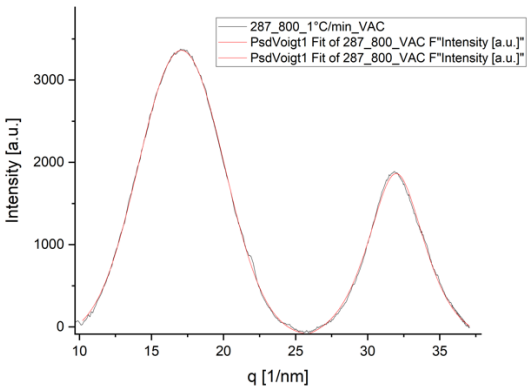

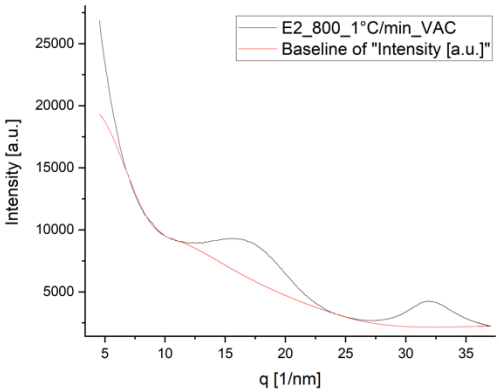

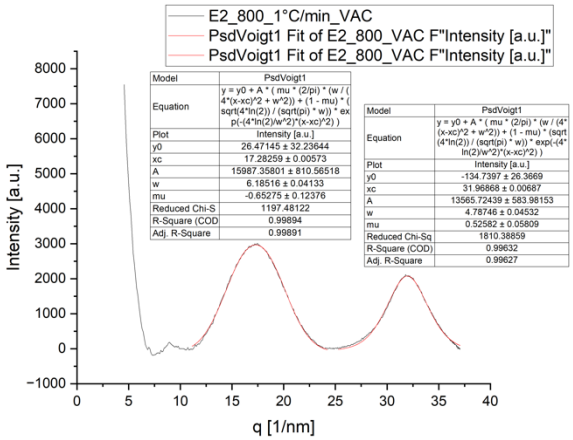

Model	PsdVoigt1
Equation	y = y0 + A * (mu * (2/pi) * (w / (4*(x-xc)^2 + w^2)) + (1 - mu) * (sqrt(4*ln(2)) / (sqrt(pi) * w)) * exp(-(4*ln(2)/w^2)*(x-xc)^2))
Plot	Intensity [a.u.]
y0	26.47145 ± 32.23644
xc	17.28259 ± 0.00573
A	15987.35801 ± 810.56518
w	6.18516 ± 0.04133
mu	-0.65275 ± 0.12376
Reduced Chi-S	1197.48122
R-Square (COD	0.99894
Adj. R-Square	0.99891

Model	PsdVoigt1
Equation	y = y0 + A * (mu * (2/pi) * (w / (4*(x-xc)^2 + w^2)) + (1 - mu) * (sqrt(4*ln(2)) / (sqrt(pi) * w)) * exp(-(4*ln(2)/w^2)*(x-xc)^2))
Plot	Intensity [a.u.]
y0	-134.7397 ± 26.3669
xc	31.96868 ± 0.00687
A	13565.72439 ± 583.98153
w	4.78746 ± 0.04532
mu	0.52582 ± 0.05809
Reduced Chi-Sq	1810.38859
R-Square (COD)	0.99632
Adj. R-Square	0.99627

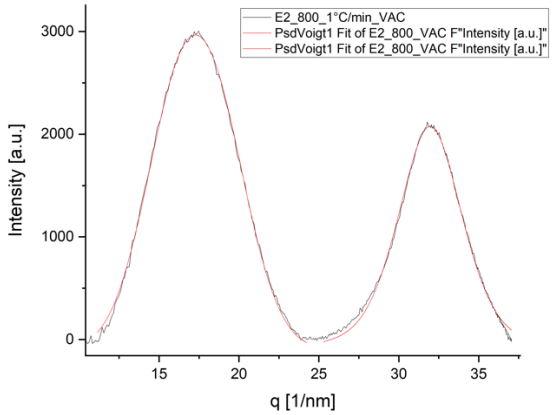

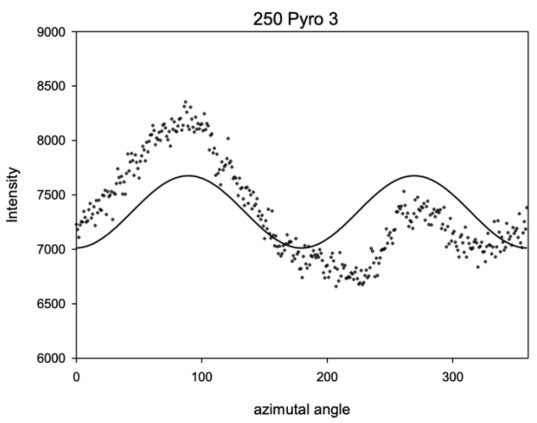
250 Pyro 3
Intensity
azimutal angle

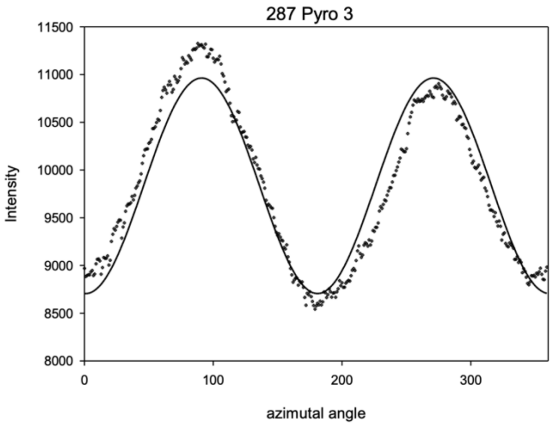
287 Pyro 3
Intensity
azimutal angle

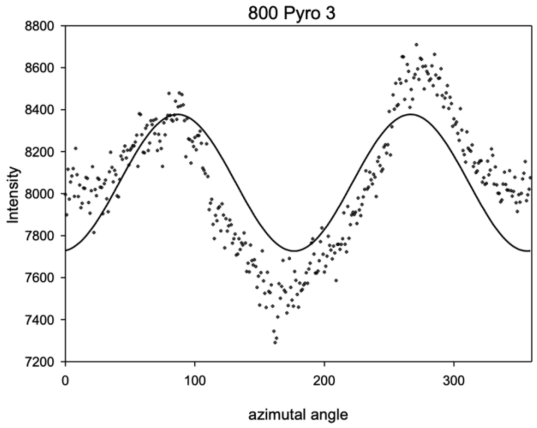
800 Pyro 3
Intensity
azimutal angle

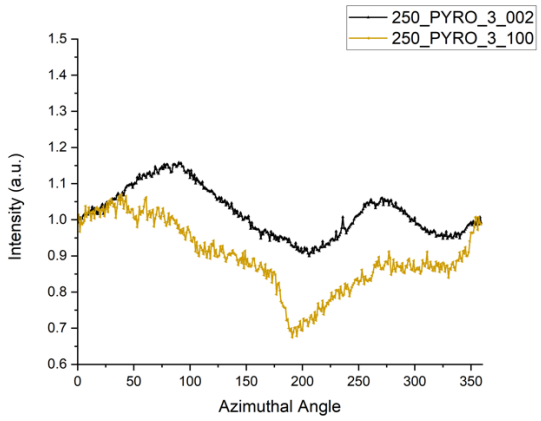
250_PYRO_3_002
250_PYRO_3_100
Intensity (a.u.)
Azimuthal Angle

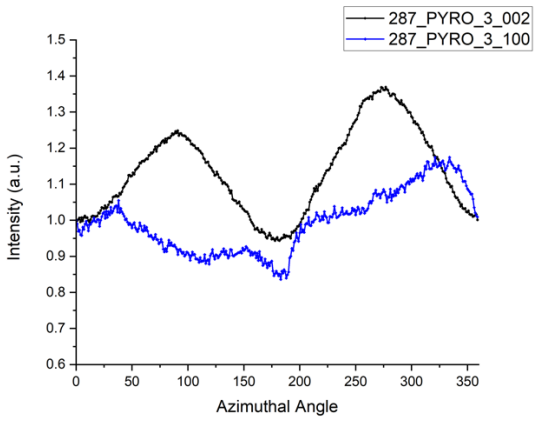
287_PYRO_3_002
287_PYRO_3_100
Intensity (a.u.)
Azimuthal Angle

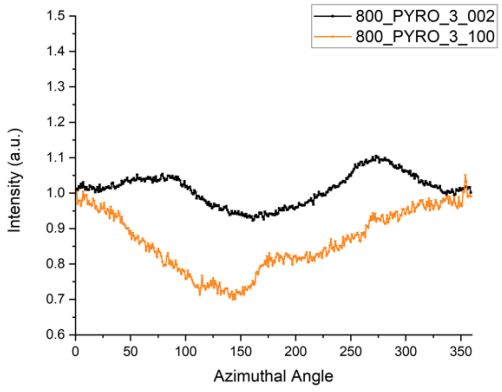
800_PYRO_3_002
800_PYRO_3_100
Intensity (a.u.)
Azimuthal Angle

ACTIVATION

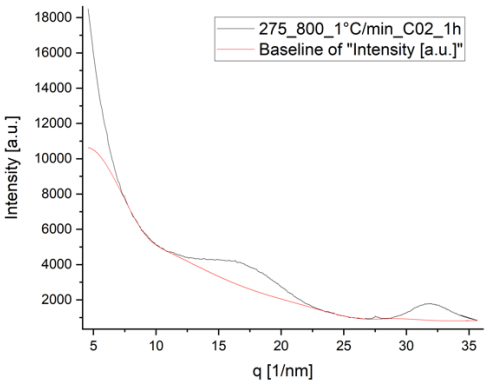
275_800_1°C/min_C02_1h
Baseline of "Intensity [a.u.]"
Intensity [a.u.]
q [1/nm]

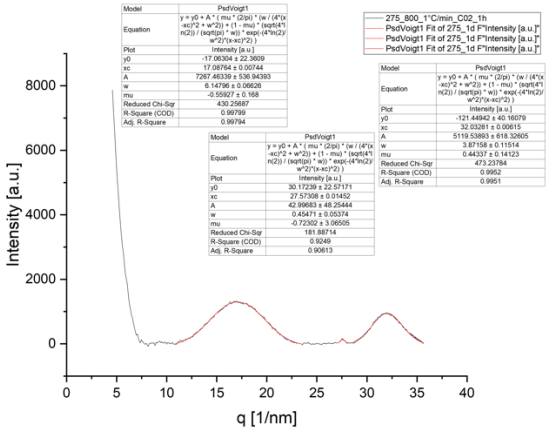
Model PsdVoigt1
Equation y = y0 + A * (mu * (2/pi) * (w / (4*(x -xc)^2 + w^2)) + (1 - mu) * (sqrt(4*l n(2)) / (sqrt(pi) * w)) * exp(-(4*ln(2)/ w^2)*(x-xc)^2))
Plot Intensity [a.u.]
y0 -17.06304 ± 22.3699
xc 17.08764 ± 0.00744
A 7267.46339 ± 536.94393
w 6.14798 ± 0.09626
mu -0.55927 ± 0.168
Reduced Chi-Sqr 430.25687
R-Square (COD) 0.99799
Adj. R-Square 0.99794
Model PsdVoigt1
Equation y = y0 + A * (mu * (2/pi) * (w / (4*(x -xc)^2 + w^2)) + (1 - mu) * (sqrt(4*l n(2)) / (sqrt(pi) * w)) * exp(-(4*ln(2)/ w^2)*(x-xc)^2))
Plot Intensity [a.u.]
y0 30.17239 ± 22.57177
xc 27.57308 ± 0.01452
A 42.99683 ± 48.25444
w 0.45471 ± 0.05374
mu -0.72302 ± 3.06505
Reduced Chi-Sqr 181.88714
R-Square (COD) 0.9249
Adj. R-Square 0.90613
Model PsdVoigt1
Equation y = y0 + A * (mu * (2/pi) * (w / (4*(x -xc)^2 + w^2)) + (1 - mu) * (sqrt(4*l n(2)) / (sqrt(pi) * w)) * exp(-(4*ln(2)/ w^2)*(x-xc)^2))
Plot Intensity [a.u.]
y0 -121.44942 ± 40.16079
xc 32.03281 ± 0.00615
A 5119.53893 ± 618.32605
w 3.87158 ± 0.11514
mu 0.44337 ± 0.14123
Reduced Chi-Sqr 473.23784
R-Square (COD) 0.9952
Adj. R-Square 0.9951
275_800_1°C/min_C02_1h
PsdVoigt1 Fit of 275_1d F"Intensity [a.u.]"
PsdVoigt1 Fit of 275_1d F"Intensity [a.u.]"
PsdVoigt1 Fit of 275_1d F"Intensity [a.u.]"
Intensity [a.u.]
q [1/nm]

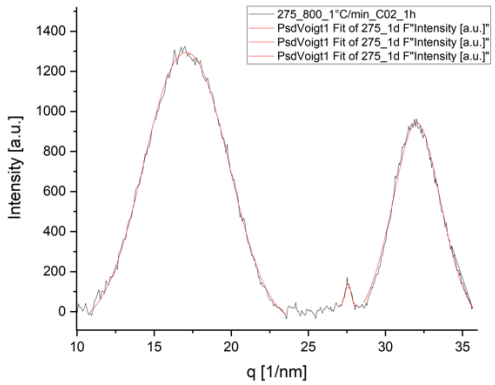
275_800_1°C/min_C02_1h
PsdVoigt1 Fit of 275_1d F"Intensity [a.u.]"
PsdVoigt1 Fit of 275_1d F"Intensity [a.u.]"
PsdVoigt1 Fit of 275_1d F"Intensity [a.u.]"
Intensity [a.u.]
q [1/nm]

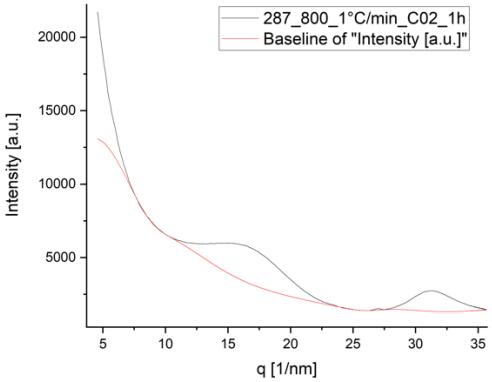
287_800_1°C/min_C02_1h
Baseline of "Intensity [a.u.]"
Intensity [a.u.]
q [1/nm]

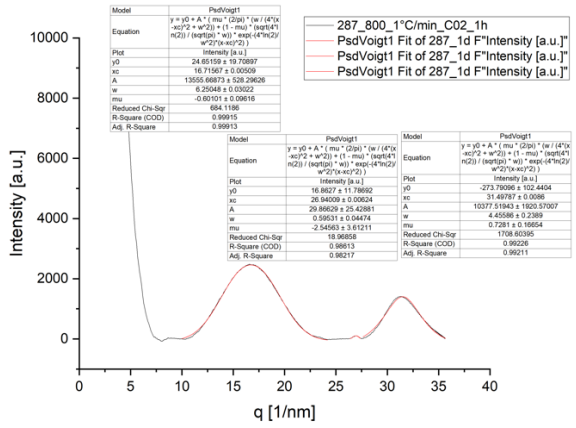
Model PsdVoigt1
Equation y = y0 + A * (mu * (2/pi) * (w / (4*(x -xc)^2 + w^2)) + (1 - mu) * (sqrt(4*l n(2)) / (sqrt(pi) * w)) * exp(-(4*ln(2)/ w^2)*(x-xc)^2))
Plot Intensity [a.u.]
y0 24.65159 ± 19.70897
xc 16.71567 ± 0.00509
A 13555.66873 ± 528.29626
w 6.25048 ± 0.03022
mu -0.60101 ± 0.09616
Reduced Chi-Sqr 684.1186
R-Square (COD) 0.99915
Adj. R-Square 0.99913
Model PsdVoigt1
Equation y = y0 + A * (mu * (2/pi) * (w / (4*(x -xc)^2 + w^2)) + (1 - mu) * (sqrt(4*l n(2)) / (sqrt(pi) * w)) * exp(-(4*ln(2)/ w^2)*(x-xc)^2))
Plot Intensity [a.u.]
y0 16.8627 ± 11.78692
xc 26.94009 ± 0.00624
A 29.88629 ± 25.42881
w 0.59531 ± 0.04474
mu -2.54563 ± 3.61211
Reduced Chi-Sqr 18.96858
R-Square (COD) 0.98613
Adj. R-Square 0.98217
Model PsdVoigt1
Equation y = y0 + A * (mu * (2/pi) * (w / (4*(x -xc)^2 + w^2)) + (1 - mu) * (sqrt(4*l n(2)) / (sqrt(pi) * w)) * exp(-(4*ln(2)/ w^2)*(x-xc)^2))
Plot Intensity [a.u.]
y0 -273.79096 ± 102.4404
xc 31.49787 ± 0.0086
A 10377.51943 ± 1820.57007
w 4.45586 ± 0.2389
mu 0.7281 ± 0.16654
Reduced Chi-Sqr 1708.80395
R-Square (COD) 0.99226
Adj. R-Square 0.99211
287_800_1°C/min_C02_1h
PsdVoigt1 Fit of 287_1d F"Intensity [a.u.]"
PsdVoigt1 Fit of 287_1d F"Intensity [a.u.]"
PsdVoigt1 Fit of 287_1d F"Intensity [a.u.]"
Intensity [a.u.]
q [1/nm]

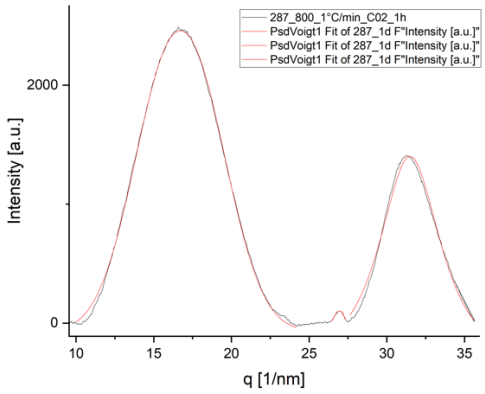
287_800_1°C/min_C02_1h
PsdVoigt1 Fit of 287_1d F"Intensity [a.u.]"
PsdVoigt1 Fit of 287_1d F"Intensity [a.u.]"
PsdVoigt1 Fit of 287_1d F"Intensity [a.u.]"
Intensity [a.u.]
q [1/nm]

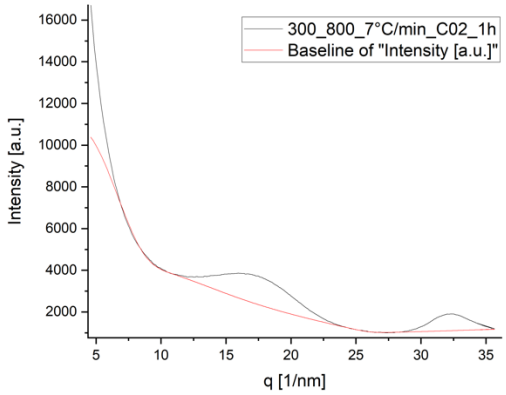
300_800_7°C/min_C02_1h
Baseline of "Intensity [a.u.]"
Intensity [a.u.]
q [1/nm]

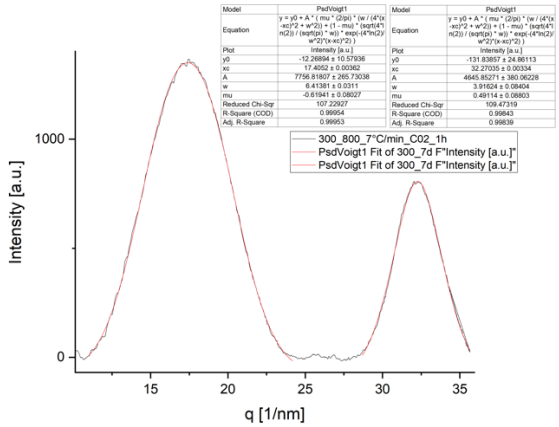
300_800_7°C/min_C02_1h
PsdVoigt1 Fit of 300_7d F"Intensity [a.u.]"
PsdVoigt1 Fit of 300_7d F"Intensity [a.u.]"
Intensity [a.u.]
q [1/nm]

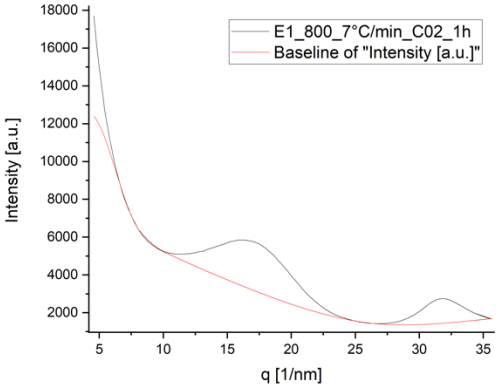
E1_800_7°C/min_C02_1h
Baseline of "Intensity [a.u.]"
Intensity [a.u.]
q [1/nm]

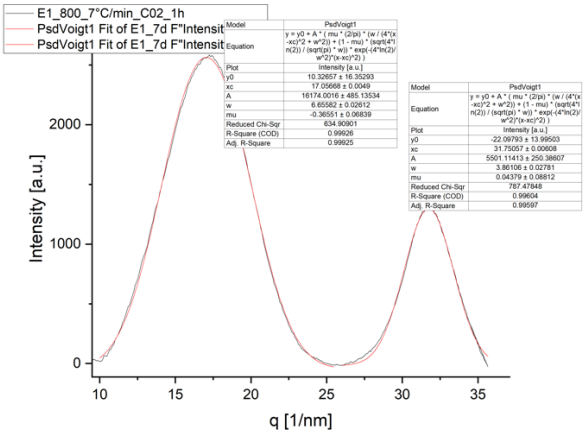
E1_800_7°C/min_C02_1h
PsdVoigt1 Fit of E1_7d F"Intensit
PsdVoigt1 Fit of E1_7d F"Intensit
Intensity [a.u.]
q [1/nm]

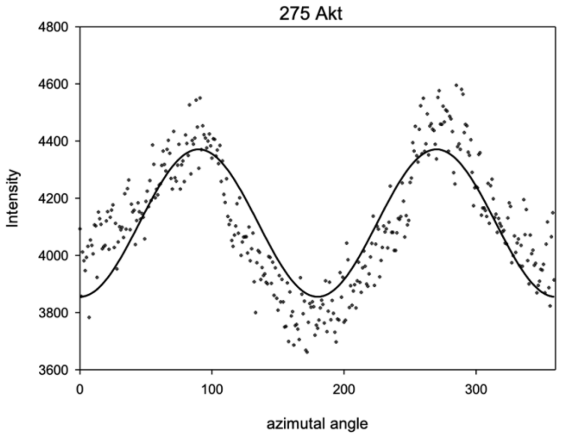
275 Akt
Intensity
azimutal angle

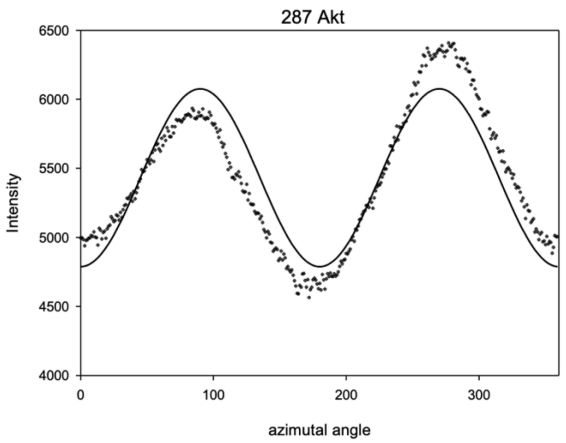
287 Akt
Intensity
azimutal angle

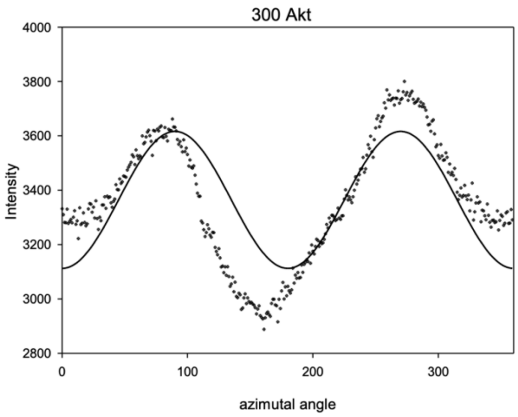
300 Akt
Intensity
azimutal angle

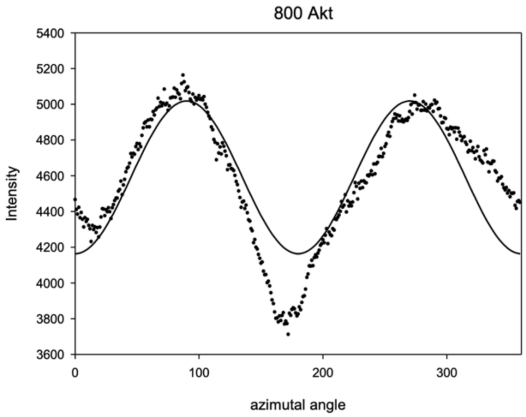
800 Akt
Intensity
azimutal angle

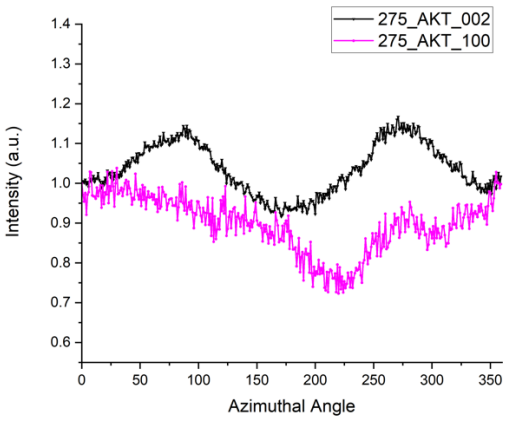
275_AKT_002
275_AKT_100
Intensity (a.u.)
Azimuthal Angle

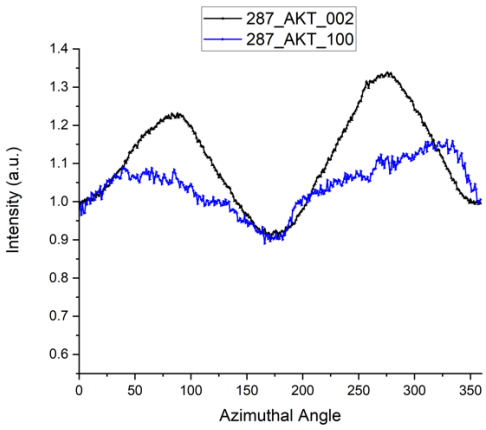
287_AKT_002
287_AKT_100
Intensity (a.u.)
Azimuthal Angle

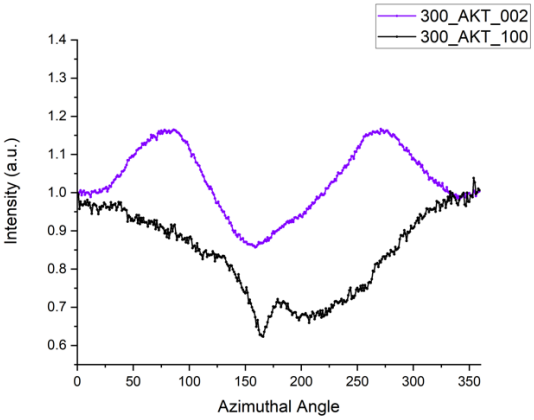
300_AKT_002
300_AKT_100
Intensity (a.u.)
Azimuthal Angle

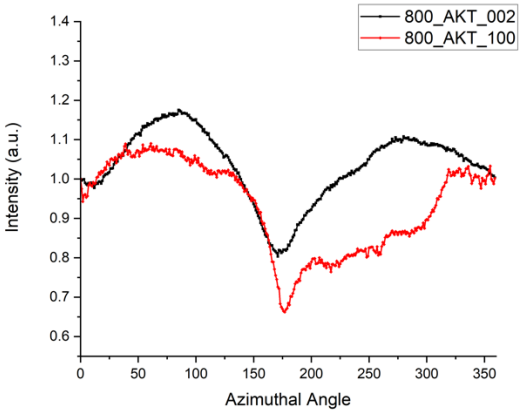
800_AKT_002
800_AKT_100
Intensity (a.u.)
Azimuthal Angle

GAS SORPTION: NITROGEN